ALMA MATER STUDIORUM
UNIVERSITÀ DI BOLOGNA

DOTTORATO DI RICERCA IN

MECCANICA E SCIENZE AVANZATE DELL'INGEGNERIA

Ciclo 38

Settore Concorsuale: 09/C2 - FISICA TECNICA E INGEGNERIA NUCLEARE

Settore Scientifico Disciplinare: ING-IND/18 - FISICA DEI REATTORI NUCLEARI

DEVELOPMENT OF A NUMERICAL FRAMEWORK FOR MODELING AND REDUCTION OF PLASMA CHEMICAL KINETICS

Presentata da: Andrea Marchetti

Coordinatore Dottorato

Lorenzo Donati

Supervisore

Matteo Gherardi

Co-supervisore

Ernesto Salzano

Elkid Cobani

Esame finale anno 2026

Finanziato dall'Unione europea- Next Generation EU, Missione 4, Componente 2, Investimento 3.3 (D.M. 117/2023) CUP J33C22001480009

The greatest teacher, failure is.

Master Yoda

Abstract

This thesis aims to extend numerical modeling techniques for non-equilibrium plasmas in order to simplify the study of complex plasma-chemical processes. In particular, it presents the development of a numerical solver for global models (SPPARK - Simulation Platform for Plasma Assisted Reactive Kinetics), based on the coupling of Cantera and Bolsig+, which provides an open-source framework to represent complex phenomena such as electron kinetics in non-equilibrium plasmas, reaction thermodynamics, and the interactions between these two domains. The solver also includes the capability to model heterogeneous phase phenomena, allowing the incorporation of interaction mechanisms of a plasma phase with electrodes and gas ones. In this context, the thesis introduces a multizone approach for the representation of systems that are not strictly spatially homogeneous. This approach consists of defining a separate system of ordinary differential equation for each phase and introducing transport derived net source terms in such equations, thereby enabling separate results for different phases while maintaining their coupling through the representation of transport processes. The overall goal is to obtain simulation results from complex reaction schemes that are less constrained by the assumption of homogeneity. This approach can provide useful and more detailed inputs for the final aspect addressed in the thesis: the adoption of Analytically Reduced Chemistry techniques in plasma-chemistry modeling. These techniques allow for the reduction of the chemical complexity associated with the reaction schemes used in numerical models. The simplification of detailed reaction mechanisms, with arbitrary and controllable accuracy, enables their adoption within geometrically resolved simulations, while keeping the computational cost contained. The thesis ultimately presents a comprehensive chemistry reduction framework, combining established methodologies with new approaches, that can deal with the reduction of arbitrary complex chemistry sets for non-equilibrium plasmas.

Preface

In this thesis, I wish to recount the work I have carried out over the past three years during my doctoral studies. This journey has provided me with the opportunity to immerse myself in the field of numerical modeling of non-equilibrium plasmas, particularly in the chemical fundamentals of this area. I consider the common thread of this work to be the attempt to establish a connection between different modeling domains, that may persist, in the form of a simulation framework, beyond the completion of my PhD.

At the beginning of my doctoral research, I noticed a separation between the different branches contributing to the modeling of plasma-enhanced chemical processes. My work therefore aims, within my limits, to expand the modeling capabilities for processes that combine electronic non-equilibrium phenomena with thermochemical and thermodynamic effects, processes that require a careful balance between chemical detail and spatial non-uniformity, and that are often too complex to interpret *a priori*.

For these reasons, during this journey I had the pleasure of developing a numerical solver for global models capable of coupling a detailed treatment of electron kinetics with an accurate representation of reaction thermodynamics. I subsequently extended it to represent, through a multizone approach, non-homogeneous geometries with complex chemistries. Finally, I explored the possibility of adopting higher geometrical resolutions in these phenomena modeling, starting from reaction schemes that would otherwise be computationally prohibitive, by applying a structured and automated reduction. Throughout this process, I also found a great deal of enjoyment and personal satisfaction.

Contents

Chapter 1

Introduction

Non-equilibrium plasmas find applications in a wide range of engineering contexts, including materials science [1–4], environmental applications [5–8], aerospace engineering [9–11], biomedical applications [12–15], and the electrification of chemical processes [16–19]. Each of these applications, although exploiting different properties of partially ionized gases, is influenced by the chemical kinetics that develops within the plasma. The study of such kinetics is the subject of plasma chemistry.

Due to their intrinsic thermodynamic non-equilibrium, non-thermal plasmas can sustain reaction pathways that would otherwise be unfavourable under global thermodynamic conditions. This behaviour is directly linked to the key role of electrons in the system: they gain energy from externally applied electromagnetic fields and transfer it to the other particles, thereby shifting, at constant macroscopic temperature, the gas composition away from equilibrium and producing ions, excited species, and radicals. The presence of these species is what drives the chemical reactivity of non-equilibrium plasmas.

This feature, however, introduces additional complexity in the study of the elementary mechanisms that affect process efficiency. From both a fundamental and process-optimization perspective, the numerical modeling of non-equilibrium plasmas thus becomes a highly valuable tool. The present thesis is framed within this context.

In continuum descriptions, depending on the level of accuracy required by the specific application, different mathematical models can be employed to represent a non-equilibrium plasma. When focusing exclusively on chemical interactions, global models are generally adopted. These numerical models are spatially homogeneous (zero-dimensional) that enable a detailed representation of chemical mechanisms through complex reaction schemes. Conversely, fluid models are spatially resolved numerical models that emphasize the dynamics of the species, including the possibility of representing the plasma source and its electromagnetic coupling with the plasma phase (self-consistent fluid models). These models also rely on the adoption of a chemical reaction scheme in order to incorporate source terms in the species continuity equations. However, due to computational cost

limitations, the chemical schemes employed in fluid models are generally required to be less detailed than those that can be used in global models.

The main objective of this thesis is to contribute to the current state-of-the-art modeling capabilities by introducing a new and generalized tool for plasma chemistry. More specifically, the tool is based on a novel and generalized global model solver for plasma chemistry (SPPARK – Simulation Platform for Plasma Assisted Reactive Kinetics), designed to accurately capture the chemical phenomena occurring in plasmas under applications where the gas temperature spans wide ranges.

To achieve this, SPPARK has been developed by coupling Bolsig+ [20] and Cantera [21], in such a way as to combine the accurate treatment of electron kinetics (through Bolsig+) with the detailed description of species thermodynamic properties and, consequently, of reaction thermodynamics (through Cantera). In this sense SPPARK was built as a Python package on the Cantera extensible backend, handling external calls to Bolsig+ at runtime. Furthermore, the adoption of Cantera enables the introduction of a multi-zone modeling approach within global modeling of plasmas, thereby partially relaxing the assumption of spatial homogeneity that is typically inherent to such models.

In addition to the solver, this thesis also introduces an algorithm for chemical complexity reduction, with the goal of providing a framework that allows starting from detailed reaction mechanisms (as characteristic of global models) to simplify and adapt them for use within fluid models.

In this thesis, it is shown how the combination of SPPARK with the reduction algorithm, within a unified framework, constitutes a useful contribution to plasma modeling, enabling more accurate and flexible simulations, particularly for gas mixtures for which only limited prior information is available.

The thesis is organized as follows:

- Chapter 2 - Plasma chemistry – an overview, where an overview of the theoretical concepts, mathematical formulations and numerical representation of plasma-chemistry is introduced.

- Chapter 3 – A Generalized Global Model Solver for Plasma Chemistry, where the rationale behind the development of SPPARK is presented together with validation cases.

- Chapter 4 – Multizone Global Modeling of Plasmas, where the use of SPPARK for multi-zone simulations of global models is described in greater detail.

- Chapter 5 – Analytically Reduced Chemistry for Non-Equilibrium Plasmas, where the automatic algorithm for reaction mechanism reduction is introduced.

References

[1] Sun X, Bao J, Li K, Argyle M D, Tan G, Adidharma H, Zhang K, Fan M and Ning P 2021 Advance in Using Plasma Technology for Modification or Fabrication of Carbon-Based Materials and Their Applications in Environmental, Material, and Energy Fields *Adv Funct Materials* **31** 2006287

[2] Li C, Zhang T, Qiu Z, Ye B, Liang X, Liu X, Chen M, Xia X, Wang C, Wan W and Zhang Y 2025 Plasma-assisted fabrication of multiscale materials for electrochemical energy conversion and storage *Carbon Energy* **7** e641

[3] Feng X, Tao H, Yang S, Liu C, Wei C, Wang Y, Zhao H, Yao S and Cheng Z 2025 Recent Advances of Plasma Technology Applications in 2D Materials and Electronics *Adv Materials Technologies* **10** 2402207

[4] Han Z J, Murdock A T, Seo D H and Bendavid A 2018 Recent progress in plasma-assisted synthesis and modification of 2D materials *2D Mater.* **5** 032002

[5] Dobslaw C and Glocker B 2020 Plasma Technology and Its Relevance in Waste Air and Waste Gas Treatment *Sustainability* **12** 8981

[6] Sanito R C, You S-J and Wang Y-F 2022 Degradation of contaminants in plasma technology: An overview *Journal of Hazardous Materials* **424** 127390

[7] Oost G 2022 Applications of Thermal Plasmas for the Environment *Applied Sciences* **12** 7185

[8] Mizuno A 2007 Industrial applications of atmospheric non-thermal plasma in environmental remediation *Plasma Phys. Control. Fusion* **49** A1–15

[9] Semenov V E, Bondarenko V G, Gildenburg V B, Gubchenko V M and Smirnov A I 2002 Weakly ionized plasmas in aerospace applications *Plasma Phys. Control. Fusion* **44** B293

[10] Kim M 2014 Active plasma layer manipulation scheme during hypersonic flight *Aerospace Science and Technology* **35** 135–42

[11] Esposito S, Scarabosio A, Vecchi G and D'Ambrosio D 2024 Non-equilibrium plasma distribution in the wake of a slender blunted-nose cone in hypersonic flight and its effect on the radar cross section *Aerospace Science and Technology* **155** 109699

[12] Bisag A, Isabelli P, Laghi G, Laurita R, Dirani G, Taddei F, Bucci C, Capelli F, Gherardi M, Paglianti A, Sambri V and Colombo V 2022 Cold atmospheric plasma decontamination of SARS-CoV-2 bioaerosols *Plasma Processes and Polymers* **19** e2100133

[13] Lu X, Naidis G V, Laroussi M, Reuter S, Graves D B and Ostrikov K 2016 Reactive species in non-equilibrium atmospheric-pressure plasmas: Generation, transport, and biological effects *Physics Reports* **630** 1–84

[14] von Woedtke T, Laroussi M and Gherardi M 2022 Foundations of plasmas for medical applications *Plasma Sources Sci. Technol.* **31** 054002

[15] Duarte S and Panariello B H D 2020 Comprehensive biomedical applications of low temperature plasmas *Archives of Biochemistry and Biophysics* **693** 108560

[16] Nozaki T, Kim D-Y and Chen X 2024 Plasma-enabled electrification of chemical processes toward decarbonization of society *Jpn. J. Appl. Phys.* **63** 030101

[17] Kamarinopoulou N S, Nguyen D K and Vlachos D G 2025 Process-chemistry intensification using non-thermal plasmas: Toward one-step chemical production *Current Opinion in Green and Sustainable Chemistry* **51** 100997

[18] Jung C, Khoe Dinh D, Lee C, Sohn S, Kim Y-N and Hoon Lee D 2024 Highly selective conversion of toluene to acetylene for upcycling by a plasma process *Chemical Engineering Journal* **481** 148604

[19] Maslova V, Nastase R, Veryasov G, Nesterenko N, Fourré E and Batiot-Dupeyrat C 2024 Current status and challenges of plasma and plasma-catalysis for methane coupling: A review *Progress in Energy and Combustion Science* **101** 101096

[20] Hagelaar G J M and Pitchford L C 2005 Solving the Boltzmann equation to obtain electron transport coefficients and rate coefficients for fluid models *Plasma Sources Science and Technology* **14** 722–33

[21] Goodwin D G, Moffat H K, Schoegl I, Speth R L and Weber B W 2024 Cantera: An Object-oriented Software Toolkit for Chemical Kinetics, Thermodynamics, and Transport Processes

Chapter 2

Plasma-chemistry: an overview

2.1 Introduction

Non-equilibrium plasmas could be defined as a globally neutral ionized gas populated by free highly energetic electrons and ions immersed in a background gas medium. As mentioned before, the high energy of electrons can be engineeringly used to sustain valuable chemical processes by employing plasma-chemical kinetics.

The founding mechanism of such phenomena involves a free electron placed within an electromagnetic field which experiences a Lorentz force:

$$\vec{F} = -e\left(\vec{E} + \vec{v} \times \vec{B}\right) \tag{2.1}$$

where e is the electron charge, $\vec{E}$ is the electric field, $\vec{v}$ is the electron velocity, and $\vec{B}$ is the magnetic flux density.

Under this force, the electron accelerates, gaining energy, and moves through space. If along its trajectory it encounters another particle (*i.e.*, it comes sufficiently close to the target particle), an interaction between the two particles may occur, in which the electron (being more energetic) can transfer energy to the second body. If the particle is different from another electron (*i.e.,* a heavy particle), either elastic collisions (in which the total momentum of the binary system is conserved) or inelastic collisions (in which the second body absorbs part of the electron's energy during the collision getting promoted to an excited state) can take place [1]. Among inelastic collisions, the following can be distinguished:

- Electronic excitations, in which the valence electron of the target particle is excited during the collision to a higher-energy orbital.

- Vibrational excitations, possible in the case of a molecular target, in which the bond between atoms is excited, increasing the relative motion of the nuclei.

- Rotational excitations, also possible only for molecular targets, in which the molecule is set into rotation by the electron impact.

- Dissociations, in which the molecular bond is broken by the electron impact, releasing radicals.

- Ionization, in which the valence electron receives enough energy to escape from the collision target, thus producing an ion.

- Combinations of the above processes.

In addition to the processes listed above, super-elastic collisions may also occur. In addition to the processes listed above, super-elastic collisions may also occur. In these processes, which feature excited or metastable particles, the electron gains energy from the collision, leading to de-excitation and, more generally, to associative or recombination processes involving the target particles.

Extending the discussion to a collection (population) of electrons, in a system at thermodynamic equilibrium (*i.e.*, a system in which a sufficiently long time has elapsed since the previous perturbation to allow it to reach its most stable and probable configuration), the application of an electromagnetic field represents a perturbation of the system's state. Through the interaction mechanisms previously described, electrons subjected to the external forcing mediate the redistribution of the externally supplied energy among the plasma constituents, driving the heavy-particle system state away from global thermodynamic equilibrium. At the microscopic level, the particles interactions act as relaxation mechanisms tending to restore local thermal equilibrium; however, at a macroscopic scale it sustains non-equilibrium conditions. As a result, energy is conveyed by electrons both to a direct transfer of kinetic energy - temperature (via elastic collisions) - and to an imbalance in the chemical composition (*i.e.*, the introduction of radicals) as well as in the distribution of excited states of its components (via inelastic collisions). The perturbed system will naturally tend to restore equilibrium through relaxation processes (*i.e.*, photon emissions, vibrational-to-translational relaxations, vibrational-to-vibrational relaxations), which may favour the conversion of potential energy acquired by the collision targets into kinetic energy (this time of the heavy-particle system) and chemical recombinations.

2.2 Mathematical formulations for plasma-chemistry

For a system of N particles, the qualitative description given so far can be translated, at a microscopic scale, into a system of deterministic equations describing the trajectory of the system in the $6N$-dimensional phase space (for each particle we introduce 3 variables for the coordinates in geometric space and 3 variables for the velocity-space coordinates) via the Hamiltonian formulation.

$$H(\vec{q}_1, \dots, \vec{q}_n, \vec{p}_1, \dots \vec{p}_n) = T + V$$

$$H(\vec{q}_1, \dots, \vec{q}_n, \vec{p}_1, \dots \vec{p}_n) = \sum_{i=1}^{N} \frac{\|\vec{p}_i\|^2}{2m_i} + V_{\text{ext}}(\vec{q}_1, \dots, \vec{q}_n) + \sum\nolimits_{j>i} U_{ij}(\vec{q}_i - \vec{q}_j) \tag{2.2}$$

where H is the system's Hamiltonian, $\vec{q}_i$ is the i-th particle generalized coordinates' vector, $\vec{p}_i$ is the i-th particle momentum, T is the system's kinetic energy, V is the total potential, m_i is the i-th particle mass, V_{ext} is the external potential, and U_{ij} is the interaction potential between the i-th and j-th particle dependant on the two particles characteristics (*i.e.* the particles charges). This leads to the canonical equations:

$$\begin{cases} \dfrac{d\vec{q}_i}{dt} = \dfrac{\partial H}{\partial \vec{p}_i} = \dfrac{\vec{p}_i}{m_i} \\ \dfrac{d\vec{p}_i}{dt} = -\dfrac{\partial H}{\partial \vec{q}_i} = -\dfrac{\partial V_{\text{ext}}}{\partial \vec{q}_i} - \displaystyle\sum_{j \neq i} \frac{\partial U_{ij}(\vec{q}_i - \vec{q}_j)}{\partial \vec{q}_i} \end{cases} \tag{2.3}$$

However, studying a complex system (with a large number of particles) at the microscopic scale is excessively demanding (one must solve a system of $6N$ equations to obtain a complete description of the system's kinetics). For this reason, by means of the Liouville equation and the Bogoliubov–Born–Green–Kirkwood–Yvon (BBGKY) hierarchy [2], and by introducing the hypothesis that particles interact only during collisions (assumed approximatively instantaneous) and of "molecular chaos" (*i.e.*, the assumption of uncorrelated particle velocities prior to collisions), it is possible to approximate the problem and represent it by stochastic integro-differential equations (Boltzmann equations), thus introducing the mesoscale description of the phenomena. These equations describe the particle population through a single-particle distribution function representing the fraction of particles occupying a subset of geometric space $(\vec{x}, \vec{x} + d\vec{x})$ and velocity space $(\vec{v}, \vec{v} + d\vec{v})$. Focusing on the electronic population, the Boltzmann equation for electrons (EBE) can be written as follows:

$$\frac{\partial f_e}{\partial t} + \vec{v} \cdot \nabla f_e - \frac{e}{m_e}\left(\vec{E} + \vec{v} \times \vec{B}\right) \cdot \nabla_v f_e = C \tag{2.4}$$

where f_e is the single-particle distribution function for the electrons, m_e is the electron mass, ∇ represents the gradient operator in the geometrical space, ∇_v represents the gradient operator in the velocity space, and C represents the integral term considering the collisional processes faced by the electrons. Through the EBE it is possible to represent the whole electron population in a six-dimensional space in a single equation.

Nevertheless, the level of detail achieved by the mesoscale formulation is often unnecessary to describe the macroscopic behaviour of the system. In fact, for any

particle population - whether electrons or heavy species - the macroscopic quantities describing the thermodynamic state of the system can be obtained by solving partial differential equations (PDEs) derived from velocity-space moments of the Boltzmann equation. Specifically, the mass (or particle number), momentum, and energy balance equations can be obtained as the zeroth, first, and second moments of the Boltzmann equation, respectively as follows [3]:

$$\int_{\Omega_v}\left[\frac{\partial f_e}{\partial t}+\vec{v}\cdot\nabla f_e-\frac{e}{m_e}\left(\vec{E}+\vec{v}\times\vec{B}\right)\cdot\nabla_v f_e\right]F(\vec{v})d_3v=\int_{\Omega_v}C\cdot F(\vec{v})d_3v \tag{2.5}$$

where Ω_v is the velocity domain, d_3v is a compact notation representing the three velocity coordinates $\left(d_3v=dv_xdv_ydv_z\right)$, and $F(\vec{v})$ is a function of the velocity variable which selects the moments of the distribution [3]:

$$F(\vec{v})=1\Rightarrow n_e(\vec{x},t)=\int_{\Omega_v}f_e d_3v \tag{2.6}$$

$$F(\vec{v})=\vec{v}\Rightarrow n_e\vec{u}=\int_{\Omega_v}\vec{v}f_e d_3v \tag{2.7}$$

$$F(\vec{v})=\frac{1}{2}m_e v^2\Rightarrow w=\frac{3}{2}n_e k_b T_e+\frac{1}{2}m_e u^2 n_e=\frac{1}{2}m_e\int_{\Omega_v}v^2 f_e d_3v \tag{2.8}$$

where n_e is the electron particle (or number) density, $\vec{u}$ is the electrons mean velocity, and w is the particle kinetic energy per unit volume (with $\frac{3}{2}n_e k_b T_e$ internal energy and $\frac{1}{2}m_e u^2 n_e$ flow of energy density, with k_b the Boltzmann constant and T_e is the electron temperature).

Integrating the EBE, it is possible to obtain the following macroscopic conservation equations:

$$\frac{\partial n_e}{\partial t}+\nabla\cdot(n_e\vec{u})=S_e \tag{2.9}$$

$$m_e n_e\left[\frac{\partial\vec{u}}{\partial t}+(\vec{u}\cdot\nabla)\vec{u}\right]=-en_e\left(\vec{E}+\vec{u}\times\vec{B}\right)-\nabla\cdot\hat{\Pi}+\vec{f}\Big|_c \tag{2.10}$$

$$\frac{\partial}{\partial t}\left(\frac{3}{2}p_e\right)+\nabla\cdot\frac{3}{2}(p_e\vec{u})+p_e\nabla\cdot\vec{u}+\nabla\cdot\vec{q}=\frac{\partial}{\partial t}\left(\frac{3}{2}p_e\right)\Big|_c \tag{2.11}$$

where n is the electron number density, $\vec{u}$ is the electron mean velocity, and $p_e=n_e k_b T_e$.

Some additional terms are also present in the equations:

$$S_i = \sum_{j=1}^{N} \nu_{i,j}^{net} \left[k_j^f \prod\nolimits_{q=1}^{S} n_q^{\nu_{q,j}^f} - k_j^r \prod\nolimits_{q=1}^{S} n_q^{\nu_{q,j}^r} \right] \tag{2.12}$$

$$\widehat{\Pi} = \begin{pmatrix} \Pi_{11} & \Pi_{12} & \Pi_{13} \\ \Pi_{21} & \Pi_{22} & \Pi_{23} \\ \Pi_{31} & \Pi_{32} & \Pi_{33} \end{pmatrix} : \; \Pi_{ij} = m_e n_e \langle (v_i - u)(v_j - u) \rangle_v \tag{2.13}$$

$$\vec{q} = -\kappa_T \nabla T_e \tag{2.14}$$

where $\nu_{i,j}^f$, $\nu_{i,j}^r$, $\nu_{i,j}^{net}$ are the forward, reverse and net stoichiometric coefficients of the i-th species in the j-th reaction, k_j^f and k_j^r are the forward and reverse rate coefficients of the j-th reaction (collision), n_q is the q-th species density, v_i is the single electron velocity magnitude in the i-th direction, u is the mean velocity magnitude, $\langle \cdot \rangle_v$ represents the averaging operator in the velocity space weighted on f_e, and κ_T is the thermal conductivity. The further parameters included in equations 2.10 and 2.11 ($\vec{f}\big|_c$ and $\frac{\partial}{\partial t}\left(\frac{3}{2} p_e\right)\Big|_c$) represent the effect of the collisional term C in the momentum and energy conservation equations [3].

These equations introduce terms that are inherently linked to the mesoscale (e.g., reaction rate coefficients or thermal conductivity or the collisional terms), thus leading to a closure problem for the system. This problem can be addressed either by assuming a specific energy distribution for each particle family or by formally determining it directly from the Boltzmann equation.

For heavy particles, such distribution assumption is generally well justified. In this case (except for ions), the forcing term is negligible. By considering a sufficiently homogeneous spatial region and modeling interactions between particles as binary collisions of hard spheres (*i.e.*, neglecting effects on the energy distribution resulting from collisions not captured by this idealization), each population of heavy particles can be described analytically by a Maxwell–Boltzmann distribution. This assumption allows the kinetic and transport parameters of these particles to be derived in closed form. For example, reaction rate constants for interactions between heavy particles can be approximated in the Arrhenius form [4]:

$$k_j = A_j \exp\left(-\frac{E_{a_j}}{RT}\right) \tag{2.15}$$

with A_j the preexponential factor, E_{aj} the activation energy of the reaction, T the particle population temperature, and R the ideal gas constant ($R = k_b N_a$ with N_a the Avogadro constant).

The Maxwellian distribution assumption, however, is generally not valid for electrons in low-temperature, weakly ionized plasma. In this case, electron-electron collisions are relatively infrequent compared to the electron-heavy particle interactions. In such regimes, modeling electron kinetics through a predefined equilibrium distribution would lead overly restrictive approximations. As a result, the Boltzmann equation for electrons must be solved at least in the energy space to ensure a reliable approximation of the kinetic and transport coefficients required for the closure of the system of equations.

2.3 Numerical modeling of plasma-chemistry

So far, the mathematical formulations useful for studying plasma-chemical processes have been introduced at three different scales: microscopic (equation 2.3), mesoscopic (equation 2.4), and macroscopic (equations $2.9 - 2.11$). It has also been discussed how these three scales are closely interconnected and can be derived from one another through successive approximations. In this context, it is worth noting that the most suitable mathematical formulation depends on the scale required by the study of the phenomena of interest.

In practical cases, the equations discussed above are solved through numerical simulation. Each scale introduces different mathematical formulations and therefore requires the adoption of distinct solution techniques. Among the main methodologies commonly employed in the numerical simulation of non-equilibrium plasmas are [5]:

- Particle In Cell (PIC): this method is aimed at simulating the behaviour of a non-equilibrium plasma at the microscale (with good accuracy). A hybrid approach is often adopted. A discrete number of *macro-particles* is introduced (each representing a large number of real particles, to reduce computational cost) whose equations of motion are solved under the action of electromagnetic forces (equation 2.1). These forces are computed from Maxwell's equations on a computational grid discretizing the geometrical space in which particles move. In this framework, interactions between particles occur only through the electromagnetic fields which are directly affected by the charged particles. In other words, the plasma is formally modelled as collision-less (mathematically represented through the Vlasov kinetic equation).

- PIC-Monte Carlo (PIC-MC): This method represents a variant of the previously described PIC approach, designed to account for collisional interactions between particles (typically electrons and neutrals). The Monte Carlo methodology is added to the PIC framework to statistically estimate the occurrence of collisions between a macro-particle and the background gas and to identify their type based on input cross-section data. The energy and direction of motion of each particle selected as a collider are then modified according to the conservation laws of energy and momentum during the impact. This method enables the self-consistent determination of transport coefficients, reaction rates, and the electron energy distribution function, albeit at a higher computational cost and generally requiring a larger number of *macro-particles* compared to the PIC methodology.

- Kinetic models: This type of method refers to the mesoscale and involves solving the EBE (equation 2.4) directly. More precisely, it approximates the EBE by focusing only on the distribution in energy space. In this context, one of the most known approaches (see for example Hagelaar *et al.* [6]), which is based on a series expansion in spherical harmonics of the single-particle distribution function. In this method, the expansion is truncated at the second term ($f_e \approx f_0 + \cos(\theta)\, f_1$, valid approximation for low electric field values), and the dependence on spatial and temporal variables is assigned solely to the electron density. This allows the introduction of the electron energy distribution function (EEDF) and the anisotropy of the distribution as unknowns, both functions of the electron kinetic energy only. By doing so, it is possible to obtain two ordinary differential equations for these two unknowns, which can be solved numerically as boundary value problems. Also in this case, it is possible to obtain the kinetic and transport parameters of the electron population by means of the EEDF. For example:

$$k_j = \gamma \int_{\varepsilon=0}^{\infty} \varepsilon \sigma_j(\varepsilon)\, F_0(\varepsilon) d\varepsilon \tag{2.16}$$

  with $\gamma = \sqrt{2e/m_e}$, ε the colliding electron energy (eV), σ_j the j-th collision cross section (m^2), and F_0 the EEDF $\left(eV^{-\frac{3}{2}}\right)$.

- Fluid Models: this type of model refers to the macroscopic scale (equations 2.9 to 2.11). The system is thus studied through local average quantities as functions of time and geometric space. As mentioned earlier, to ensure closure of the mathematical problem, it is necessary to provide input data, typically related to the reaction rate constants and the transport parameters of the particle populations (especially for the electron population). In this

context, estimates of these parameters can generally be obtained from literature data or from previous simulations at a smaller dimensional scale.

A widely used example of a fluid model concerns drift-diffusion models, in which the solution of the momentum balance equation to determine the average velocity is avoided. Instead, the particle flux is approximated as resulting from electron mobility (μ_e) and diffusion (D_e) coefficients according to the following equation (valid for electrostatic fields):

$$n_e\vec{u} = -\mu_e n_e\vec{E} - D_e\nabla n_e \tag{2.17}$$

having equation 2.9 become:

$$\frac{\partial n_e}{\partial t} = \nabla\cdot\left(\mu_e n_e\vec{E} + D_e\nabla n_e\right) + S_e\left(k_j\right) \tag{2.18}$$

The electric field $\left(\vec{E}\right)$ is usually coupled with the continuity equation by means of the Gauss law.

In this context, the kinetic parameters (μ_e, D_e, k_j) have to be defined prior to the simulation execution. These parameters can be considered (with reasonable approximation) as functions of the mean electron energy ($\langle\varepsilon\rangle$). The drift-diffusion model can then be extended by means of the local mean energy approximation (LEA) with the following equation [5]:

$$\frac{\partial(n_e\langle\varepsilon\rangle)}{\partial t} + \nabla\cdot\vec{\Gamma}_\varepsilon = S_\varepsilon \tag{2.19}$$

where $\vec{\Gamma}_\varepsilon$ is the mean electron energy flux, and S_ε represents an energy source (involving collisions and fields), which approximates equation 2.11. It is worth noting that both $\vec{\Gamma}_\varepsilon$ and S_ε are determined by electron kinetic parameters (such as the energy mobility and diffusion coefficients), functions of the mean electron energy $\langle\varepsilon\rangle$.

A common practice to ensure a good representation of the kinetic aspects of a plasma is to precompute the values of the needed kinetic parameters by means of a mesoscale approach and to tabulate them as functions of the mean energy, relying on interpolating estimations in the simulation's runtime.

- Global models: belonging to the macroscopic class, these models represent the computationally lightest among those described so far. They focus on solving and representing the system only in terms of time (*i.e.*, they are zero-

dimensional - 0D). Although this approximation significantly simplifies the dynamics of the processes, it allows this type of model to be applied for rapid, high-level simulations of extremely complex systems in terms of the number of chemical species involved. The associated mathematical modeling can be obtained by imposing spatial uniformity on the equations previously introduced for a drift-diffusion model under the LEA:

$$\frac{\partial n_e}{\partial t} = S_e(k_j) \tag{2.20}$$

$$\frac{\partial (n_e \langle \varepsilon \rangle)}{\partial t} = S_\varepsilon \tag{2.21}$$

As mentioned before, also in this case electron kinetic parameters are required for the problem closure.

- Hybrid models: these represent models obtained by coupling of the previously described techniques [7]. For example, due to their low computational demands, the majority of global models are coupled with kinetic models by default.

In this context, the thesis focuses on an advanced global model development and application together with a batch coupling technique between global and fluid models based on Analytically Reduced Chemistry, a set of systematic approaches aimed at reducing the chemical complexity of detailed kinetic mechanisms by constructing simplified representations that retain the dominant kinetic pathways relevant to the conditions of interest, while significantly lowering the computational cost.

2.4 References

[1] Fridman A 2008 Plasma Chemistry *Plasma Chemistry* 9780521847353 1–978

[2] Cercignani C, Gerasimenko V I and Petrina D Ya 1997 The BBGKY Hierarchy *Many-Particle Dynamics and Kinetic Equations* ed C Cercignani, V I Gerasimenko and D Ya Petrina (Dordrecht: Springer Netherlands) pp 7–65

[3] Lieberman M A and Lichtenberg A J 2005 Principles of Plasma Discharges and Materials Processing: Second Edition *Principles of Plasma Discharges and Materials Processing: Second Edition* 1–757

[4] Steinfeld J I 1999 *Chemical kinetics and dynamics* (Upper Saddle River, N.J. : Prentice Hall)

[5] Alves L L, Bogaerts A, Guerra V and Turner M M 2018 Foundations of modelling of nonequilibrium low-temperature plasmas *Plasma Sources Sci. Technol.* 27 023002

[6] Hagelaar G J M and Pitchford L C 2005 Solving the Boltzmann equation to obtain electron transport coefficients and rate coefficients for fluid models *Plasma Sources Science and Technology* 14 722–33

[7] Kushner M J 2009 Hybrid modelling of low temperature plasmas for fundamental investigations and equipment design *J. Phys. D: Appl. Phys.* **42** 194013

Chapter 3

A Generalized Global Model Solver for Plasma Chemistry

This chapter is based on the article: A. Marchetti, et al., "SPPARK – a novel generalized simulation tool for non-equilibrium plasma chemistry", Journal of Physics D: Applied Physics, Vol. 58, pp. 315204, 2025, © The Author(s). Published by IOP Publishing Ltd. Reproduced with permission from the publisher.

3.1 Preface

This chapter introduces the rationale and methodology followed in the development of a simulation software for global models in non-equilibrium plasma chemistry (SPPARK - Simulation Platform for Plasma Assisted Reactive Kinetics), as described in the presentation paper of the solver – A. Marchetti, et al., "SPPARK – a novel generalized simulation tool for non-equilibrium plasma chemistry", *Journal of Physics D: Applied Physics*, Vol. 58, p. 315204, 2025. The software is based on the coupling between Bolsig+ (for which a Python wrapper has been developed) and Cantera, ensuring an accurate resolution of the electron Boltzmann equation and a robust representation of the reaction thermodynamics linked to thermochemistry. The solver is also benchmarked for validation against the state-of-the-art solver ZDPlasKin, both to demonstrate its accuracy in case studies that can likewise be handled by ZDPlasKin, and to highlight its capability to address scenarios that ZDPlasKin cannot manage with the same level of detail (e.g., reaction thermodynamics dependent on the gas temperature).

Within the context of this thesis, the solver introduced here is the one employed for every simulation subsequently reported. Since it is built upon Cantera, it readily supports the multizone approach (here described in Section 3.4.3.2) that constitutes the focus of Chapter 4. Moreover, the plasma chemistry reduction methodology introduced in Chapter 5 is directly based on the results and classes provided by the solver and is implemented as an additional module integrated into the software.

3.2 Abbreviations

GHG: Greenhouse gas

ODE: Ordinary Differential Equation

EBE: Electrons Boltzmann Equation

EEDF: Electron Energy Distribution Function

LFA: Local Field Approximation

LEA: Local mean Energy Approximation

PSR: Perfectly Stirred Reactor

3.3 Introduction

In the context of global climate crisis, the interest towards environmental sustainability of chemical processes is arising. To reduce the industry impact on greenhouse gasses (GHGs) production, plasma technologies have demonstrated to be a possible path for the chemical industry electrification, inducing a large interest in the scientific community. Some examples of the most studied plasma-chemical processes are: methane pyrolysis to split CH_4 and produce hydrogen and various carbon allotropic forms and nanostructures [1–7], low temperature methane oxidation to decrease the GHGs emissions [8–11]; methane coupling with the aim of C2 and C3 hydrocarbons production [12–17], nitrogen fixation for ammonia and fertilizers synthesis [18–25], carbon dioxide splitting [26–33], ammonia cracking [34–37] and carbon dioxide hydrogenation [38–43].

In a plasma, electrical power is coupled with the gas particles thanks to the charged particles susceptibility to electro-magnetic fields. Due to their low inertia, most of the energy is acquired by electrons and part of it is ceded to the gas (heavy) particles through collisions. Whenever the number of collisions per unit time is not high enough to thermally equilibrate electrons and heavy particles, the plasma is in non-equilibrium (*i.e.* a single temperature is not sufficient to describe the energies in the system). This characteristic is particularly interesting in chemical processes. In fact, it allows new reaction pathways to occur that otherwise would not be relevant at equal gas temperatures [44]. Moreover, plasma-chemical processes may present fast gas temperature raises as the system proceeds toward equilibrium [45,46].

On the other hand, these characteristics grant plasma-chemical interaction mechanisms high complexity: a large number of reactive species are coexisting in the system; the chemical kinetics is characterized by multiple timescales; the phenomena are presenting a multiphysics nature. This often leads to the need of numerical models to achieve insights on the founding mechanisms of the process.

In this context, a plasma chemistry solver is a numerical solver focusing on the zero-dimensional (0D) time-dependent evolution of the chemical system. Its general structure includes an ordinary differential equation (ODE) solver coupled with a Boltzmann solver, which is a numerical solver for the electron Boltzmann equation (EBE). The purpose of the ODE solver is to determine the time evolution of variables of interest. Concurrently, the Boltzmann solver computes the kinetic energy distribution of the electron population (Electron Energy Distribution Function - EEDF). This distribution is used to determine the electron population properties that are influencing the overall chemical kinetics. Among the available Boltzmann solvers, Bolsig+ [47] is one of the most used, granting high customization of the hypothesis influencing electron kinetic modeling. Bolsig+ is

actively coupled with different ODE solvers in most of the plasma-chemistry solvers [48–52] through embedded versions limiting the model customizability.

Some of the models, for example the one adopted by ZDPlasKin [48] and Plasimo [49], are more focused on the pure non-equilibrium plasma phenomena description. In fact, they allow users to include non-equilibrium reaction rate constants (*i.e.* dependent on the temperature, drift velocity or diffusivity of electrons), to use signals of electrical power densities coupled to the plasma directly as an electron solicitation (through power coupling models) for the EBE solution and to decouple the collisions utilized in the Boltzmann solver from the ones included as chemical reactions in the ODE solver. On the other hand, these kinds of solvers lack chemical model customizability as they are generally limited to Perfectly Stirred Reactor models with a poor description of the reaction thermodynamics of the system as they may require users to define a constant value of reaction enthalpy for each reaction.

On the other hand, some plasma-chemistry solvers are being developed based on more complex thermochemical solvers [50,51]. One of the most used is Cantera [53], a free-ware open-source code highly used in the chemistry modeling community, making use of its rigorous system thermodynamic modeling and customizability. From the reaction thermodynamics perspective, Cantera offers the possibility to include species thermodynamic properties as functions of the gas temperature, thus influencing the heat release (or absorbtion) from reactions during the computations. The plasma-chemistry solvers based on Cantera include a Boltzmann solver, e.g. BOLOS [50] and its C++ version CppBOLOS [51], to manage the electron collisional processes but are not including custom defined non-equilibrium reactions nor power coupling models to input power density signals to the EBE solver.

To enlarge the physical representativeness of plasma-chemistry models, a novel solver, SPPARK (Simulation Platform for Plasma Assisted Reactive Kinetics), has been developed by the Authors based on a Cantera - Bolsig+ coupling. The coupling aim is granting chemical rigorousness and flexibility of application together with full customizability of the physical hypothesis influencing the EBE solution with the objective of filling the gaps between the two families of plasma-chemistry solvers, providing researchers with an open-source environment to simulate complex plasma-chemical processes. In this sense, SPPARK is able to: include electron collision processes in Cantera chemistry sets; include non-equilibrium reactions with arbitrary complex reaction rate constants; make use of power coupling models or electric circuit schemes to extract the electron solicitation to feed Bolsig+ with; deal with eterogeneous plasma-gas mixtures; include multizone

modeling of plasma sources; use the formulations available in Cantera to represent the species thermodynamic properties as a function of gas temperature.

The present work describes the SPPARK solver, the plasma-chemistry models currently included, and the methodology adopted for Cantera-Bolsig+ coupling. A validation of the software is also presented comparing SPPARK computations against data obtained with the widely adopted ZDPlaskin [48] code using reaction mechanisms describing a N_2 plasma and an Ar plasma under multiple operating conditions. Moreover a simple CH_4 splitting model is included to further argue on the necessity including a rigorous thermodynamic representation of the system for applications with large ranges of temperature variability.

3.4 Model description

A plasma-chemistry model aims to the detailed representation of the chemical mechanisms that occur in a plasma. The goal can be reached by describing the phenomena existing in the plasma discharge and the effects that these have on the state of the gas. First of all, electron collisions should be included in the model as they allow energy to be transferred from electrons to heavy particles. These collisions, together with the electromagnetic field intensity, are responsible for the overall behaviour of the electron population as a swarm of particles (*i.e.* their mean energy $\langle\varepsilon\rangle$, their diffusion coefficient D_e, their mobility coefficient μ etc.). Through collisions, which are considered as chemical reactions, electrons can drive energy to the mean kinetic energy of the gas particles (their temperature) or to their internal energy (*i.e.* exciting their electronic state). Species produced by electron collisions are reacting in the gas system. As these particles state is shifted from the macroscopic equilibrium (*i.e.* the equilibrium state defined by the gas temperature in low ionization plasmas), the rates of the reactions they are involved in are generally a function of the overall plasma state (*i.e.* are also dependant on the electron swarm coefficients) and so cannot be analytically expressed through simple Arrhenius rate constants. All of these aspects are addressed in SPPARK through the Cantera-Bolsig+ coupling rationale schematically represented in Figure 3.4.1.

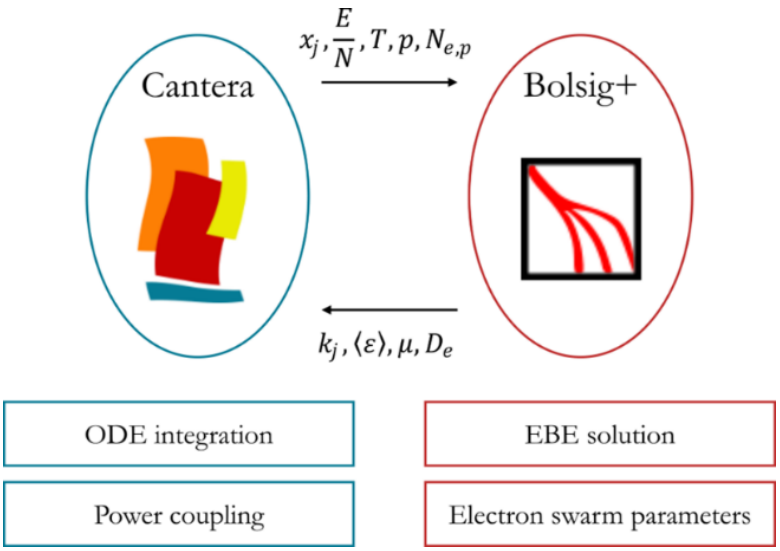

Figure 3.4.1 Cantera-Bolsig+ coupling conceptual scheme. Boxed are represented the specific tasks attributed to each solver. Arrows indicate the data transfer between the two: the system thermodynamic state and electron solicitation from Cantera to Bolsig+ and the electron swarm parameters from Bolsig+ to Cantera.

The coupling involves Bolsig+ to solve the EBE, obtaining the EEDF from which the electron collisions rates (k_j) and the kinetics parameters can be derived, and Cantera to compute the electron solicitation for Bolsig+ through power coupling models and to time integrate the ODEs to obtain the new plasma state (its temperature T, pressure p, molar fraction x_j and electron density $N_{e,p}$) at each timestep.

In this section, the theoretical model representing electron collisions, non-equilibrium processes, power coupling models, electron effects on gas temperature and heterogeneous plasma interactions are described. Furthermore, the adopted strategies to include electron collisions and non-equilibrium reactions in objects derived from Cantera classes together with the methodology of synchronized coupling of Bolsig+ during the time integration are introduced.

3.4.1 Plasma chemical kinetics

Electron collisions are the driving force of the non-equilibrium chemical processes taking place in a plasma. In general, electron collisions are considered as binary reactions with the heavy species being targeted by the impact assumed to be stationary [54]. By convention, collisions can be classified as: elastic when the energy ceded by the colliding electron is conveyed in the kinetic energy of the heavy target particles; inelastic when the energy transfer from the electron results in a variation of the internal energy of the target particle. Macroscopically, elastic collisions lead directly to a raise of the gas temperature whilst the inelastic collisions in the production of new chemical compounds (generally unstable); these can be electronically excited states of a species, rovibrationally excited states of

molecules, ions and radicals. Each of the produced species will then interact with the whole system of particles resulting in a superposition of thermochemical, electron kinetics and non-equilibrium mechanisms. The last two reaction mechanisms require the definition of rate constants (k_j).

Electron collisions rate constants are obtained directly from their cross-section by the following integral formulation:

$$k_j^{coll,f} = \gamma \int_0^{\infty} \varepsilon\, \sigma_j(\varepsilon) F(\varepsilon)\, d\varepsilon \tag{3.1}$$

where, $\sigma_j(\varepsilon)$ (m^2) represents the cross-section of the j-th collision, $F(\varepsilon)$ $(eV^{-3/2})$ the EEDF, ε (eV) the kinetic energy of the colliding electron and $\gamma = \left(\frac{2e}{m_e}\right)^{1/2}$ a constant with e (C) and m_e (kg) electron charge and mass respectively. In case of super-elastic collisions (i.e., collisions in which energy is transferred from excited or metastable particles back to the electrons, consistent with microscopic reversibility), the inverse rate constant is determined through the following expression [47] from the direct (excitation) collision cross-section (σ_j).

$$k_j^{coll,i} = \frac{g_h}{g_l} \cdot \gamma \int_0^{\infty} \left(\varepsilon - U_j\right) \sigma_j\left(\varepsilon - U_j\right) F(\varepsilon)\, d\varepsilon \tag{3.2}$$

where $\frac{g_h}{g_l}$ is the statistical weight ratio between the forward collision products (g_h) and the forward collision reactants (g_l) and U_j (eV) is the threshold energy of the excitation collision.

The EEDF can be obtained by solving the electron Boltzmann equation [47] (a more detailed description is provided in Section 2.2):

$$\frac{\partial f}{\partial t} + \vec{v} \cdot \nabla f - \frac{e}{m_e} \vec{E} \cdot \nabla_v f = C \tag{3.3}$$

where f is the electron distribution in the six-dimensional phase space, $\vec{x}$ and $\vec{v}$ are respectively the vector of space and velocity coordinates, $\vec{E}$ is the electric field and C is the collision integral term of the equation.

On the other hand, the non-equilibrium reactions rate constants are usually expressed in analytical formulations depending on both the gas overall thermodynamic state and electron kinetic parameters (*i.e.* electron temperature, mobility and diffusion coefficients) also obtained from the EEDF [47]:

$$k_j^{neq} = k_j^{neq}\left(T_{gas}, T_e, \mu_e, D_e, \dots\right) \tag{3.4}$$

3.4.2 Power coupling models

As described in [47], the external solicitation required for the EEDF equation solution is the reduced electric field E/N (with E electric field magnitude and N heavy particles number density). In general, the reduced electric field is laboriously measured, thus, to extend experimental data availability, deposited power density values are more often used as the electron solicitation [3,55,56]. For this reason, to solve the EEDF equation, which explicitly depends on the reduced electric field value [47], using the deposited power density, a correspondence between power densities and reduced electric fields values is required. This is obtained through power coupling models. Among the available ones, two are here described. The first algebraic model utilizes the Local Field Approximation (LFA) [54] to obtain E/N (Td) directly from the deposited power density:

$$\frac{E}{N} = \frac{1}{N}\sqrt{\frac{\widetilde{P_p}}{N_{e,p} e \mu_e}} \cdot 10^{21} \tag{3.5}$$

where N is the heavy particles number density (m^{-3}), $\widetilde{P_p}$ is the deposited power density in the plasma (W/m^3), $N_{e,p}$ is the electron number density (m^{-3}) in the plasma and μ_e is the electron mobility $(m^2/(V \cdot s))$. This relation is obtained by the Joule heating equation:

$$\widetilde{P_p} = \sigma E^2 \tag{3.6}$$

where the approximation $\sigma \approx N_{e,p} e \mu_e$ is introduced making the whole power coupling model hold for low excitation frequencies [54].

The second model is generally more accurate as it relies on the homogeneous Local mean Energy Approximation (LEA) [57] (see Section 2.3) from which the following equation can be obtained and solved to compute the mean electron energy $(\langle \varepsilon \rangle - eV)$:

$$\frac{d\langle \varepsilon \rangle}{dt} = \frac{1}{N_{e,p}}\left(\frac{\widetilde{P_p}}{e} - Q_{el} - Q_{in} - \langle \varepsilon \rangle \frac{dN_{e,p}}{dt}\right) \tag{3.7}$$

where Q_{el} and Q_{in} are the powers deposited (lost) by electrons respectively in elastic and inelastic collisions (eV/s). Both Q_{el} and Q_{in} can be computed from the EEDF [47] as follows:

$$Q_{el} = N_{e,p}N \sum_{j=elastic} \gamma x_j \frac{2m_e}{M_j} \int_0^{\infty} \left[\sigma_j \left(\varepsilon^2 F + \frac{K_b T}{e} \frac{\partial F}{\partial \varepsilon}\right)\right] d\varepsilon \tag{3.8}$$

$$Q_{in} = N_{e,p}N \sum_{j=inel} U_j x_j \left(y_j^{low} k_j^{coll,f} - y_j^{up} k_j^{coll,i}\right) \tag{3.9}$$

Where x_j and M_j are respecitvely the molar fraction (considering just the heavy particles) and the mass (kg) of the chemical species involved in the j-the collision, K_b the Boltzmann constant (J/K), T the gas temperature, U_j the energy threshold of the j-th collision (*i.e.* the chemical bond energy for a dissociation, the energy gap between two electronic shells, etc…) and y_j^{low} and y_j^{up} the population fractions in the lower and upper excited states. The E/N value is then obtained by matching mean electron energy obtained by equation 3.7 with the one obtained by [47]:

$$\langle \varepsilon \rangle = \int_0^{\infty} \varepsilon^{\frac{3}{2}} F(\varepsilon)\, \mathrm{d}\varepsilon \tag{3.10}$$

with F being obtained by the solution of the EEDF equation with the target E/N value as an input.

3.4.3 Heterogeneous phase plasma interactions

In many systems the generated plasma phase is in contact with electrodes and reactor walls. For this reason, including heterogeneous phase plasma-solid interaction is fundamental to comprise the additional charged particles losses. Moreover, many plasma discharges cannot be considered to be homogeneous, being characterized by an admixture of gas and plasma phases (Figure 3.4.2). The plasma-boundary interactions and plasma-gas mixtures models adopted by the Authors are here described.

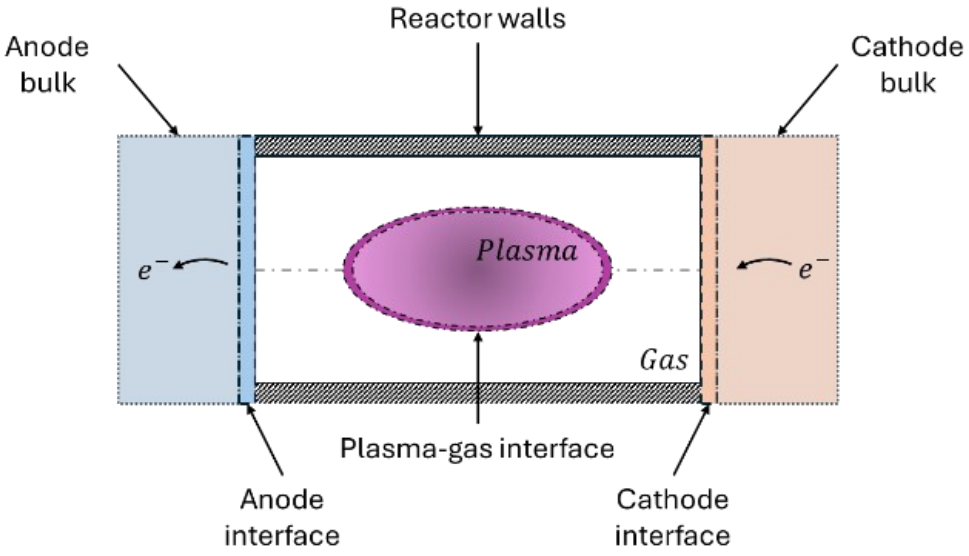

Figure 3.4.2 Abstract representation of a plasma reactor including walls, electrodes and plasma-gas interfaces

3.4.3.1 Plasma-boundary interactions.

Heterogeneous plasma-solid interactions can be described by means of surface interactions at the interfaces between the plasma and the solid phases. These interfaces can be represented as catalytic solid interfaces being characterized by an area (A) and a density of active sites (S_d). In addition, the loss mechanisms can be included as surface reactions occurring on the surface of the catalyst. The here presented model refers to two types of plasma-solid interfaces: *Walls* and *Electrodes*. *Wall* interfaces allow species to stick to their surfaces introducing additional loss terms for the species interacting with them. On the other hand, *Electrode* interfaces are characterized by permeability to electrons. A solid phase must then be included to function as a reservoir of solid electrons to be ceded (in a cathode electrode) or to be extracted (in an anode electrode) from the *Electrode* interfaces. The plasma solid interactions are particularly relevant to include charged particles losses to the system boundaries. The model adopted by the Authors allows to consider these losses through the definition of a transport loss frequencies (ν_L) and to determine the loss rate constant; in the following example, a general mechanism of electron loss to an anode interface (represented by an anode active site $A(S)$) is presented.

$$\begin{cases} e^- + A(S) \overset{k_0}{\Rightarrow} A(S)^- \overset{k_1}{\Rightarrow} A(S) + e^-_{anode} \\ k_0 = \nu_L \cdot \dfrac{V}{A} \cdot \dfrac{1}{S_d} \\ k_1 = k_1 \gg k_0 \end{cases} \tag{3.11}$$

In the above expression k_0 represents the plasma-to-surface loss mechanism rate constant, whilst k_1 represents the anode restoration rate constant with V being the plasma volume. The k_1 constant is arbitrarily chosen to be much greater than k_0 to ensure the instantaneous restoration of the active sites of the electrode.

Many expressions to include charged particles transport losses ν_L in 0D plasma-chemistry modeling have been presented by Alves et al. depending on the dominant discharge phenomena [58].

3.4.3.2 Plasma-gas mixtures.

To extend the applicability of the model to non-homogeneous plasma discharges two approaches are here introduced. The first one makes use of the same principle used for plasma-solid interactions. If a plasma-gas interface can be properly defined, the transport of species between the two phases can be modelled introducing a fictitious surface of voids ($V(S)$). Doing so, a transport frequency (ν_τ) can be used to model the exchanges between the two phases as in the following example:

$$\begin{cases} X^{(p)} + V(S) \underset{k_1}{\overset{k_0}{\Leftrightarrow}} V(S) + X^{(g)} \\ \quad k_0 = \nu_\tau^{(p)} \cdot \dfrac{V_p}{A} \cdot \dfrac{1}{S_d} \\ \quad k_1 = \nu_\tau^{(g)} \cdot \dfrac{V_g}{A} \cdot \dfrac{1}{S_d} \end{cases} \tag{3.12}$$

with k_0 being the plasma-to-gas transport rate constat, k_1 the gas-to-plasma one and $X^{(p)}$, $X^{(g)}$ referring to the same X species considered in the plasma and gas phase respectively. V_p and V_g here represent the plasma and gas phases volumes respectively whilst $\nu_\tau^{(p)}$ and $\nu_\tau^{(g)}$ the plasma-to-gas and gas-to-plasma transport frequencies.

If the plasma-gas interface cannot be easily defined (*i.e.* the two phases are strongly mixed), a second approach can be used by introducing a volume weighted approximation. Assuming that free electrons are present only in the homogeneous plasma phase, the EBE can be solved by considering a higher density electron population obtained by the global (mean) electron density as:

$$N_{e,p} = \frac{N_e}{\varphi} \tag{3.13}$$

where N_e is the electron number density in the whole volume and the term $\varphi = \frac{V_p}{V_{tot}}$, with V_p the plasma volume and V_{tot} the total volume, is the plasma to total volume

ratio. Under this approximation, the collisions rate constants and electron kinetic parameters are calculated as in a pure-plasma homogeneous system, but their overall effect is downscaled by considering an available population of N_e particles to be able to support the non-equilibrium processes.

3.4.4 Implementation in Cantera

The previous sections highlighted the need of a closed coupling between Cantera and Bolsig as summarized in Figure 3.4.3.

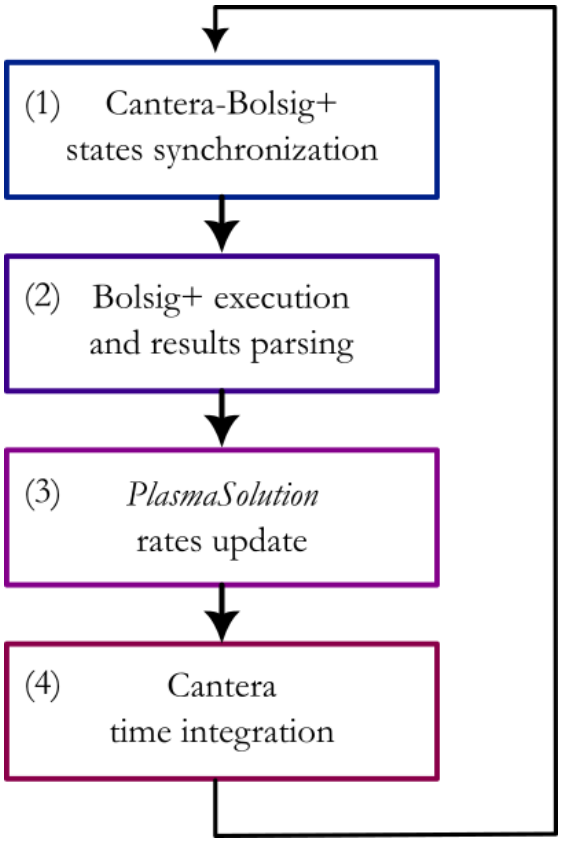

Figure 3.4.3 Single time-step Cantera-Bolsig+ coupling algorithm. At the beginning of the time-step the Bolsig+ gas state is synchronized (1) accordingly with the results obtained by Cantera in the ODE time integration together with the reduced electric field value relative to the simulation time (either imposed or computed by the power coupling model of choice). Bolsig+ is then called (2) to solve the electron Boltzmann equation and extract the electron transport and kinetic parameters which are parsed and fed back to the PlasmaSolution object (3) to update the rate reaction constants. Ultimately, the time integration of the ODEs at the current simulation time is effectuated (4) providing the results necessary for the new time-step

Bolsig+ is freely available as an executable file. Its command line operated version elaborates the user requests delivered in a text file. The input file contains the hypothesis on the electron kinetics model, the path to the cross-section data file and the path to the output text file. To couple Cantera and Bolsig+ in a python environment, a python wrapper to write the inputs, execute the simulation and read the results has been developed. To ensure the consistency of the electron

kinetic simulation with the plasma-gas system state the wrapper consists of a system of python classes representing species, reactions and the whole particles system which allows the runtime coupling of the two codes.

In SPPARK the single timestep operations are executed as follows and summarized in Figure 3.4.3: at first a synchronization of the Bolsig+ hypothesis to a PlasmaSolution (the SPPARK Solution class inheriting its attributes and methods from the Cantera *Solution* class) state is performed; secondly, a call of Bolsig+ computes the electron collisions rates and the electron kinetics parameters for the non-equilibrium reaction rates, which are parsed from the Bolsig+ output text file; non-equilibrium rates are computed and the numerical values of electron collisions and non-equilibrium rate constants are updated in the *PlasmaSolution* object; afterwards the time integration in Cantera is carried out obtaining a new state for the *PlasmaSolution* object allowing the next timestep to occur. The runtime coupling of the two solvers is obtained through the *ExtensibleReactor* classes available in Cantera by modifying the constitutive equations to consider the plasma effects on the system.

Depending on the application, users can select the *ExtensibleReactor* of choice and apply the same coupling procedure previously described.

To further clarify the procedures required to consider electron collisions and non-equilibrium reactions in Cantera, represented by point (3) in Figure 3.4.3, Figure 3.4.4 provides an in-depth scheme of the rate constants update. These operations are executed in the *after_get_state* method of the *ExtensibleReactor* class before the evaluation of the ODEs terms is performed in its *after_eval* method.

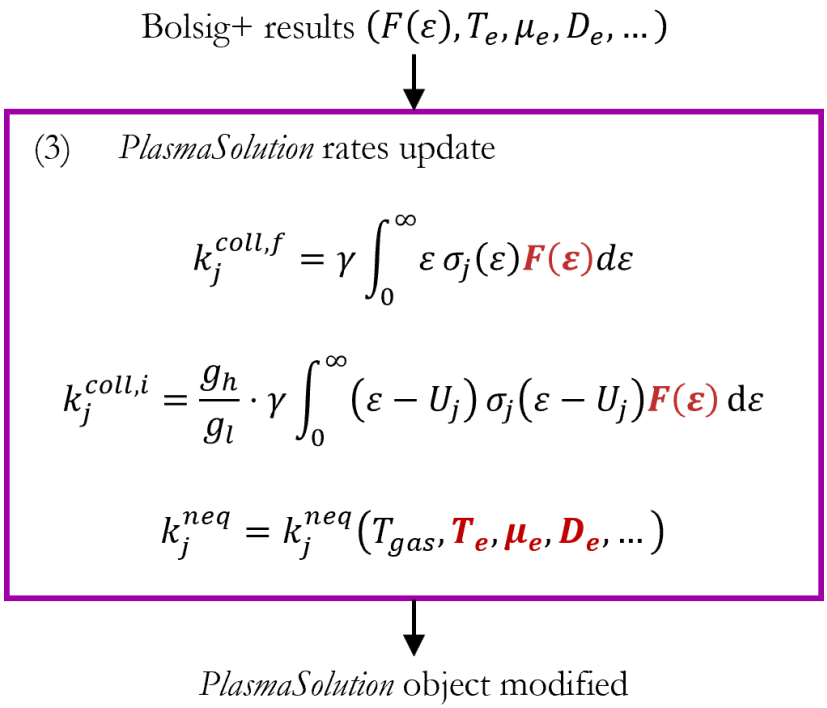

Figure 3.4.4 Detailed description of the Bolsig+ results coupling to reaction rate constants. The terms highlighted in red are results directly parsed from the Bolsig+ output files which are used in the *after_get_state* method of the *ExtensibleReactor* class of Cantera to modify the rate constants of electron collisions and non-equilibrium reactions.

3.4.4.1 Plasma chemical kinetics

The electron collision rate constants computation requires the integration of the cross-section of the reaction weighted on the EEDF, as described in equation 3.1. Concurrently, non-equilibrium reactions are strongly dependent on the electron kinetic parameters. In Cantera the definition of user defined rate constants is implemented by the use of *CustomRate* and *ExtensibleRate* classes. The first one presents a strong limitation since it allows the definition of a custom function for the rate computation only dependent on the gas temperature. The other can take all the thermodynamic data from a *Solution* object and use it to evaluate the rate. Although the latter is a positive feature, the implementation of a new rate requires a new class definition for each additional reaction, which is not suitable for large chemistry sets. By virtue of these considerations, two different approaches have been applied for electron collisions and non-equilibrium reactions. The first are treated as constant Arrhenius rates whose values are updated each timestep using the results obtained from Bolsig+. For this reason, the reactions are first defined through the cross-section data in the Bolsig+ input text file and then coupled to Cantera *Reaction* objects. Additionally, users can selectively choose which subset of the electron collisions used in Bolsig+ to compute the EEDF to include in the ODE time integration. For the second type of reactions, the customized class *CustomPlasmaReaction* is introduced. This class takes the

reaction equation, a reaction order and a python function as inputs. The python function is user defined and returns the rate constant value. Each instance of this class is then associated with a Cantera *Reaction* object in a *PlasmaSolution* object whose rate is updated at each timestep. Furthermore, electron inelastic collisions and some non-equilibrium reactions (*i.e.* some radiative relaxations of electronically excited species) should not directly influence the gas temperature computation. For this reason, all the inelastic collisions and the subset of *CustomPlasmaReaction* objects are extracted in the *PlasmaSolution* class as no-heat reactions, whose reaction enthalpy will not be considered in the heat equation.

3.4.4.2 Power coupling models.

To include the two power coupling models (equations 3.5 and 3.7) in the runtime coupling, they have been introduced in two *ExtensibleReactor* classes. The LFA model (equation 3.5) is simply included in the *after_get_state* method of the class whilst the LEA model (equation 3.7) is included in its *after_eval* method.

3.4.4.3 Heterogeneous plasma interactions.

To ensure the maximum freedom in modeling transport phenomena, an additional *PlasmaInterface* class (inheriting from the Cantera *Interface* class) has been introduced. The class has the possibility of including *CustomPlasmaReaction* objects defining the rate constants of transport losses or gains of the adjacent phases. Regarding the *Electrode* boundaries the *PlasmaInterface* is coupling the *ExtensibleReactor* containing the *PlasmaSolution* with a *ConstPressureMoleReactor* containing a *fixed-stoichiometry* phase representing the solid electrode phase. On the other hand, the gas-plasma interface for plasma-gas mixtures modeling can be represented by a *PlasmaInterface* as well connecting two *ExtensibleReactors* for the two *PlasmaSolutions*. Even if it does not include charged particles, the choice of representing the gas through a *PlasmaSolution* allows the inclusion non-equilibrium reactions that may occur between the transported species.

3.5 Validation Results

The code validation has been performed against the ZDPlasKin solver [48] on three chemistries. To ensure the comparability of the results, the same conditions available in the model adopted by ZDPlasKin were replicated in SPPARK. The first chemistry refers to an N_2 discharge under a simple custom power pulse solicitation. The second chemistry refers to an Ar plasma ignited under a continuous (DC) voltage signal, coupled to the chemistry through a simple circuit model, considering a multicomponent EBE solution and charged species losses due to ambipolar diffusion. The third chemistry, referring to a CH_4 discharge, is ultimately presented to introduce an example to further discuss on the potential

differences in non-isothermal plasma-chemistry simulations when adopting a rigorous gas thermodynamic approach.

3.5.1 N_2 discharge

A homogeneous ($\varphi = 1$), closed Perfectly Stirred Reactor (PSR) with a volume of 1 m^3 was chosen to represent the discharge domain. The adopted chemistry set represents a N_2 discharge at 1 bar and is freely available in the ZDPlasKin website. The gas temperature was set constant at 298.15 K. The electron solicitation was provided as deposited power density (Figure 3.5.1) under the LFA model as additional ODEs cannot be included in the ZDPlasKin equation system.

In Figure 3.5.2 the results on the electron density and reduced electric field computed by SPPARK are shown against the same values obtained by ZDPlasKin. Figure 3.5.3 shows the computations of both solvers on heavy species number densities. The results show a good agreement between the two solvers computations. The maximum relative errors between the two have been calculated and are shown in Figure 3.5.4 proving the almost exact equivalence in the two different solvers. Replicating the same approach, the code has been tested on multiple cases with varying power signals, pressure and temperatures showing a good agreement between results (Figure 3.5.5, Figure 3.5.6 and Figure 3.5.7). Since SPPARK employs an adaptive time-stepping scheme both for computation and for storing results, while ZDPlasKin restricts output to user-defined time instants, a time interpolation of the SPPARK simulation results was performed to enable a direct comparison at the same output times. It is worth noting that the minor discrepancies observed between the results may be attributed to this interpolation procedure. The SPPARK executions took an average of 3 minutes and 31.12 seconds whilst the ZDPlasKin executions took 1 minute and 2.81 seconds.

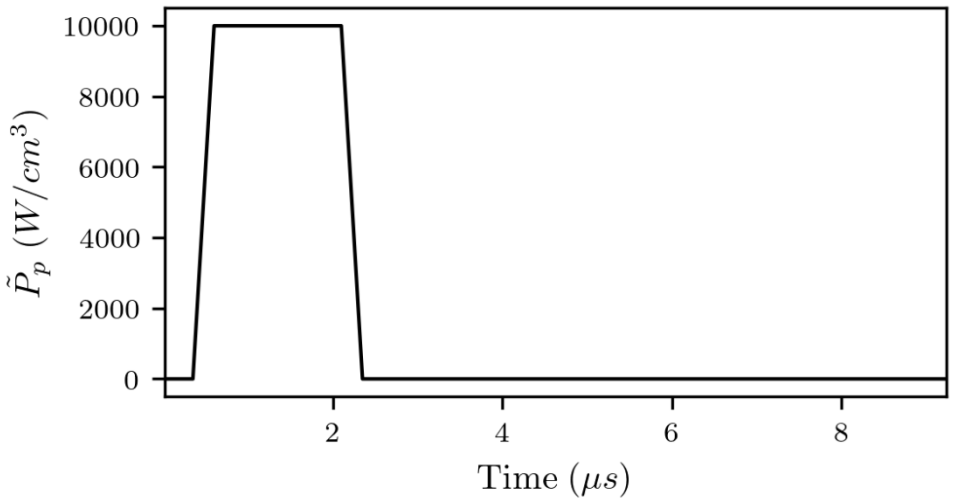

Figure 3.5.1 Power density signal provided to the simulation

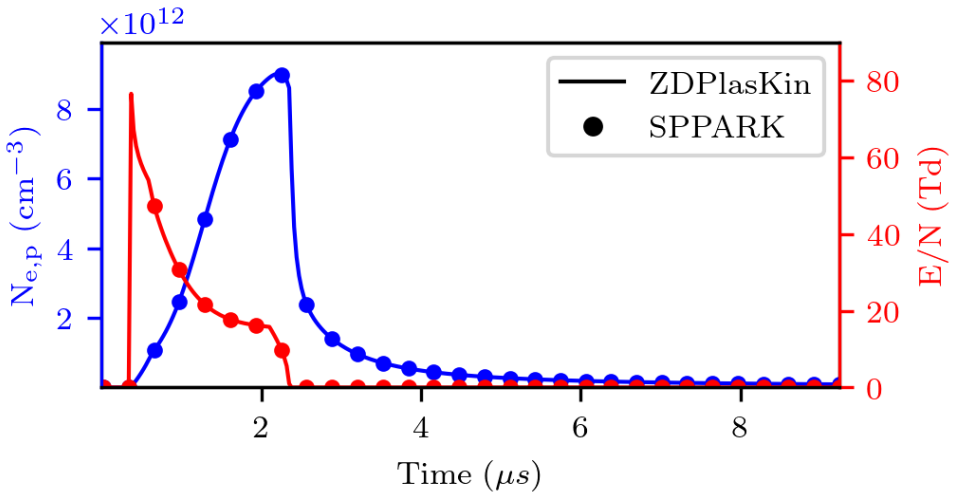

Figure 3.5.2 Electron number density (blue) and reduced electric field (red) results comparison between ZDPlasKin (continuous line) and SPPARK (dots) simulations for a pure N_2 plasma at a constant temperature of 298.15 K and 1 bar of pressure

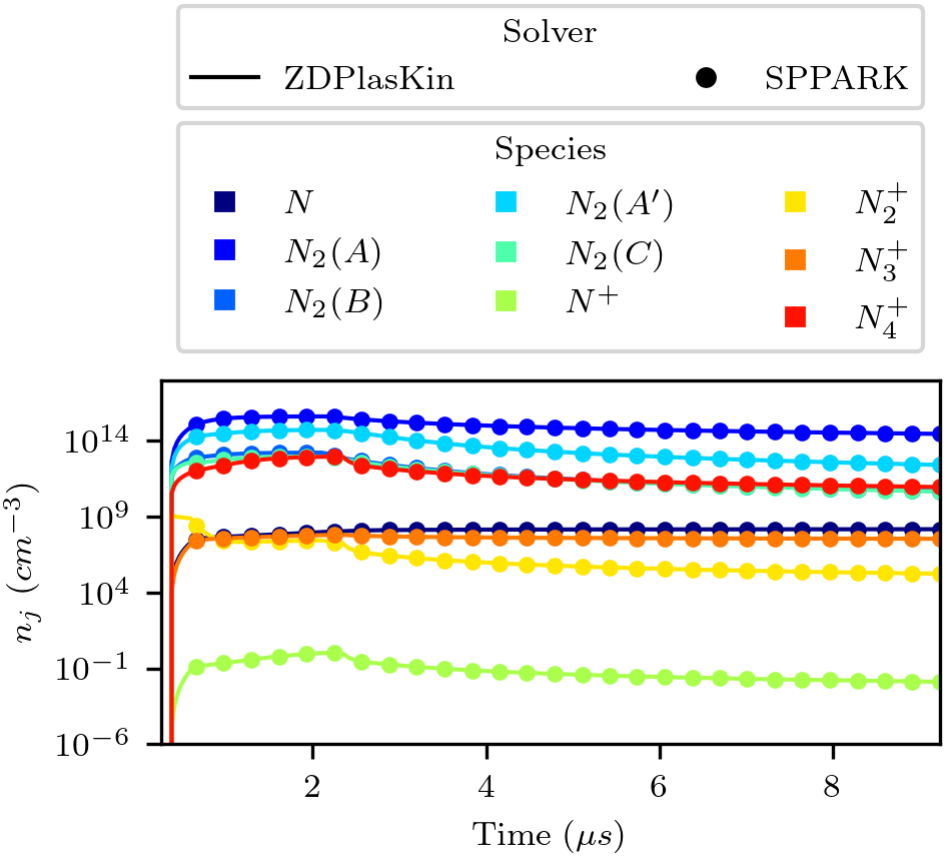

Figure 3.5.3 Heavy particles number densities results comparison between ZDPlasKin (continuous line) and SPPARK (dots) simulations for a pure N_2 plasma at a constant temperature of 298.15 K and 1 bar of pressure.

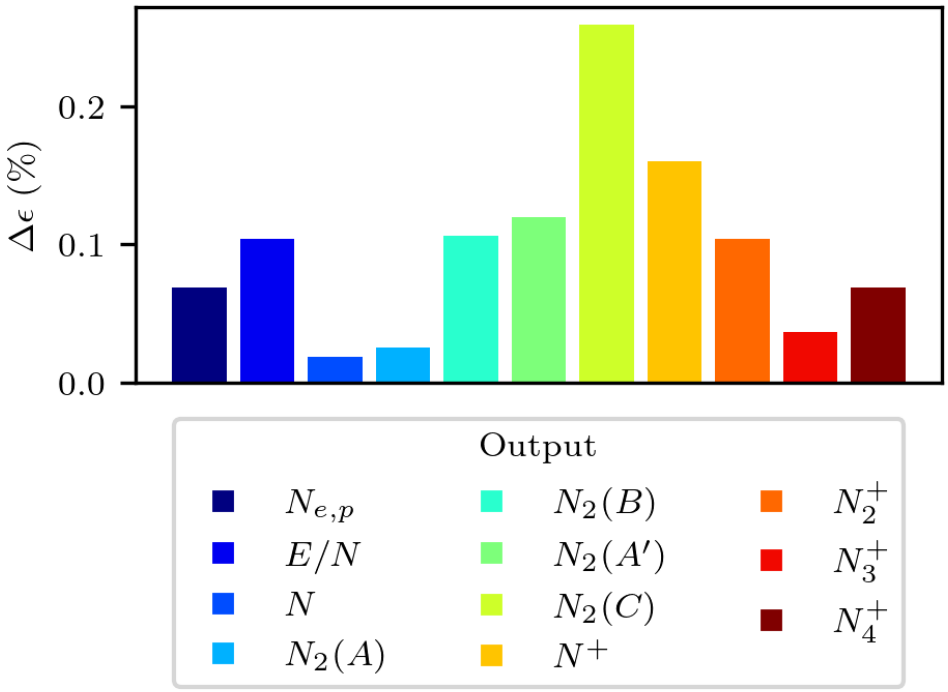

Figure 3.5.4 Maximum relative error (in percent) between the SPPARK and ZDPlasKin computation

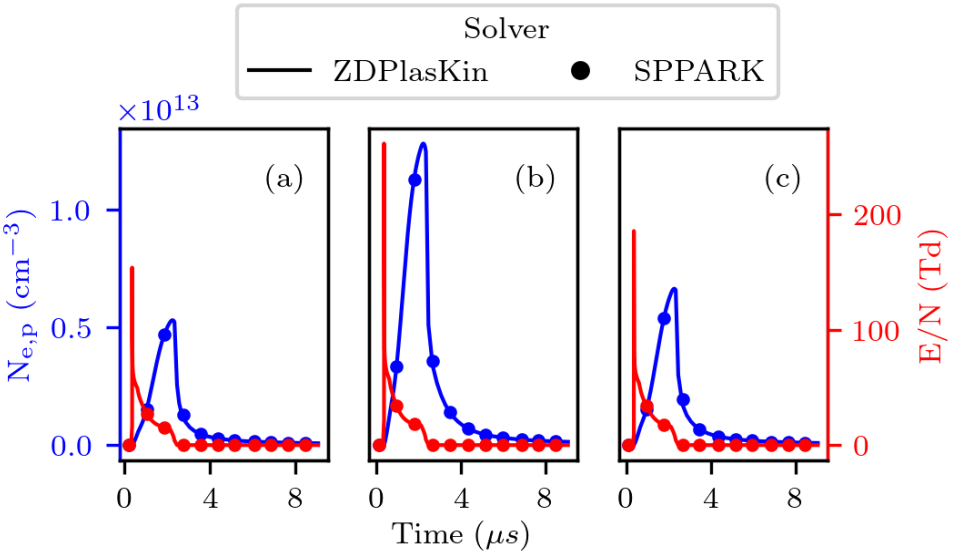

Figure 3.5.5 Electron number density (blue) and reduced electric field (red) results comparison between ZDPlasKin (continuous line) and SPPARK (dots) simulations for a pure N_2 plasma at: (a) a constant temperature of 298.15 K, 2 bar of pressure and 10^4 W/cm^3 of peak deposited power density; (b) a constant temperature of 500 K, 1 bar of pressure and 10^4 W/cm^3 of peak deposited power density; (c) a constant temperature of 298.15 K, 1 bar of pressure and $7.5 \cdot 10^3$ W/cm^3 of peak deposited power density.

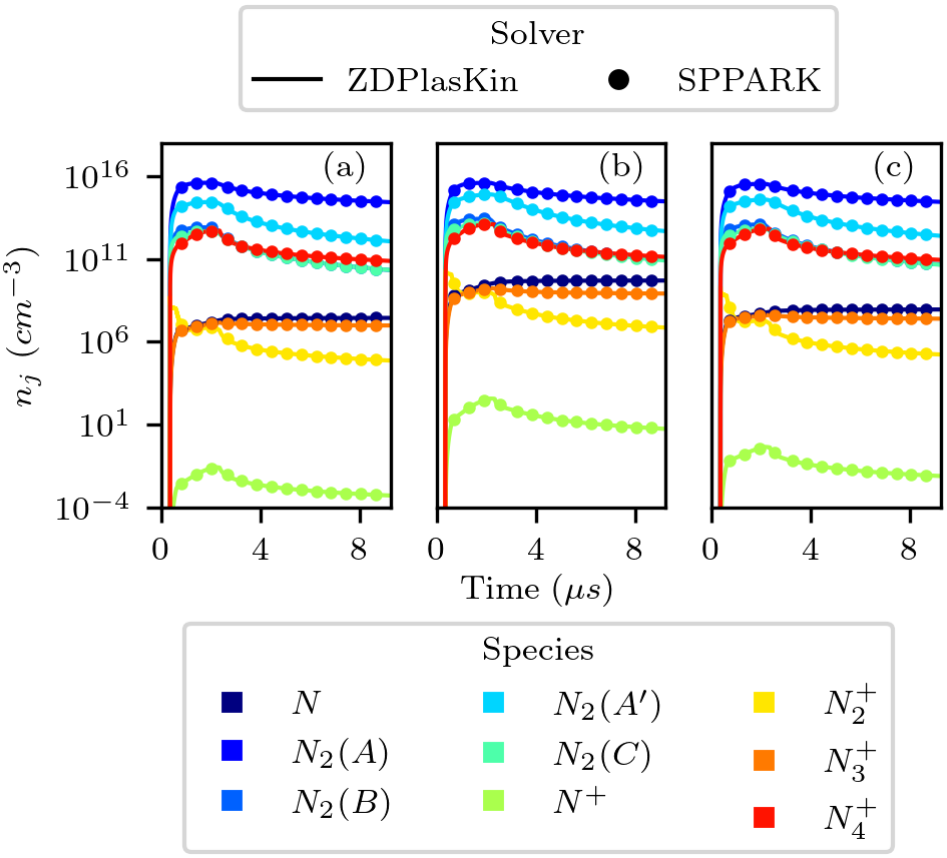

Figure 3.5.6 Heavy particles number densities results comparison between ZDPlasKin (continuous line) and SPPARK (dots) simulations for a pure N2 plasma at: (a) a constant temperature of 298.15 K, 2 bar of pressure and 10^4 W/cm^3 of peak deposited power density; (b) a constant temperature of 500 K, 1 bar of pressure and 10^4 W/cm^3 of peak deposited power density; (c) a constant temperature of 298.15 K, 1 bar of pressure and $7.5 \cdot 10^3$ W/cm^3 of peak deposited power density.

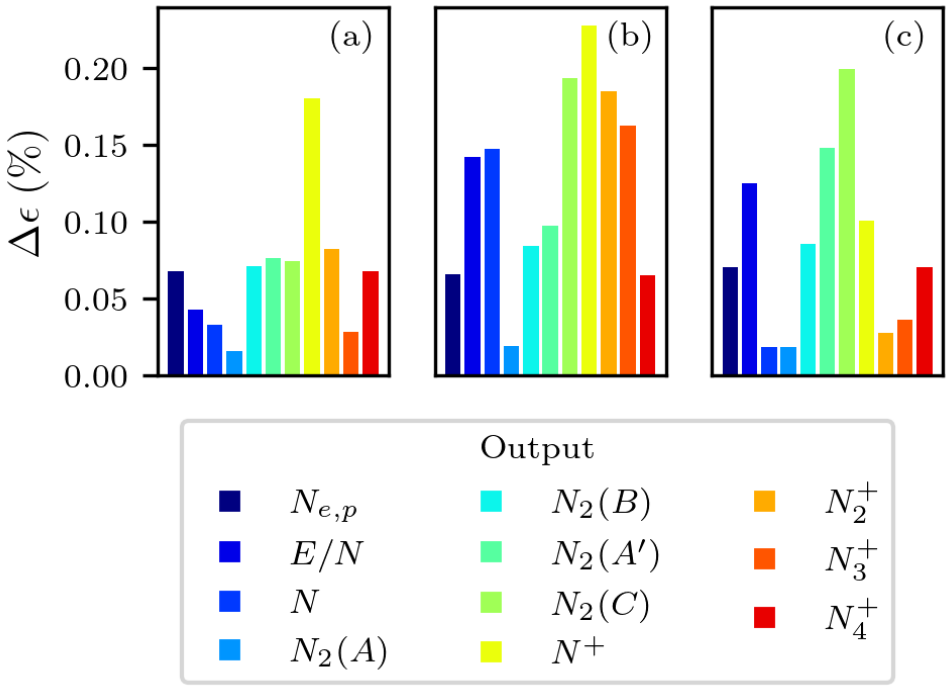

Figure 3.5.7 Maximum relative error (in percent) between the SPPARK and ZDPlasKin computations at: (a) a constant temperature of 298.15 K, 2 bar of pressure and 10^4 W/cm^3 of peak deposited power density; (b) a constant temperature of 500 K, 1 bar of pressure and 10^4 W/cm^3 of peak deposited power density; (c) a constant temperature of 298.15 K, 1 bar of pressure and $7.5 \cdot 10^3$ W/cm^3 of peak deposited power density.

3.5.2 Ar discharge

A plasma chemistry set comprising charged particles transport loss mechanisms due to ambipolar diffusion in an Ar plasma is available for ZDPlasKin. The considered plasma system represents a homogeneous Ar plasma at a pressure of 100 torr and a constant temperature of 300 K in a cylindrical reactor having a radius (r) of 4 mm and a gap (d) between electrodes of 4 mm. The electron solicitation was provided in the form of reduced electric field values by coupling a simple circuit model composed of a DC voltage generator and a series of a ballast resistor and a plasma resistance representing the discharge, while neglecting the voltage drop across the sheaths, to the plasma-chemistry model. Even if the circuit model might not be the best representation of a plasma-electrical behaviour, it has been implemented to further compare SPPARK computations against ZDPlasKin. The DC voltage signal (U) was set at $1\,kV$ with a ballast resistor (R) of $1\,k\Omega$. The plasma resistance was calculated through the plasma conductivity ($\sigma \approx N_{e,p} e \mu_e$) accordingly with the time-evolving electron density and mobility. In SPPARK, the circuit is coupled with the chemistry by providing the circuit net to an *ExtensibleIdealGasMoleReactor* object from Cantera, adapted to explicitly solve the circuit voltage and current equations and the reduced electric field has been computed from the voltage drop across the plasma resistance. This

feature allows to generalize the applicability of the approach to an arbitrary circuit net which is automatically translated from its components and circuit nodes definition to the constitutive circuit equations. To ensure a smooth evolution of the plasma conductivity in time, the time step has been limited to a maximum of 1 ns. In ZDPlasKin the coupling has been performed as implemented in the in the reference example as expressed in equation 3.14.

$$\begin{cases} J = e(\pi r^2) N_e v_d \\ \left(\frac{E}{N}\right)_{\text{test}} = \frac{1}{N} \frac{U}{d + \frac{RJ}{10^{-17} E^{(\tau)} + 10^{-99}}} \\ \frac{E}{N}^{(\tau+1)} = 0.5 \left[\left(\frac{E}{N}\right)_{\text{test}} + \left| \left(\frac{E}{N}\right)_{\text{test}} \right| \right] \end{cases} \tag{3.14}$$

where J is the electron current (A), e is the electron charge (C), N_e is the electron number density (cm^{-3}), v_d is the electron drift velocity, N is the neutral particles density (cm^{-3}), r and d are respectively the discharge radius and diameter (cm), $E^{(\tau)}$ and $E^{(\tau+1)}$ are respectively the electric field at the current time-step (τ) and at the next time-step $\left(\frac{V}{cm}\right)$.

The ambipolar diffusion losses were included using two different approaches for ZDPlasKin and SPPARK. The ZDPlasKin model treats these as homogeneous phase reactions leading to the production of wall-attached species. In SPPARK they were included as plasma-boundary interactions (described in Section 3.4.3.1), considering the whole external surface of the plasma phase as available for the charged species losses. To better clarify how such reactions are included in SPPARK the example for the ambipolar diffusion losses is provided (equation 3.15).

$$\begin{cases} \Lambda = \left(\frac{2.405}{r}\right)^2 + \left(\frac{3.1410}{d}\right)^2 \\ \nu = 1.52 \frac{760}{p} \frac{T_g}{273.15} \frac{T_e}{11600} \Lambda \\ k(T_g, T_e, p) = \nu \frac{V}{A} \frac{10^3}{S_d N_a} \end{cases} \tag{3.15}$$

where V is the reactor volume (m^3), A is the total external surface (m^2), S_d is the surface active-sites density $(kmol/m^2)$, N_a is the Avogadro constant, T_g is the gas temperature (K), T_e is the electron temperature (K), p is the gas pressure $(Torr)$ and k is the rate constant for the ambipolar diffusion losses (cm^3/s). This expression can be directly implemented in a Python function giving the k value as

a return to be passed as an argument to the *PlasmaCustomReaction* object representative of the ambipolar diffusion loss reaction.

To ensure the full comparability of the models, a two-step of comparison was performed. The first step concerned a homogeneous phase model, obtained by neglecting the transport losses by ambipolar diffusion. In the second one, the ambipolar diffusion loss mechanisms were included to evaluate the equivalence of the two approaches.

In Figure 3.5.8 and Figure 3.5.9 the computed electron density together with the reduced electric field values and the heavy species number densities obtained in the two simulations (A – no-ambipolar diffusion losses and B – including the ambipolar diffusion losses) are respectively shown. In both cases, the results show a good agreement (Figure 3.5.10) between ZDPlasKin and SPPARK with the discrepancies possibly due to the time interpolation of the results in SPPARK (as in Section 3.5.1) and to the different approach in the circuit to chemistry coupling. The simulation in SPPARK took 4 minutes and 49.13 seconds to execute for the case without ambipolar diffusion losses and 5 minutes and 24.41 seconds for the case including ambipolar diffusion losses whilst in ZDPlasKin tool 18.78 seconds and 27.51 seconds respectively.

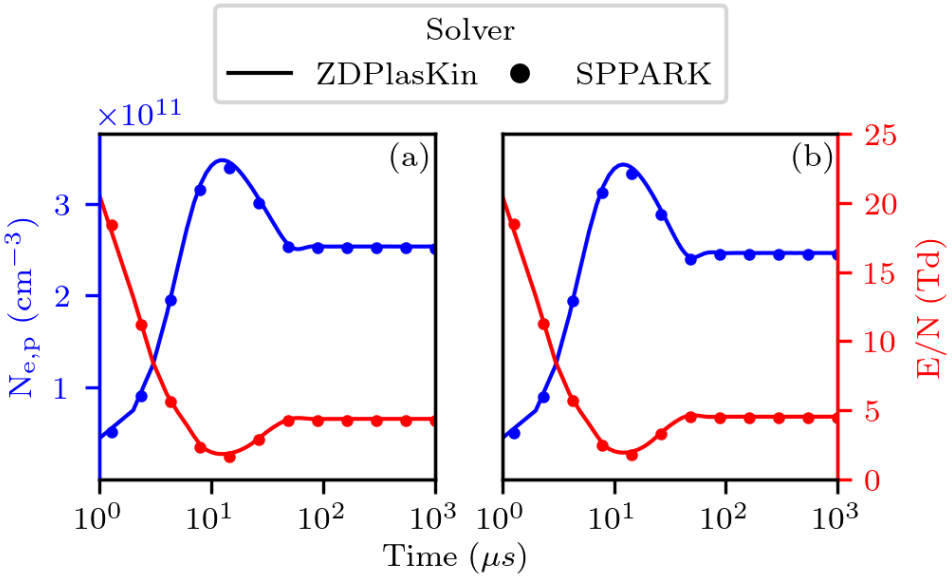

Figure 3.5.8 Electron number density (blue) and reduced electric field (red) results comparison between ZDPlasKin (continuous line) and SPPARK (dots) simulations for a pure Ar plasma at a constant temperature of 300 K and 100 torr of pressure, neglecting (a) and including (b) ambipolar losses in the chemistry set

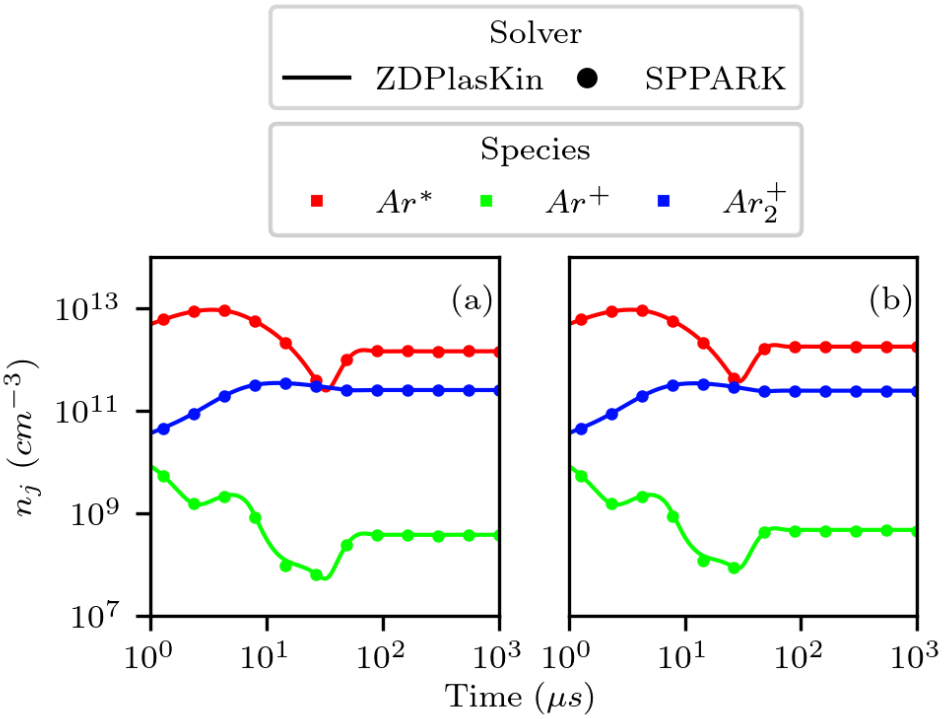

Figure 3.5.9 Heavy particles number densities results comparison between ZDPlasKin (continuous line) and SPPARK (dots) simulations for a pure Ar plasma at a constant temperature of 300 K and 100 torr of pressure, neglecting (a) and including (b) ambipolar losses in the chemistry set.

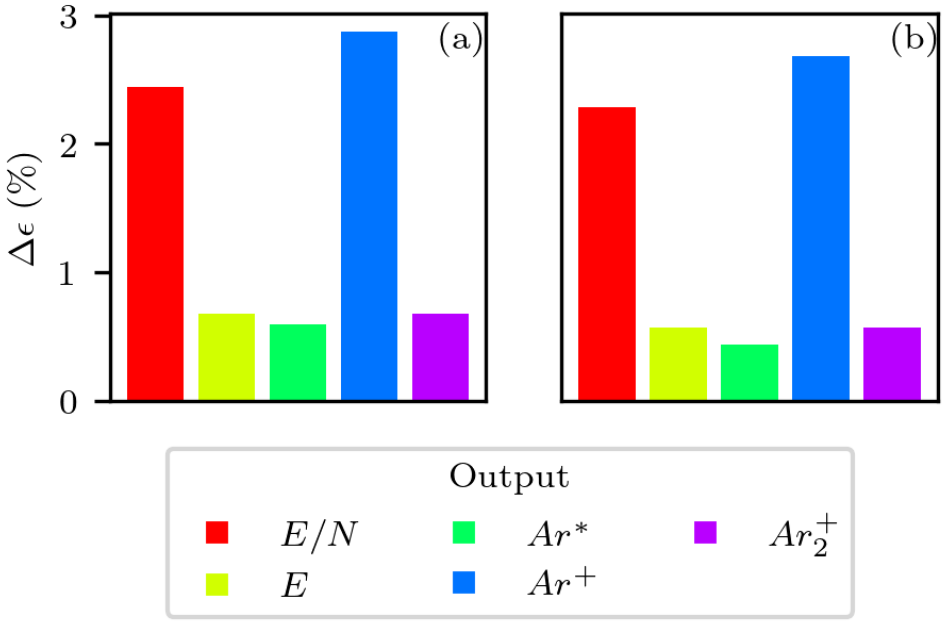

Figure 3.5.10 Maximum relative error (in percent) between the SPPARK and ZDPlasKin computations at a constant temperature of 300 K and 100 torr of pressure, neglecting (a) and including (b) ambipolar losses in the chemistry set.

3.5.3 CH_4 discharge

In this example, a homogeneous PSR with free-to-variate temperature is used to simulate the dissociation of methane in a plasma discharge. A power density of 75 W/mm^3 having the same shape of the signal in Figure 3.5.1 is used as electron solicitation in a pure methane mixture at 298.15 K and 1 bar. The adopted chemistry set is composed of 5 species (e^-, CH_4, CH_3, H and CH_4^+) reacting through the reactions described in Table 3.5.1. Being the chemistry set so approximate, the simulation purpose is not to present accurate results on methane dissociation in a plasma discharge, but rather to highlight the need of a proper species thermodynamic description for temperature-evolving systems.

In both the SPPARK and ZDPlasKin models, the species thermodynamic data has been obtained from NASA7 polynomials as provided by the GRI-Mech 3.0 mechanism [59]. Being based on Cantera, SPPARK can directly accept the polynomials coefficients in its configuration file. The ZDPlasKin model has been featured with user-defined functions to use the NASA7 polynomials data to compute the ratio of specific heats of the evolving gas mixture.

Id	**Equation**	**Rate constant**
1	$e^- + CH_4 \Rightarrow 2e^- + CH_4^+$	$f(\sigma)$ [60]
2	$e^- + CH_4 \Rightarrow e^- + CH_3 + H$	$f(\sigma)$ [61]
3	$e^- + CH_4^+ \Rightarrow CH_3 + H$	$f(\sigma)$ [62]
4	$CH_3 + H \Rightarrow CH_4$	$k_{Troe}(T_g)$ [59]

Table 3.5.1 Chemical reactions included in the methane chemistry set. The rate constants are expressed in cm3/s with $f(\sigma)$ being obtained through the Bolsig+ EEDF computation and T_g being the gas temperature expressed in K

In Table 3.5.1, k_{Troe} is defined as in equation 3.16:

$$\begin{cases} k_\infty = 2.31 \cdot 10^{-8} T_g^{-0.534} \exp\left(-\frac{269.75}{T_g}\right) \\ k_0 = 1.44 \cdot 10^{-14} T_g^{-4.74} \exp\left(-\frac{1227.98}{T_g}\right) \\ F_c = (1-A)\exp\left(-\frac{T_g}{T_3}\right) + A\exp\left(-\frac{T_g}{T_1}\right) + \exp\left(-\frac{T_2}{T_g}\right) \\ C = -0.4 - 0.67\log_{10} F_c \\ N = 0.75 - 1.27\log_{10} F_c \\ P_r = \frac{k_o[M]}{k_\infty} \\ f_1 = \frac{\log_{10} P_r + C}{N - 0.14(\log_{10} P_r + C)} \\ F(T_g, P_r) = 10^{\frac{\log_{10} F_c}{1+f_1^2}} \\ k_{Troe} = k_\infty \left(\frac{P_r}{1+P_r}\right) F(T_g, P_r) \end{cases} \quad (3.16)$$

where $A = 0.783$, $T_1 = 2941\,K$, $T_2 = 6964\,K$, $T_3 = 74\,K$, $[M]$ is the sum of number densities of any neutral species such that $k_0[M]$ and k_∞ are respectively the low-pressure and the high-pressure limits of the rate constant $\left(\frac{cm^3}{s}\right)$.

To ensure the equivalence of the two solvers implementation of gas heating due to electron-neutral elastic collisions, a first simulation neglecting reaction enthalpies has been performed. The agreement between the two approaches begins to diminish as the energy contribution of reaction 4 of table (1) is considered in the model. In fact, to the best of Authors' knowledge, the enthalpy of reaction must be provided as a constant value to the ZDPlasKin chemistry set input file, whilst it should be changing across the gas temperature spectrum accordingly with the enthalpy of formation of the species it features. This represents an approximation when dealing with large gas temperature ranges in the simulation. To better clarify this concept the values of internal energy of reaction for each CH_3 and H recombination to CH_4 occurring is presented in Figure 3.5.11. In Figure 3.5.12 the two simulations relative differences in the gas temperature computation are presented together with the gas temperature change in time due to reaction 4. From Figure 3.5.12 it is noticeable how the ZDPlasKin and SPPARK discrepancy is related to the introduction of the heat released by reaction 4. It is worth noticing that the discrepancy would increase with a larger number of temperature influencing reactions. For the 2 comparisons the average computation time for SPPARK is registered to be of 4 minutes and 2.1 seconds whilst the ZDPlasKin execution took 8 minutes and 22.80 seconds.

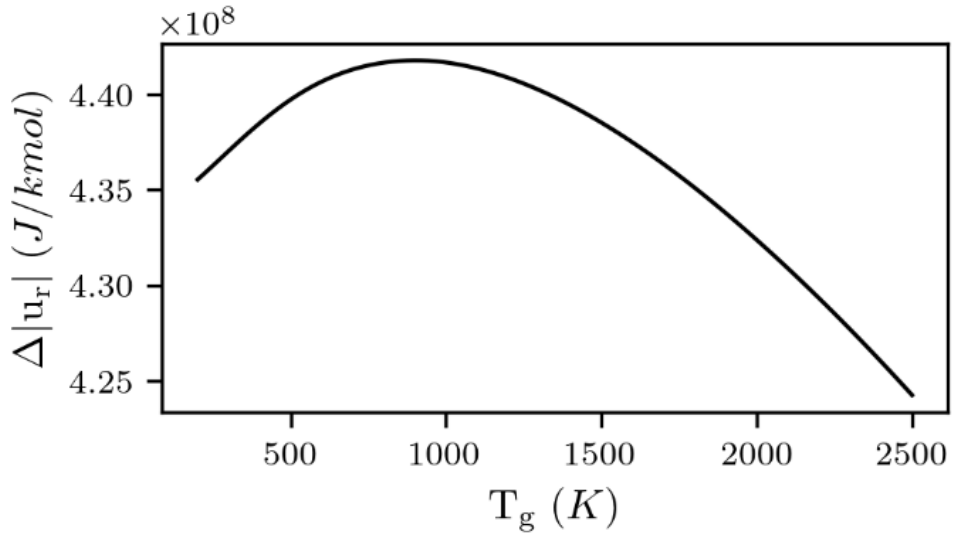

Figure 3.5.11 Internal energy of reaction for CH_3 and H recombination to CH_4.

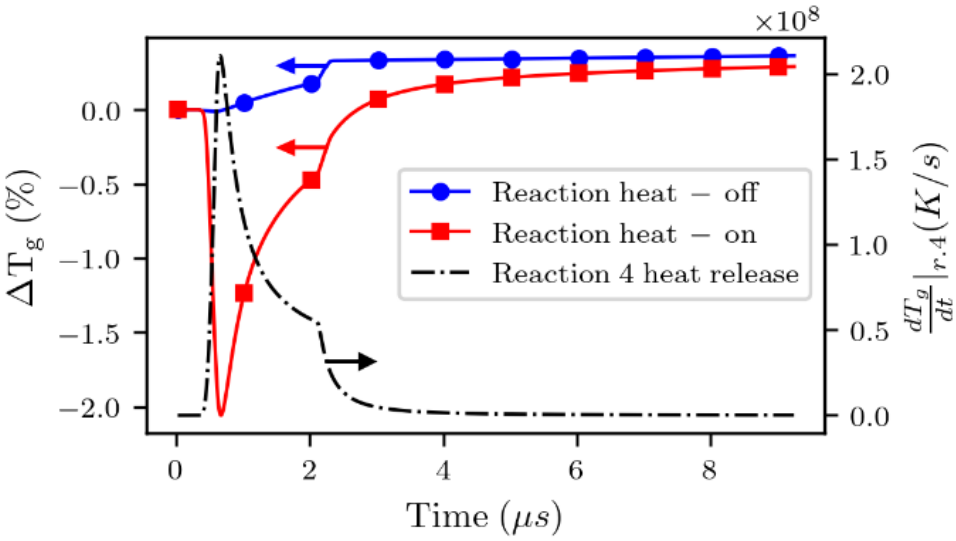

Figure 3.5.12 Comparison of the gas temperature time-evolution in the two simulations having the internal energy of reaction 4 excluded (blue) and included (red) in the simulation together with the heat release of reaction 4 (black).

3.6 Conclusions

Due to their potential to enhance the environmental sustainability of chemical process, non-equilibrium plasmas are gaining increasing interest in this technological field. Being characterized by multi-physical complex mechanisms, the study of plasma-chemistry processes often requires the application of numerical models to gain detailed insights into their founding principles. In this context, zero-dimensional plasma-chemistry solvers allow to focus on detailed

chemistries limiting the simulations computational time. To ensure full customisation and flexibility of application of a plasma-chemistry solver, it should be able to accurately consider both the electronic and thermochemical effects. SPPARK (Simulation Platform for Plasma Assisted Reactive Kinetics), a novel plasma chemistry solver based on Cantera and Bolsig+, has been developed. The solver makes use of the formalism and robustness of Cantera's models in thermo-chemical simulations together with the completeness of the description of the electronic kinetics of the Bolsig+ model, coupling them through many state-of-the-art models for the numerical representation of plasma effects in a plasma-gaseous system allowing users to represent many different plasma-chemical processes. The validity of the code has also been proven by comparison of its simulations results against the simulations obtained through the state-of-the-art solver ZDPlasKin on two different chemistry-sets on multiple validation cases. In addition, a test case on a simple methane splitting chemistry has been presented to extend the comparison of the two solvers to models characterized by time-evolving gas temperatures. Due to the different approaches in species and reactions thermodynamics representations, the results show relevant differences in the gas temperature results which could rapidly build up when implementing more complex reaction schemes. In conclusion, SPPARK's performance requires a brief discussion. Profiling the code revealed that the overall longer execution time of SPPARK compared to ZDPlasKin primarily derives from a non-optimized call of Bolsig+, which involves the writing of a configuration file, an external call to the Bolsig+ executable, and the reading of a result file at runtime. The input/output overhead is currently mitigated by triggering Bolsig+ execution only at the time steps where significant changes occur in the gas thermodynamic state, electron density or reduced electric field relative to a previous call. A complete resolution of this inefficiency could be achieved by the adoption in SPPARK of a dedicated Boltzmann solver that fully replicates the Bolsig+ model.

3.7 References

[1] De Bie C, Verheyde B, Martens T, van Dijk J, Paulussen S and Bogaerts A 2011 Fluid Modeling of the Conversion of Methane into Higher Hydrocarbons in an Atmospheric Pressure Dielectric Barrier Discharge Plasma Processes and Polymers **8** 1033–58

[2] Wnukowski M 2023 Methane Pyrolysis with the Use of Plasma: Review of Plasma Reactors and Process Products Energies **16** 6441

[3] Yuan X, Sun J, Ma Y, Wang Y, Liu B, Cai Y, Yong X and Tu X 2024 A kinetic study of nonthermal plasma pyrolysis of methane: Insights into hydrogen and carbon material production Chemical Engineering Journal **499** 156396

[4] Li T, Rehmet C, Cheng Y, Jin Y and Cheng Y 2017 Experimental Comparison of Methane Pyrolysis in Thermal Plasma Plasma Chemistry and Plasma Processing **37** 1033–49

[5] An H, Cheng Y, Li T, Li Y and Cheng Y 2018 Numerical analysis of methane pyrolysis in thermal plasma for selective synthesis of acetylene Fuel Processing Technology **172** 195–9

[6] Daghagheleh O, Schenk J, Zarl M A, Lehner M, Farkas M and Zheng H 2023 Feasibility of a Plasma Furnace for Methane Pyrolysis: Hydrogen and Carbon Production Energies **17** 167

[7] Daghagheleh O, Schenk J, Zheng H, Zarl M A, Farkas M, Ernst D, Kieush L, Lehner M, Kostoglou N and Obenaus-emler R 2024 Optimizing methane plasma pyrolysis for instant hydrogen and high-quality carbon production International Journal of Hydrogen Energy **79** 1406–17

[8] Hazenberg T, van Dijk J and Oijen J A van 2023 Chemical flux analysis of low-temperature plasma-enhanced oxidation of methane and hydrogen in argon Combustion and Flame **257** 113037

[9] Burger C M, Zhang A J, Xu Y, Hansen N and Ju Y 2023 Plasma-Assisted Chemical-Looping Combustion: Low-Temperature Methane and Ethylene Oxidation with Nickel Oxide The Journal of Physical Chemistry A **127** 789–98

[10] Sun J, Chen Q, Yang X and Koel B E 2019 Effects of non-equilibrium excitation on methane oxidation in a low-temperature RF discharge Journal of Physics D: Applied Physics **53** 064001

[11] Ma T, Sun K, Meng L, Cheng P, Cheng Q and Li S 2024 Oxidation of lean methane by dielectric barrier discharge plasma and Mn–Ce catalyst Chemical Engineering and Processing - Process Intensification **204** 109925

[12] Zhou M, Yang Z, Ren J, Zhang T, Xu W and Zhang J 2023 Non-oxidative coupling reaction of methane to hydrogen and ethene via plasma-catalysis process International Journal of Hydrogen Energy **48** 78–89

[13] Pourali N, Vasilev M, Abiev R and Rebrov E V 2022 Development of a microkinetic model for non-oxidative coupling of methane over a Cu catalyst in a non-thermal plasma reactor Journal of Physics D: Applied Physics **55** 395204

[14] Maslova V, Nastase R, Veryasov G, Nesterenko N, Fourré E and Batiot-Dupeyrat C 2024 Current status and challenges of plasma and plasma-catalysis for methane coupling: A review Progress in Energy and Combustion Science **101** 101096

[15] Maitre P-A, Long J, Bieniek M S, Bannerman M N and Kechagiopoulos P N 2022 Investigating the effects of helium, argon and hydrogen co-feeding on the non-oxidative coupling of methane in a dielectric barrier discharge reactor Chemical Engineering Science **259** 117731

[16] Wnukowski M, Steeg A W van de, Hrycak B, Jasiński M and Rooij G J van 2021 Influence of hydrogen addition on methane coupling in a moderate pressure microwave plasma Fuel **288** 119674

[17] Liu R, Hao Y, Wang T, Wang L, Bogaerts A, Guo H and Yi Y 2023 Hybrid plasma-thermal system for methane conversion to ethylene and hydrogen Chemical Engineering Journal **463** 142442

[18] Klimek A and Piercey D G 2024 Nitrogen Fixation via Plasma-Assisted Processes: Mechanisms, Applications, and Comparative Analysis—A Comprehensive Review Processes **12** 786

[19] Chen H, Yuan D, Wu A, Lin X and Li X 2021 Review of low-temperature plasma nitrogen fixation technology Waste Disposal & Sustainable Energy **3** 201–17

[20] Manaigo F, Bogaerts A and Snyders R 2024 Study of a gliding arc discharge for sustainable nitrogen fixation into NOx 2024 IEEE International Conference on Plasma Science (ICOPS) (IEEE) pp 1–1

[21] Aceto D, Ambrico P F and Esposito F 2024 Air cold plasmas as a new tool for nitrogen fixation in agriculture: underlying mechanisms and current experimental insights Frontiers in Physics **12**

[22] Lamichhane P, Pourali N, Rebrov E V and Hessel V 2024 Energy Intensified Nitrogen Fixation Through Fast Modulated Gas Discharge from Pyramid-shaped Micro-electrode Plasma Chemistry and Plasma Processing **44** 1369–92

[23] Gao H, Wang G, Huang Z, Nie L, Liu D, Lu X, He G and Ostrikov K K 2023 Plasma-Activated Mist: Continuous-Flow, Scalable Nitrogen Fixation, and Aeroponics ACS Sustainable Chemistry & Engineering **11** 4420–9

[24] Zhao X and Tian Y 2023 Sustainable nitrogen fixation by plasma-liquid interactions Cell Reports Physical Science **4** 101618

[25] Muzammil I, Lee D H, Dinh D K, Kang H, Roh S A, Kim Y-N, Choi S, Jung C and Song Y-H 2021 A novel energy efficient path for nitrogen fixation using a non-thermal arc RSC Advances **11** 12729–38

[26] Centi G, Perathoner S and Papanikolaou G 2021 Plasma assisted CO2 splitting to carbon and oxygen: A concept review analysis Journal of CO2 Utilization **54** 101775

[27] Burghaus H, Kaiser C F, Fasoulas S and Herdrich G 2023 Influence of specific energy inhomogeneity on the CO2 splitting performance in a high-power plasma jet Vacuum **217** 112500

[28] Scurtu A, Ticoş D, Mitu M L, Diplaşu C, Udrea N and Ticoş C M 2023 Splitting CO2 in Intense Pulsed Plasma Jets International Journal of Molecular Sciences **24** 6899

[29] Liu Z, Zhou W, Xie Y, Liu F, Fang Z, Zhang G and Jin W 2023 Highly effective CO2 splitting in a plasma-assisted membrane reactor Journal of Membrane Science **685** 121981

[30] Renninger S, Lambarth M and Birke K P 2020 High efficiency CO2-splitting in atmospheric pressure glow discharge Journal of CO2 Utilization **42** 101322

[31] Meng G, Xia L, Cheng Y and Yin Z 2023 AC-driven atmospheric pressure glow discharge co-improves conversion and energy efficiency of CO2 splitting Journal of CO2 Utilization **70** 102447

[32] Mahdikia H, Brüser V, Schiorlin M and Brandenburg R 2023 CO2 Dissociation in Barrier Corona Discharges: Effect of Elevated Pressures in CO2/Ar Mixtures Plasma Chemistry and Plasma Processing **43** 2035–63

[33] Renninger S, Stein J, Lambarth M and Birke K P 2022 An optimized reactor for CO2 splitting in DC atmospheric pressure discharge Journal of CO2 Utilization **58** 101919

[34] Faingold G, Kabour R, Shen S and Lefkowitz J K 2024 Reforming of ammonia and ammonia-air mixtures in a homogenous plasma reactor: Parametric study of hydrogen yields International Journal of Hydrogen Energy **73** 856–67

[35] Zhang X and Cha M S 2024 Ammonia cracking for hydrogen production using a microwave argon plasma jet Journal of Physics D: Applied Physics **57** 065203

[36] Bang S, Snoeckx R and Cha M S 2023 Kinetic Study for Plasma Assisted Cracking of NH_3: Approaches and Challenges The Journal of Physical Chemistry A **127** 1271–82

[37] Zhang X and Cha M S 2024 Optimizing ammonia cracking in microwave argon plasma: Temperature control and ammonia delivery Chemical Engineering Journal **496** 154289

[38] Zhang X, Shan Y, Sun Z, Pan H, Zhang L, Zhu Z, Feng F, Han J and Li K 2024 Mechanism of plasma chemistry in CO_2 hydrogenation using a dielectric barrier discharge reactor Plasma Processes and Polymers **21**

[39] Ullah N, Su M, Yang Y and Li Z 2023 Enhanced CO2 hydrogenation to light hydrocarbons on Ni-based catalyst by DBD plasma International Journal of Hydrogen Energy **48** 21735–51

[40] Li K, Teng P, Fei R, Lu Z, Zhang L and Zhang X 2025 Reaction mechanism of plasma chemistry in CO2 hydrogenation: The effect of CO2/H2 ratio Journal of Electrostatics **134** 104017

[41] Wang L, Yi Y, Guo H and Tu X 2018 Atmospheric Pressure and Room Temperature Synthesis of Methanol through Plasma-Catalytic Hydrogenation of CO_2 ACS Catalysis **8** 90–100

[42] Chen Y, Peng Y, Qian M, Liu S, Zhang J and Wang D 2022 A zero-dimensional model for atmospheric non-thermal plasma CO_2 hydrogenation: insights into the reaction mechanism Japanese Journal of Applied Physics **61** 086001

[43] Liu M, Yi Y, Wang L, Guo H and Bogaerts A 2019 Hydrogenation of Carbon Dioxide to Value-Added Chemicals by Heterogeneous Catalysis and Plasma Catalysis Catalysts **9** 275

[44] Fridman A 2008 Plasma Chemistry Plasma Chemistry **9780521847353** 1–978

[45] Popov N A 2011 Fast gas heating in a nitrogen–oxygen discharge plasma: I. Kinetic mechanism Journal of Physics D: Applied Physics **44** 285201

[46] Mintoussov E I, Pendleton S J, Gerbault F G, Popov N A and Starikovskaia S M 2011 Fast gas heating in nitrogen–oxygen discharge plasma: II. Energy exchange in the afterglow of a volume nanosecond discharge at moderate pressures Journal of Physics D: Applied Physics **44** 285202

[47] Hagelaar G J M and Pitchford L C 2005 Solving the Boltzmann equation to obtain electron transport coefficients and rate coefficients for fluid models Plasma Sources Science and Technology **14** 722–33

[48] Pancheshnyi S, Eismann B, Hagelaar G and Pitchford L 2008 ZDPlasKin

[49] van Dijk J Peerenboom K, Jimenez M, Mihailova D and Mullen J van der 2009 The plasma modelling toolkit Plasimo Journal of Physics D: Applied Physics **42** 194012

[50] Cheng L, Barleon N, Cuenot B, Vermorel O and Bourdon A 2022 Plasma assisted combustion of methane-air mixtures: Validation and reduction Combustion and Flame **240** 111990

[51] Shao X, Lacoste D A and Im H G 2024 ChemPlasKin: A general-purpose program for unified gas and plasma kinetics simulations Applications in Energy and Combustion Science **19** 100280

[52] K S 2022 CRANE https://github.com/lcpp-org/crane

[53] Goodwin D G, Moffat H K, Schoegl I, Speth R L and Weber B W 2024 Cantera: An Object-oriented Software Toolkit for Chemical Kinetics, Thermodynamics, and Transport Processes

[54] Lieberman M A and Lichtenberg A J 2005 Principles of Plasma Discharges and Materials Processing: Second Edition Principles of Plasma Discharges and Materials Processing: Second Edition 1–757

[55] Heijkers S, Aghaei M and Bogaerts A 2020 Plasma-Based CH_4 Conversion into Higher Hydrocarbons and H_2: Modeling to Reveal the Reaction Mechanisms of Different Plasma Sources The Journal of Physical Chemistry C **124** 7016–30

[56] Morais E, Delikonstantis E, Scapinello M, Smith G, Stefanidis G D and Bogaerts A 2023 Methane coupling in nanosecond pulsed plasmas: Correlation between temperature and pressure and effects on product selectivity Chemical Engineering Journal **462** 142227

[57] Grubert G K, Becker M M and Loffhagen D 2009 Why the local-mean-energy approximation should be used in hydrodynamic plasma descriptions instead of the local-field approximation Physical Review E **80** 036405

[58] Alves L L and Tejero-del-Caz A 2023 Charged-particle transport models for global models Plasma Sources Science and Technology **32** 054003

[59] Gregory P. Smith, David M. Golden, Michael Frenklach, Nigel W. Moriarty, Boris Eiteneer, Mikhail Goldenberg, C. Thomas Bowman, Ronald K. Hanson, Soonho Song, William C. Gardiner, Jr., Vitali V. Lissianski, and Zhiwei Qin http://www.me.berkeley.edu/gri_mech/

[60] Lindsay B and Mangan M 2003 Interactions of Photons and Electrons with Molecules vol 17C (Springer)

[61] Bouwman D, Martinez A, Braams B J and Ebert U 2021 Neutral dissociation of methane by electron impact and a complete and consistent cross section set Plasma Sources Science and Technology **30** 075012

[62] Braams B J and Chung H-K 2014 Atomic and Plasma-Material Interaction Data for Fusion. V. 16 (IAEA)

Chapter 4

Multizone global modeling of plasmas

This chapter is based on the article: A. Marchetti, et al., "A Multizone Global Model for the Analysis of Ozone Transport in Surface DBD Systems", Plasma Medicine, Vol. 15, Issue 2, pp. 49-61, 2025, © Begell House. Reproduced with permission from the publisher under the copyright agreement.

4.1 Preface

This chapter presents in greater detail an application case study of the multizone global modeling technique applied to plasma chemistry. Specifically, it reports the modeling-experimental analysis published in A. Marchetti, et al., "A Multizone Global Model for the Analysis of Ozone Transport in Surface DBD Systems", *Plasma Medicine*, Vol. 15, Issue 2, pp. 49–61, 2025. The objective is to numerically represent ozone production in large-area surface dielectric barrier discharges, investigating the extent of transport phenomena from the plasma generation zone to the gas-phase measurement zone, while keeping the bulk chemical kinetics of the two regions separate. From the comparison with experimental measurements, it is concluded that - given the considered chemistry - purely diffusive transport is not sufficient to accurately predict ozone migration from the plasma zone to the gas zone, thus requiring a forced convection mechanism whose magnitude is estimated.

In the context of the thesis, this chapter highlights the extended modeling capabilities that SPPARK enables through the multizone approach, while still relying on a comprehensive reaction set. This approach can improve, at a relatively low computational cost, the pseudo-spatial accuracy of a simulation by including approximations of species migration phenomena that would otherwise be entirely neglected in a single-zone framework. The results thus obtained can also be employed to ensure a greater precision in the chemical complexity reduction algorithm introduced in Chapter 5.

4.2 Abbreviations

CAP: Cold Atmospheric pressure Plasma

DBD: Dielectric Barrier Discharge

SDBD: Surface Dielectric Barrier Discharge

RONS: Reactive Oxygen and Nitrogen Species

SCFM: Self Consistent Fluid Model

GM: Global Model

MGM: Multizone Global Model

LA-SDBD: Large Area - Surface Dielectric Barrier Discharge

ODE: Ordinary Differential Equation

LFA: Local Field Approximation

OAS: Optical Absorption Spectroscopy

4.3 Introduction

Cold atmospheric pressure plasma (CAP) sources have emerged as versatile tools in biomedical applications, ranging from surface sterilisation to wound healing and airborne pathogen inactivation [1–3]. Among these, Dielectric Barrier Discharge (DBD) and Surface Dielectric Barrier Discharge (SDBD) plasma sources represent some of the most promising technologies for large areas objects treatment [4–6], albeit with some differences. In fact, DBD plasma sources are composed of two electrodes, between which a dielectric barrier and a gas gap, with a width ranging from 0.1 to several centimetres, are interposed, having the whole gas volume in the gap acting as a treatment chamber. This characteristic, although granting a superposition of possibly positive agents (*i.e.* long and short living reactive species, UV radiation, electric fields) [7–12] to concur in sustaining the inactivation process, limits the applicability of DBD sources to relatively small objects (*i.e.* the gap width and the object thickness must be compatible) at atmospheric pressure. In the case of SDBDs, the constitutive scheme differs from the DBD sources as the inter-electrode gap is not present. In fact, the ground electrode is usually composed of a metallic mesh, allowing the plasma generation to occur directly on the dielectric surface through the holes of such electrode. Thus, the plasma generation and treatment regions are separated. Typically, a treatment chamber is attached to the SDBD source, allowing for reactive species, such as long-living reactive oxygen and nitrogen species (RONS), to be conveyed to the objects to be treated.

In this context, ozone (O_3) is one of the most relevant reactive chemical compounds produced by CAPs ignited in humid air [13]. The typical lifetimes in air (tens of seconds to minutes) of such molecule allows it to efficiently exert its antimicrobial effects on the treatment sample surfaces. In a humid air plasma, the ozone production is mostly achieved by first splitting an oxygen molecule via electron collisions, obtaining atomic oxygen, that, reacting with another oxygen molecule and a third body, recombines into O_3 ($O + O_2 + M \Leftrightarrow O_3 + M$). In a SDBD, most of the ozone is produced in the plasma phase, where free electrons are sufficiently dense and energetic to split the oxygen molecules and initiate the reaction chain to produce the ozone molecule. The O_3 in the plasma phase is then conveyed to the treatment chamber through diffusive and advective transport mechanisms.

Nonetheless, CAP treatments involve a complex interplay of fundamental phenomena, making it challenging to control and optimize the overall process. In this context, numerical plasma modeling serves as a powerful tool for gaining a deeper understanding of the underlying mechanisms. It helps clarify the relationship between the desired outcomes and the operating parameters, thereby enabling the fine-tuning of these parameters to enhance process efficiency. To

represent the ozone formation and transport from the plasma region, multidimensional self-consistent fluid models (SCFM) [14] could be a valuable solution as they include the continuity, momentum, and energy balances coupled with the time-dependent solution for the electric field in the discharge domain. Unfortunately, SCFMs are usually computationally demanding, especially when including large plasma-chemistry sets as the humid air one [15]. To focus on the pure chemical accuracy, dealing with reaction schemes composed of hundreds of species and reactions, plasma global models (GMs) are often preferred [14]. In fact, GMs are built to track the time evolution of chemical species concentrations and temperatures in a homogeneous (*i.e.* spatially averaged) domain, allowing the computational costs to be kept low when dealing with large chemistry sets. Nonetheless, the hypothesis of complete homogeneity of the spatial domain could be excessively approximative to model an SDBD plasma source, as the plasma generation region and the treatment chamber are usually well distinct and could have volumes differing by orders of magnitude. For this reason, the adoption of a Multizone Global Model (MGM), capable of representing the plasma and the gas (acting as the treatment chamber) phases as separate while approximating the species transport between the two, is preferable. Sakiyama *et al.* [15] used an example of MGM to simulate a SDBD humid air plasma. In that work, the species transport between the two phases was modelled as purely diffusive, and the model was qualitatively validated against *in situ* Fourier transform infrared absorption spectroscopy measurements. Nonetheless, it is known that in SDBD sources, forced transport mechanisms, like ionic winds or heat-driven advection, are also involved in the species migration [16–18].

In this work, we explore the adoption of an MGM to simulate a Large Area SDBD (LA-SDBD). The MGM was implemented in the SPPARK plasma chemistry solver [19] to study the influence of different species transport models on the gas-phase ozone concentration predicted by the simulations. In particular, the focus of this study is to determine whether the experimentally observed O_3 dynamics in a closed chamber can be reproduced by considering a diffusive migration alone, or if additional transfer mechanisms, such as forced advection, should be introduced in the model.

4.4 Model description

The MGM involves the solution of two separate ordinary differential equations (ODE) systems representing the species moles time evolution (*i.e.* continuity equations) under the ideal gas hypothesis in a plasma and a gas phase (Figure 4.4.1).

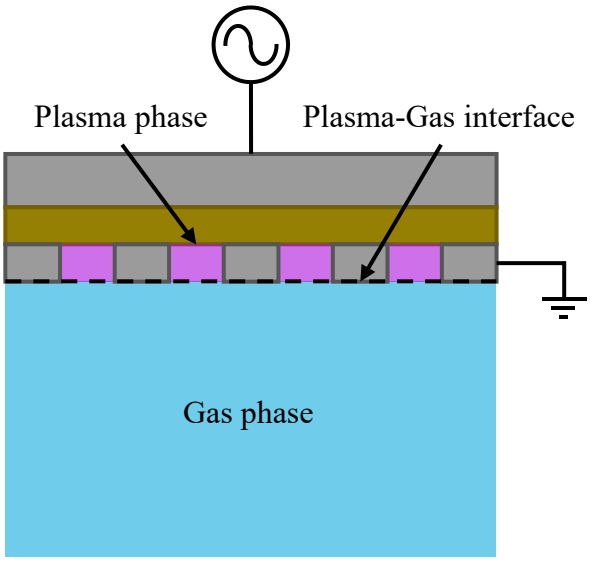

Figure 4.4.1 Multizone Global Model schematics. The LA-SDBD is modelled through two separate phases: a plasma phase and a gas phase. The two volumes are connected with a fictitious plasma-gas interface where the species exchange between the two phases is modelled.

The two ODE systems are coupled employing shared terms in the continuity equations representing the species transport between the plasma and the gas phase. For reference, the i-th species continuity equation is shown in equations 4.1 – 4.4.

$$\frac{dn_i^{(\varphi)}}{dt} = V^{(\varphi)} \cdot \omega_i^{(\varphi)} + \mathrm{T}_i^{(\varphi)} + \dot{n}_i(\Delta p) \tag{4.1}$$

$$\omega_i^{(\varphi)} = \sum_{j=1}^{N_R} \left(\nu_{i,j}^{p} - \nu_{i,j}^{r}\right) \left[r_{j,f}^{(\varphi)} - r_{j,r}^{(\varphi)}\right] \tag{4.2}$$

$$r_{j,f}^{(\varphi)} = k_{j,f}^{(\varphi)} \prod_{q=1}^{N_S} \left(c_q^{(\varphi)}\right)^{\nu_{q,j}^{r}} \tag{4.3}$$

$$r_{j,r}^{(\varphi)} = k_{j,r}^{(\varphi)} \prod_{q=1}^{N_S} \left(c_q^{(\varphi)}\right)^{\nu_{q,j}^{p}} \tag{4.4}$$

where t is the time (s), φ is the phase index (*i.e.* p for the plasma phase and g for the gas phase), $n_i^{(\varphi)}$ is the i-th species number of moles ($kmol$) in the φ phase, $V^{(\varphi)}$ is the φ phase zone volume (m^3), $\omega_i^{(\varphi)}$ is the volumetric net production rate of the i-th species $\left(\frac{kmol}{m^3 s}\right)$, $\mathrm{T}_i^{(\varphi)}$ is the i-th species net transport term towards phase φ $\left(\frac{kmol}{s}\right)$, $\nu_{i,j}^{p}$ and $\nu_{i,j}^{r}$ are respectively the product and reactant stoichiometric

coefficients of the i-th species in the j-th reaction, $r_{j,f}^{(\varphi)}$ and $r_{j,r}^{(\varphi)}$ are the j-th forward and reverse reaction rates evaluated in the φ phase $\left(\frac{kmol}{m^3 s}\right)$, $k_{j,f}^{(\varphi)}$ is the forward rate constant of the j-th reaction in the φ phase $\left(\frac{m^{3\left(\sum_{q=1}^{N_s} \nu_{q,j}^{r} - 1\right)}}{s \cdot kmol^{\left(\sum_{q=1}^{N_s} \nu_{q,j}^{r} - 1\right)}}\right)$, $k_{j,r}^{(\varphi)}$ is the reverse rate constant of the j-th reaction in the φ phase $\left(\frac{m^{3\left(\sum_{q=1}^{N_s} \nu_{q,j}^{p} - 1\right)}}{s \cdot kmol^{\left(\sum_{q=1}^{N_s} \nu_{q,j}^{p} - 1\right)}}\right)$, $c_q^{(\varphi)}$ is the q-th species concentration in the φ phase $\left(\frac{kmol}{m^3}\right)$, N_R is the total number of reactions, and N_s is the total number of species. $\dot{n}_i(\Delta p)$ is an additional term, proportional to the difference in pressure between the two phases (Δp), representing the transport of species to equilibrate such pressure mismatch $\left(\frac{kmol}{s}\right)$. The latter term is included, in the continuity equations, by connecting the two phases with a *Valve* object in the network of reactors in SPPARK's Cantera [20] backend. The species and reactions involved in the model are defined by means of a chemistry-set and thus continuity equations (equation 4.1) are solved for each species thereby included for both phases but, in the case of the gas phase, the charged species are not considered in the system of equations.

The species transport term (T_i) is implemented to represent the superposition of a diffusive effect moving particles between the two phases and a phenomenological forced effect advecting species from the plasma to the gas phase. By including a fictitious boundary surface between the two phases, this term can be considered in the model through a surface reaction, as reported in Marchetti *et al.* [19], for each species and phase. A generic fictious surface reaction of this type has an equation defined as described in equation 4.5.

$$I^{(\varphi_1)} + \mathrm{Void}(S) \underset{\sigma_i^{(\varphi_2)}}{\overset{\sigma_i^{(\varphi_1)}}{\Longleftrightarrow}} I^{(\varphi_2)} + \mathrm{Void}(S) \tag{4.5}$$

where $I^{(\varphi_j)}$ is the i-th species belonging to the φ_j phase, $\mathrm{Void}(S)$ is a "void" active-site of the fictitious surface between the two phases, and $\sigma_i^{(\varphi_j)}$ is the surface reaction rate constant defined for the generic φ_j phase $\left(\frac{m^3}{s \cdot kmol}\right)$. Making use of such reactions, the T_i term can be expressed as follows:

$$\mathrm{T}_i^{(\varphi_1)} = A \cdot \left(\sigma_i^{(\varphi_2)} c_i^{(\varphi_2)} S_d - \sigma_i^{(\varphi_1)} c_i^{(\varphi_1)} S_d\right) \tag{4.6}$$

where S_d is the surface active-site density $\left(\frac{kmol}{m^2}\right)$, and A is the surface area (m^2). For the plasma phase, the surface reaction rate constant $\sigma_i^{(p)}$ is defined as:

$$\sigma_i^{(p)} = \left[\frac{D_i}{\frac{1}{2}(d_p + d_g)} + v\right] \cdot \frac{1}{S_d} \tag{4.7}$$

where D_i is the diffusion coefficient of the i-th species $\left(\frac{m^2}{s}\right)$, $d_p = \frac{V^{(p)}}{A}$ is the plasma phase thickness (m), $d_g = \frac{V^{(g)}}{A}$ is the gas phase thickness (m), and v is the forced advection term velocity $\left(\frac{m}{s}\right)$. For the gas phase the surface reaction rate constant $\sigma_i^{(g)}$ is defined similarly, neglecting the forced term (v) as described in equation 4.8.

$$\sigma_i^{(g)} = \left[\frac{D_i}{\frac{1}{2}(d_p + d_g)}\right] \cdot \frac{1}{S_d} \tag{4.8}$$

Using the definition of the surface reaction rate constants in equation 4.7 and 4.8, the $\mathrm{T}_i^{(\varphi)}$ transport term defined in equation 4.6 becomes independent of the S_d active-site density.

The reaction set adopted in the model is the one described by Sakiyama *et al.* [15]. In this reaction set, some of the non-equilibrium induced reactions (*i.e.* electron collisions and charged species recombinations) are defined as a function of the electron temperature. In order to speed up calculation times, an approximation has been carried out in the model. Assuming the electron kinetics to be faster than the considered timescales, the reduced electric field solicitation, responsible for sustaining the temperature of the electrons, has been derived from a comparison of the mean power supplied to the plasma source against the power ceded to the gas particles by electron collisions calculated through Bolsig+ [21]. The value of reduced electric field granting the equilibrium between the supplied and ceded power is then used, in Bolsig+, to compute the electron temperature. Subsequently, a constant value of electron density has been obtained through the Local Field Approximation (LFA):

$$N_e = \frac{\tilde{P}}{\left(\frac{E}{N}10^{-21}\right)^2 \cdot N^2 \mu_e e} \tag{4.9}$$

where N_e is the electron number density (m^{-3}), $\frac{E}{N}$ is the reduced electric field (Td) obtained through the Bolsig+ power comparison, $\tilde{P}$ is the deposited power density $\left(\frac{W}{m^3}\right)$, $N = \frac{p}{k_b T_g}$ is the neutral number density (m^{-3}) with p the gas pressure (Pa),

k_b the Boltzmann constant $\left(\frac{J}{K}\right)$ and T_g the macroscopic gas temperature (K), μ_e is the electron mobility $\left(\frac{m^2}{Vs}\right)$ obtained in Bolsig+, and e is the elementary charge (C).

4.5 Simulation set-up

The gas initial conditions are set to represent a humid air mixture at a constant temperature of $300K$, a pressure of $1atm$ and relative humidity of 60%. From the experimental electrical characterization of the plasma, an average power per period of $27.363\ W$ is measured as described by Maccaferri *et al.* [22–24], which corresponds to a power density of $1.204\frac{W}{cm^3}$ considering a plasma phase volume of $22.72\ cm^3$. This power density value is used to estimate the steady-state reduced electric field value, which is found to be equal to $108\ Td$, corresponding to an average electron energy of $2.5\ eV$. From the LFA electron density computation (equation 4.9), the electron density is set to $2.761 \cdot 10^7\ cm^{-3}$.

The gas phase volume is set to $14.34\ L$, representing the whole box volume of the LA-SDBD [22–24]. The surface interposed between the plasma and the gas phase (equation 4.5) is defined with an area of $151.47\ cm^2$. For clarity, all the parameters relevant to the simulation are summarized in Table 4.5.1.

Parameter	**Value**
Gas temperature - T_g (K)	300
Gas pressure - p (atm)	1
Relative humidity (%)	60
Average power (W)	27.363
Average power density - $\tilde{P}\left(\frac{W}{cm^3}\right)$	1.204
Plasma volume – $V^{(p)}(cm^3)$	22.72
Gas volume – $V^{(g)}(cm^3)$	$14.34 \cdot 10^3$
Fictious interface area – A (cm^2)	151.47
Reduced electric field – $\frac{E}{N}$ (Td)	108
Mean electron energy (eV)	2.5
Electron density – N_e (cm^{-3})	$2.761 \cdot 10^7$

Table 4.5.1 List of the relevant parameters for the simulation setup.

For the forcing term in equation 4.7 (v), a parametric analysis is performed at first with a purely diffusive transport $\left(v = 0\frac{m}{s}\right)$ and subsequently ranging its values from $0.1\frac{m}{s}$ to $0.5\frac{m}{s}$. Quantitative experimental measurements of ozone concentrations are sampled at discrete spatial points throughout the treatment chamber, as described in Maccaferri *et al.* [22] (Figure 4.8.2). These measurements were then spatially averaged and used as a reference for the simulations in order to identify the transport rate that most closely aligns the model predictions with experimental data; both experimental measurements and simulations refer to a discharge time of 30 minutes. The results presented in the next section refer exclusively to the gas phase, as its reactive species concentrations are the ones

exerting the antimicrobial effect on the treatment sample, and thus are the most relevant for the process.

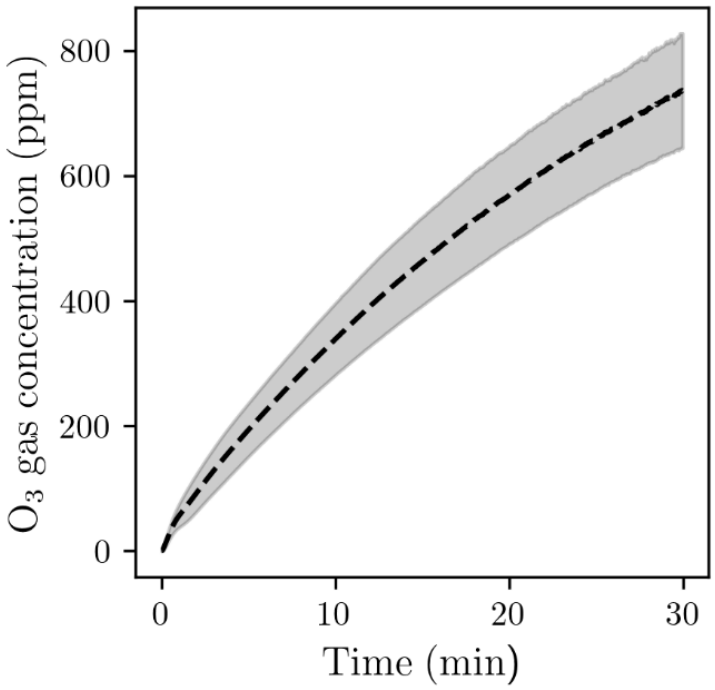

Figure 4.5.1 Time evolution of the ozone gas concentration experimentally measured in Maccaferri et al. [22]. In the graph, the dashed line represents the spatially averaged value across all measurements, and the shaded area represents the measurements' standard deviation

4.6 Results

In the case of pure diffusive transport $\left(v = 0\frac{m}{s}\right)$, the model is not able to replicate the experimental Optical Absorption Spectroscopy (OAS) measurements, reaching, after 30 min of discharge time, an ozone concentration in the gas phase of approximately $2.76\,ppm$ (Figure 4.6.1) in contrast with the final concentration of $\approx 736.28 \pm 91.82\,ppm$ measured in the experiments. This result suggests that, considering a purely diffusive plasma-to-gas reaction rate constant $\left(\sigma_i^{(p)}\right)$ in equation 4.6 is insufficient to reproduce the ozone transported in the gas phase, thereby highlighting the necessity of including the additional phenomenological forced transport term in equation 4.7.

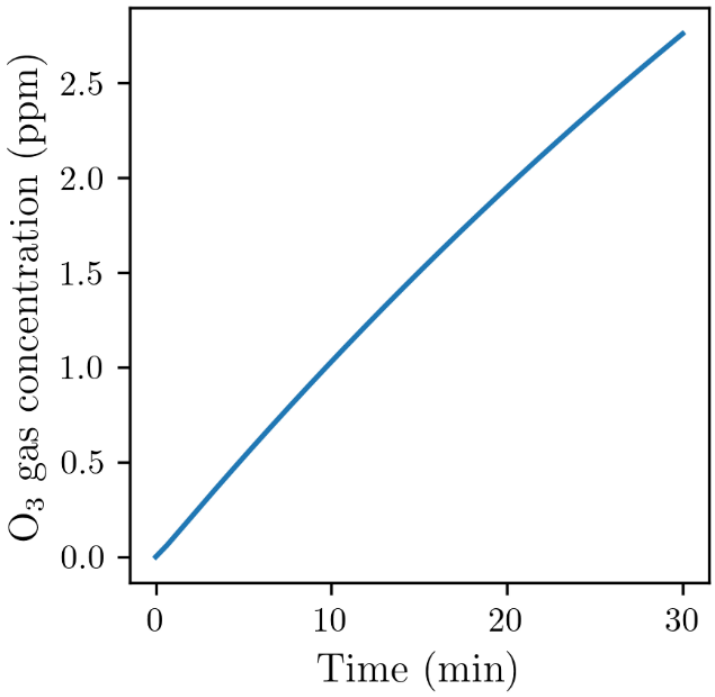

Figure 4.6.1 Simulation results for the time evolution of ozone in the gas phase with a purely diffusive migration from the plasma phase.

An array of 5 additional simulations is performed in order to identify the influence of forced transport on the O_3 concentration in the gas phase. The results produced by the simulations are summarized in Figure 4.6.2. To further characterize the effect of the forced transport term on the O_3 concentration, in Figure 4.6.3, the trend for the maximum (*i.e.* final) ozone concentration against the forced transport magnitude is presented. From the comparison of Figure 4.6.2 and Figure 4.6.3, it is possible to highlight a different dynamic behaviour in the 6 simulations. For simulations with $v \in [0.3, 0.4, 0.5]\frac{m}{s}$, in the last minutes of the simulation, the ozone source term in the gas region (*i.e.* the plasma to gas transport) decreases as the concentration of the molecule slowly approaches the steady-state. This is also reflected in Figure 4.6.3, where the slope of the maximum ozone concentration as a function of the forcing velocity decreases in the upper range of the velocity domain.

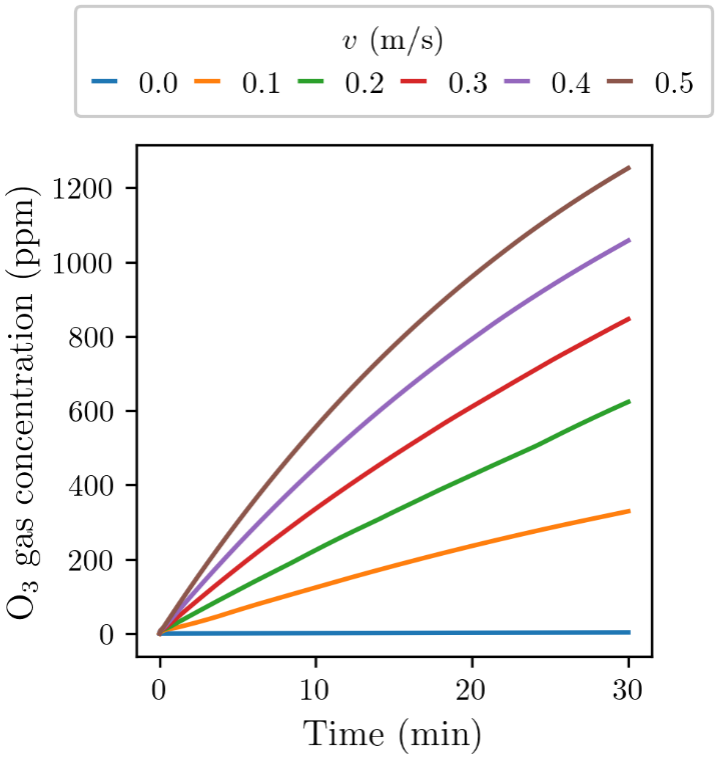

Figure 4.6.2 Simulation results for the time evolution of ozone in the gas phase varying the phenomenological forced transport magnitude.

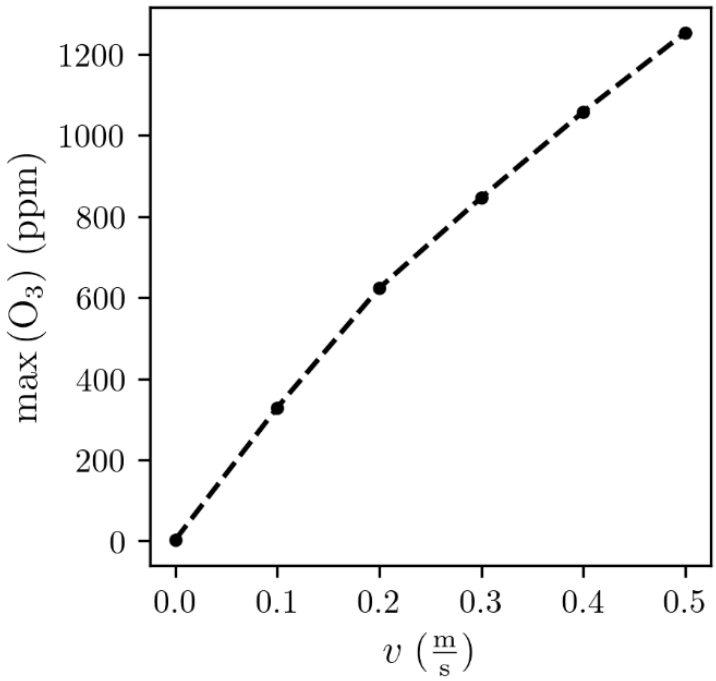

Figure 4.6.3 Trend of the maximum (final) ozone concentration against the forced transport velocity.

From the final ozone concentration trends in Figure 4.6.3, it is possible to identify the necessary phenomenological velocity value to reach the final experimental ozone density in the gas phase. This velocity is estimated to be $v = 0.2498\frac{m}{s}$. The methodology followed by the Authors to find its value is described in the Appendix. By performing a simulation with the newly identified forcing velocity value, the following results (Figure 4.6.4) are obtained.

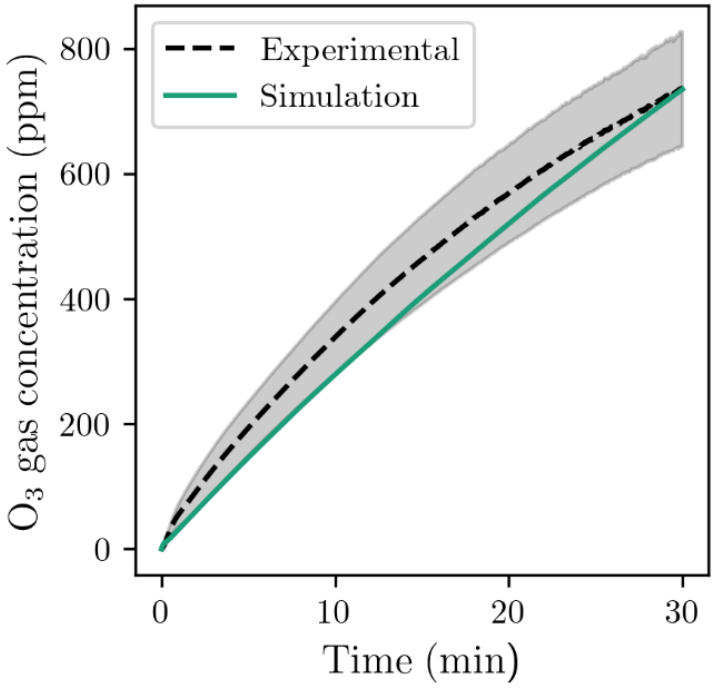

Figure 4.6.4 Comparison between the experimental and simulated ozone concentration time evolution considering a phenomenological forced transport velocity of $0.2498\frac{m}{s}$

As the results suggest, the ozone onset trend in the gas phase is well reproduced by the model; thus, the additional forcing term v helps to represent the species transport from the plasma to the gas region. By its order of magnitude, this term can be related to a superposition of multiple phenomena, such as ionic wind and thermal advection, that are not directly tracked in the model [18].

4.7 Conclusions

In the context of biomedical and industrial applications of plasmas, the SDBD plasma sources allow the separation of the plasma generation region from the treatment region, relying mostly on gas phase chemistry to sustain the process. Numerical modeling of such sources may increase the understanding of the key physical and chemical mechanisms in the treatment sustainment. As the complete representation of all the possible mechanisms occurring in the process would be computationally unaffordable, the adoption of an MGM allows for focusing on the

chemical effects involved in the plasma treatment while approximating the transport phenomena from the plasma region to the afterglow. In this study, an MGM was implemented in the SPPARK solver to understand the role of transport processes in the O_3 onset in a closed chamber placed underneath a LA-SDBD source. The results obtained in the simulations highlight how purely diffusive transport is insufficient to reproduce experimental results, thus requiring the adoption of a phenomenological constant forced transport term. In the model, the forced transport term has been included through a parametric study, resulting in a simulation that closely follows the experimental O_3 trend. This result supports the hypothesis that, in the analysed humid-air LA-SDBD plasma, additional transport mechanisms, similar in magnitude to ionic wind and thermally induced advection, play a significant role in the post-discharge species distribution. Future work should explore more refined transport models and the inclusion of dynamic feedback mechanisms to further enhance and generalise the model's predictive capabilities.

4.8 Appendix

4.8.1 Experimental procedure

The investigated plasma source is a large-area Surface Dielectric Barrier Discharge (LA-SDBD, AlmaPlasma s.r.l., Bologna, Italy), composed of 4 high voltage electrodes (internally cooled by a liquid flow), a thin dielectric layer, and a grounded perforated plate Figure 4.8.1). The source is operated at atmospheric pressure and is integrated into a PVC treatment chamber (14.34 L) to create a confined environment.

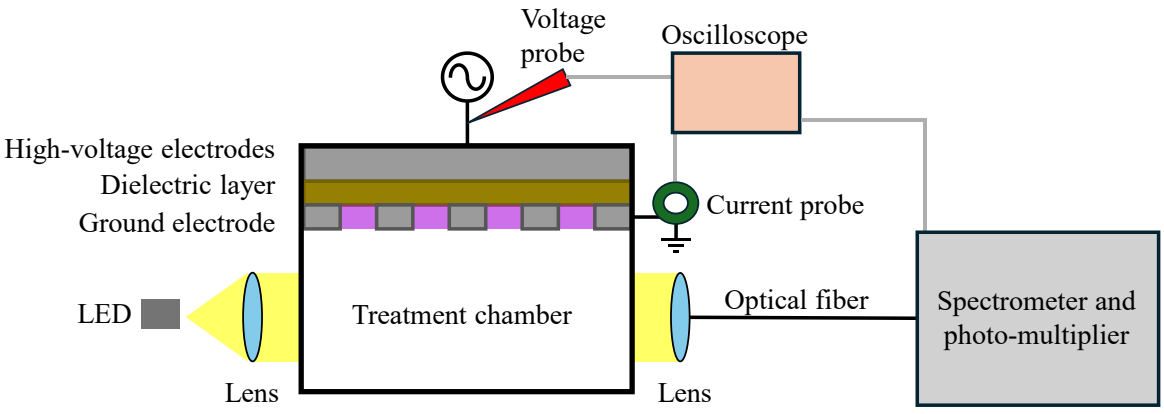

Figure 4.8.1 Experimental setup schematics. The plasma source is composed of high-voltage electrodes, a dielectric layer, and a grounded electrode. The (red) voltage probe and the (green) current probe are employed for electrical characterization, while the LED, the lenses, the spectrometer, and the photo-multiplier tube are key components for measuring the chemical kinetics.

The LA-SDBD is connected to a commercial high voltage generator (AlmaPulse, Almaplasma s.r.l, Bologna, Italy). Electrical characterization is performed by monitoring voltage and current waveforms with high-voltage (P6015A, 1000×, Rp = 100 MΩ, Tektronix, USA) and current probes (Current Monitor 6585, Pearson Electronics, USA) placed respectively on high-voltage and ground cables and connected to an oscilloscope (MSO46, Tektronix, USA), from which average power is calculated by applying the Ohm's law and then specific power density is derived by dividing the power by the discharge volume.

Ozone kinetics are quantified through OAS, using UV/visible LEDs (emitting at 253 nm), a spectrometer (Acton SP2500i, Princeton Instruments), and a photomultiplier tube (PMT—PD439, Princeton Instruments) for fast detection. The light beam is collimated with lenses and measured before and after passing through the treatment chamber (thanks to quartz optical windows on the walls). Then Lambert–Beer's law is applied to determine concentrations along a 25 cm optical path as a function of the reduction of the light beam intensity. As reported in Figure 4.8.2, nine different optical paths are chosen to ensure a representative and reliable average value over the whole treatment volume.

The gas temperature inside the chamber is simultaneously monitored with fiber-optic probes.

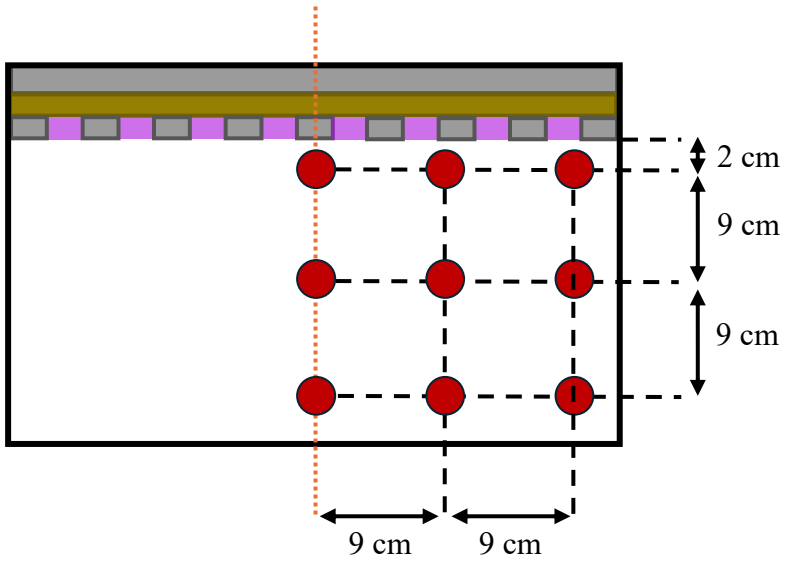

Figure 4.8.2 Optical paths. The nine circles represent the nine positions in which the kinetics are measured, allowing insights into the whole volume, under the hypothesis of symmetry of the discharge with respect to the central axis (orange dotted line).

4.8.2 Forcing term optimization

The identification of the best sitting forcing term $v = 0.2498\frac{m}{s}$ has been performed by fitting the final ozone computed concentrations obtained in each simulation, varying the forcing term v, to the second-degree polynomial (Figure 4.8.3).

$$F(v) = A + Bv + Cv^2 = 8.038 + 3.356 \cdot 10^3 v - 1.762 \cdot 10^3 v^2$$

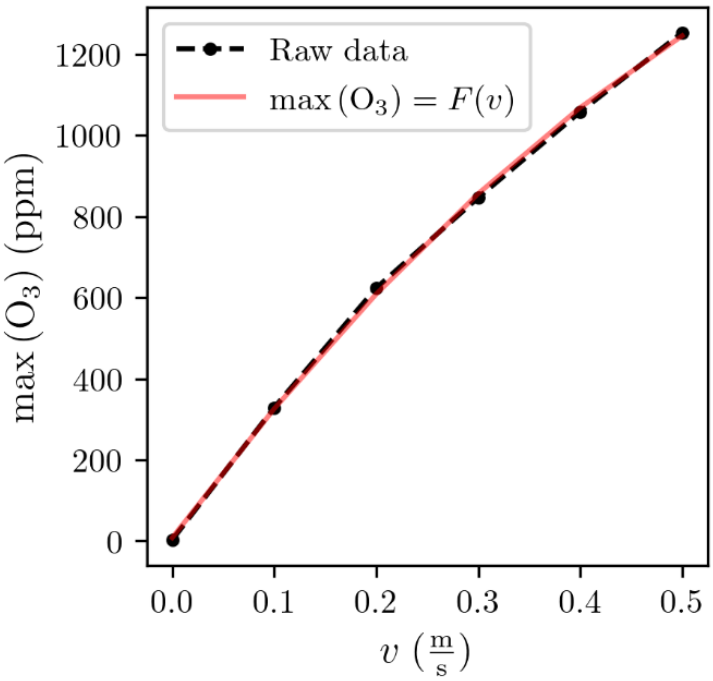

Figure 4.8.3 Fitting of the maximum ozone concentration against forced velocity magnitude trend with a second-degree polynomial (red line).

The adjusted R^2 $\left(R^2_{\text{adj}}\right)$ value for the polynomial fit has been calculated as follows:

$$R^2 = 1 - \frac{\sum_{i=1}^{n}\left(y_i - F(v_i)\right)^2}{\sum_{i=1}^{n}(y_i - \langle y \rangle)^2}$$

$$R^2_{\text{adj}} = 1 - \frac{(1 - R^2)(n-1)}{(n-p-1)} = 0.99879$$

where n is the total number of samples ($n = 6$ for $v \in [0.0, 0.1, 0.2, 0.3, 0.4, 0.5]\frac{m}{s}$), y_i is the i-th computed value of final ozone concentration, $F(v_i)$ is the value of ozone concentration predicted by the $F(v)$ function considering the i-th velocity, $\langle y \rangle$ represents the average value of the ozone concentration obtained from the

computations, and p is the number of free parameters in the $F(v)$ expression ($p = 3$ for the second-order polynomial $F(v) = A + Bv + Cv^2$).

By minimizing the error between the experimental Optical Absorption Spectroscopy final value ($736.28\ ppm$) and the $F(v)$ prediction, the $v^{\text{best}} = 0.2498 \frac{m}{s}$ has been obtained.

4.9 References

[1] Liao X, Liu D, Xiang Q, Ahn J, Chen S, Ye X and Ding T 2017 Inactivation mechanisms of non-thermal plasma on microbes: A review Food Control **75** 83–91

[2] Dubey S K, Parab S, Alexander A, Agrawal M, Achalla V P K, Pal U N, Pandey M M and Kesharwani P 2022 Cold atmospheric plasma therapy in wound healing Process Biochemistry **112** 112–23

[3] Bisag A, Isabelli P, Laghi G, Laurita R, Dirani G, Taddei F, Bucci C, Capelli F, Gherardi M, Paglianti A, Sambri V and Colombo V 2022 Cold atmospheric plasma decontamination of SARS-CoV-2 bioaerosols Plasma Processes and Polymers **19**

[4] Molina-Hernandez J B, Capelli F, Laurita R, Tappi S, Laika J, Gioia L, Valbonetti L and Chaves-López C 2022 A comparative study on the antifungal efficacy of cold atmospheric plasma at low and high surface density on Aspergillus chevalieri and mechanisms of action Innovative Food Science & Emerging Technologies **82** 103194

[5] Puligundla P, Lee T and Mok C 2016 Inactivation effect of dielectric barrier discharge plasma against foodborne pathogens on the surfaces of different packaging materials Innovative Food Science & Emerging Technologies **36** 221–7

[6] Katsigiannis A S, Bayliss D L and Walsh J L 2022 Cold plasma for the disinfection of industrial food-contact surfaces: An overview of current status and opportunities Comprehensive Reviews in Food Science and Food Safety **21** 1086–124

[7] Li X, Song S, Alderman D, Malik M A, Heller R and Jiang C 2019 Evaluation of electric field and charge on bio-substrates induced by nanosecond pulsed helium plasma jet IEEE International Pulsed Power Conference **2019-June**

[8] Deng X, Shi J and Kong M G 2006 Physical mechanisms of inactivation of Bacillus subtilis spores using cold atmospheric plasmas IEEE Transactions on Plasma Science **34** 1310–6

[9] Wang Y, Cheng C, Gao P, Li S, Shen J, Lan Y, Yu Y and Chu P K 2017 Cold atmospheric-pressure air plasma treatment of C6 glioma cells: Effects of reactive oxygen species in the medium produced by the plasma on cell death Plasma Science and Technology **19**

[10] Wang T, MacGregor S J, Anderson J G and Woolsey G A 2005 Pulsed ultra-violet inactivation spectrum of Escherichia coli Water Research **39** 2921–5

[11] Lamont Y, Rzezutka A, Anderson J G, MacGregor S J, Given M J, Deppe C and Cook N 2007 Pulsed UV-light inactivation of poliovirus and adenovirus Letters in Applied Microbiology **45** 564–7

[12] Kang S K, Choi M Y, Koo I G, Kim P Y, Kim Y, Kim G J, Mohamed A A H, Collins G J and Lee J K 2011 Reactive hydroxyl radical-driven oral bacterial inactivation by radio frequency atmospheric plasma Applied Physics Letters **98**

[13] Simoncelli E, Schulpen J, Barletta F, Laurita R, Colombo V, Nikiforov A and Gherardi M 2019 UV–VIS optical spectroscopy investigation on the kinetics of long-lived RONS produced by a surface DBD plasma source Plasma Sources Science and Technology **28** 095015

[14] Alves L L, Bogaerts A, Guerra V and Turner M M 2018 Foundations of modelling of nonequilibrium low-temperature plasmas Plasma Sources Science and Technology **27** 023002

[15] Sakiyama Y, Graves D B, Chang H W, Shimizu T and Morfill G E 2012 Plasma chemistry model of surface microdischarge in humid air and dynamics of reactive neutral species Journal of Physics D: Applied Physics **45** 425201

[16] Zhang X, Zhao Y and Yang C 2023 Recent developments in thermal characteristics of surface dielectric barrier discharge plasma actuators driven by sinusoidal high-voltage power Chinese Journal of Aeronautics **36** 1–21

[17] Bityurin V A and Bocharov A N 2017 Dynamic and Heat Effects in Sinusoidal Surface DBD IOP Conference Series: Materials Science and Engineering **249** 012008

[18] Ollegott K, Wirth P, Oberste-Beulmann C, Sakthi G S M, Magazova A, Hermanns P, Peters N, Schücke L, Bracht V, Agar D W, Awakowicz P and Muhler M 2023 Investigation of flow characteristics in a twin-surface dielectric barrier discharge reactor by Schlieren imaging Journal of Physics D: Applied Physics **56** 265201

[19] Marchetti A, Laurita R and Gherardi M 2025 SPPARK – a novel generalized simulation tool for non-equilibrium plasma chemistry Journal of Physics D: Applied Physics

[20] Goodwin D G, Moffat H K, Schoegl I, Speth R L and Weber B W 2024 Cantera: An Object-oriented Software Toolkit for Chemical Kinetics, Thermodynamics, and Transport Processes

[21] Hagelaar G J M and Pitchford L C 2005 Solving the Boltzmann equation to obtain electron transport coefficients and rate coefficients for fluid models Plasma Sources Science and Technology **14** 722–33

[22] Maccaferri C, Sainz-García A, Capelli F, Gherardi M, Alba-Elías F and Laurita R 2023 Evaluation of the Antimicrobial Efficacy of a Large-Area Surface Dielectric Barrier Discharge on Food Contact Surfaces Plasma Chemistry and Plasma Processing **43** 1773–90

[23] Tappi S, Nissen L, Casciano F, Antonelli G, Chiarello E, Picone G, Laurita R, Capelli F, Gherardi M, Maccaferri C, Gianotti A, Bordoni A, Espmark Å M, Capozzi F and Rocculi P 2023 Effect of cold plasma generated with different gas mixtures on safety, quality and nutritional aspects of fresh sea bream fillets Innovative Food Science and Emerging Technologies **89**

[24] Maccaferri C, Tomelleri F, Gherardi M and Laurita R 2025 Optimisation of plasma processes for decontamination of bacterial contaminants on polymeric food packaging materials Journal of Physics D: Applied Physics **58**

Chapter 5

Analytically Reduced Chemistry for non-equilibrium plasmas

5.1 Preface

This chapter addresses the application of Analytically Reduced Chemistry (ARC) techniques to non-equilibrium plasmas. In order to limit the computational cost associated with solving multidimensional numerical models, one possible strategy is to simplify the chemical complexity, thereby reducing both the stiffness of the numerical problem and the number of continuity equations to be solved. To this end, several ARC techniques - some well-established in the combustion research community and here adapted to the plasma context, and others newly developed - have been combined into a single comprehensive algorithm. Based on the simulation of an arbitrary number of case studies within a global model, this algorithm automatically and deterministically simplifies a given input reaction mechanism.

Within the context of this thesis, this represents the final step of a framework that, starting from a detailed reaction scheme, enables simulations that account for both electron kinetics and thermochemistry, incorporates the scheme into non–zone-averaged simulations through a multizone approach - thus providing more detailed insights into the chemical mechanisms of each phase - and derives from it a new reduced reaction mechanism tailored to the requirements of multidimensional numerical models.

5.2 Abbreviations

ARC: Analytically Reduced Chemistry

DRG: Directed Relation Graph

ILDM: Intrinsic Low Dimensional Manifold

ARCANE: Analytically Reduced Chemistry Nice and Efficient

DRGEP: Directed Relation Graph with Error Propagation

QSS: Quasi Steady-State

DIC: Direct Interaction Coefficient

EBE: Electron Boltzmann Equation

EEDF: Electron Energy Distribution Function

5.3 Introduction

One of the main advantages of non-equilibrium plasma applications in chemistry lies in the non-equilibrium gas composition induced by electron-impact processes. In the two-temperature multifluid approximation, electrons, driven by an external electromagnetic field, acquire a higher mean kinetic energy (i.e., temperature) compared to the neutral background species. Through collisions with these species, electrons shift the gas composition away from equilibrium. From a kinetic perspective, the non-equilibrium induced by electron collisions can be interpreted as an instability in the system, which naturally tends to relax back toward a stable configuration through particle-particle interactions. Part of these relaxation processes will result in an increase in the gas temperature, while another part will force changes in the gas chemical composition, leading to an overall enhancement of the chemical kinetics within the system (Figure 5.3.1). From a chemical standpoint, this probabilistic mechanism leads to the establishment of new reaction pathways involving excited states, ions, and radicals.

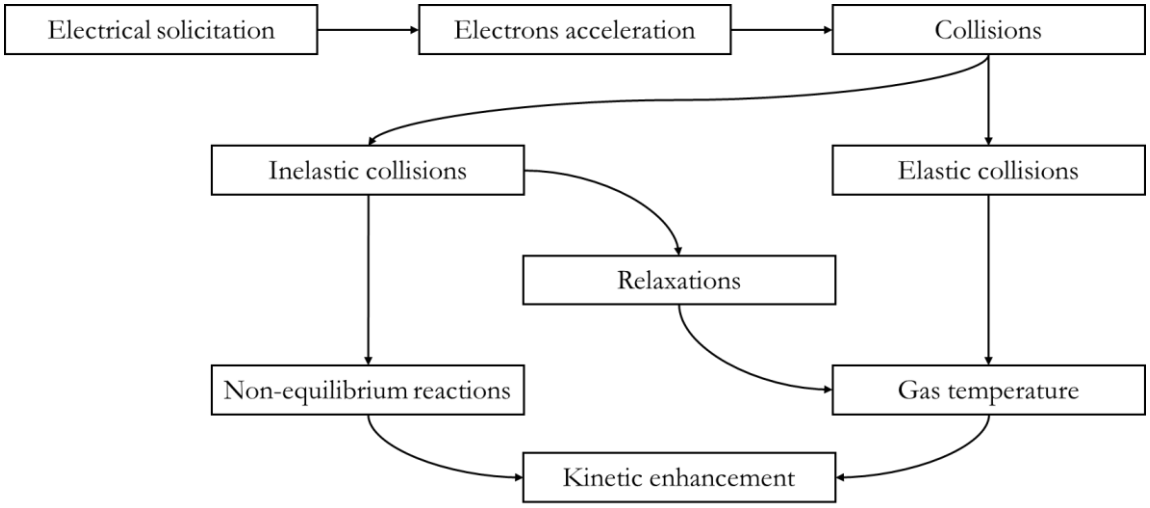

Figure 5.3.1 Conceptual pathway linking electron solicitation to chemical kinetics enhancement.

In the numerical modeling of plasma-chemical processes, which relies on a reaction set describing the interactions among the different species, the non-equilibrium induced by electron collisions results in an increased complexity of the chemistry sets in terms of both the number of species and the number of reactions. This represents a major challenge from a numerical perspective. Indeed, a larger number of species entails a larger number of continuity equations to be solved, while the number of reactions - especially those characterized by high rate constants - directly affects the numerical stiffness of the system. This limitation becomes particularly critical when, due to the geometric complexity of the application under study or to the need for an accurate spatial description of the

phenomena, multidimensional models (*i.e.,* fluid models) are required. In such cases, chemistry sets comprising only a few tens of species and several hundred reactions already become prohibitively complex to enable simulations at an affordable computational cost.

A possible solution to this issue lies in relaxing the requirement of maximum accuracy in the description of the chemical interactions within the system, in favour of a weighted approximation of the phenomena of interest in the specific case under study. To this end, Analytically Reduced Chemistry (ARC) techniques can be employed. Originally developed in the field of combustion modeling, these techniques can be broadly classified into three main families: *skeletal reduction techniques* [1–6] dealing with the reduction of chemical complexity by removing the chemistry set's components which are less relevant in the computation of control (output) quantities in the simulation; *lumping techniques* [7,8] which group together species with similar behaviour under a fictitious representative which is included in the chemistry set in place of the original species; *time-scale analysis techniques* [9,10] which approximate high rate reactions as partial equilibrium reactions and highly reactive species as quasi-steady state species.

In the plasma-chemistry field, several simplified approaches have been proposed to reduce the simulation cost of complex chemistries models and here a few examples are listed. Sakai *et al.* [1] used a graph-based approach, where species are introduced as nodes and reactions as directed edges, to analyse a plasma chemistry set for methane obtaining qualitative insights on the chemistry based on the graph geometry. Sun *et al.* [2] used the Directed Relation Graph (DRG) method by Lu and Law [3] for the CO_2 chemical kinetics in a gliding arc plasma. Obrusník *et al* [4] used a sensitivity analysis to determine the dominant processes in air plasmas. Hanicinec *et al.* [5] applied several skeletal reduction techniques on six chemistry sets under varying operative conditions. Berthelot *et al* [7] used the vibrational distribution function of vibrationally excited CO_2 states to lump together vibrational levels. Rehman *et al.* [9] applied the Intrinsic Low Dimensional Manifold (ILDM) technique to separate the fast (assumed in steady-state) and slow mechanisms in an argon plasma thus considering only the slow timescales in the chemical kinetics description.

Using a combination of three techniques, each belonging to a different family of techniques, a fully automatic procedure for the reduction of complex combustion chemistry sets to obtain computational fluid dynamics-ready chemistries, Analytically Reduced Chemistry Automatic Nice and Efficient (ARCANE), has been developed by Cazères *et al.* [11]. In particular, they used a combination of the Directed Relation Graph with Error Propagation (DRGEP) [6] as the skeletal technique targeting both species and reactions, a lumping step [8] based on the

thermodynamic similarity of isomers and the quasi-steady-state (QSS) [10] approximation as time-scale-based routine.

In this chapter, an adaptation of the *skeletal* and *lumping* steps from the ARCANE algorithm to non-equilibrium plasmas is proposed, providing an automatic and generalized procedure to effectively reduce the complexity of plasma chemistry-sets while controlling the error induced in the approximations.

5.4 Skeletal reduction

As previously mentioned, the focus of skeletal reduction techniques is to simplify an input chemistry set by rigidly removing groups of its constituents so that, in a simulation, the results produced by adopting the original (full) reaction set are similar to the ones obtained by adopting the reduced chemistry set. The procedure implies that a subset of the chemistry set constituents is irrelevant to the simulation results, which is only true if the full reaction set is sufficiently generalized. In other words, a skeletal reduction technique is effective and, thus, should be applied when, in a specific simulation, some of the theoretically possible chemical mechanisms have negligible effects on the desired results, and therefore, a reduced chemistry can be crafted to include only the relevant processes for the simulated cases.

In this context, how to identify a chemistry set component as irrelevant is the key to the algorithm's performance. In fact, according to the previous description and not accounting for the procedure's effectiveness, a chemistry set could be reduced simply by randomly selecting species and reactions, removing them, running a new simulation, and evaluating the effect of their deletion. To avoid inefficient randomness and optimize the reduction, a better approach would be to create a ranking of similar chemistry set components (reducing species and reactions separately) based on their influence on the desired simulation outputs. Under these circumstances, the skeletal techniques differentiate based on whether they focus on species (species-oriented techniques) or reactions (reaction-oriented techniques) removal, and on the specific metrics used to define the component importance in the simulation.

Lastly, it is worth mentioning that the reduction procedure effects cannot be known *a priori*, and the implications of the component removal must be evaluated on the new simulation. This entails that the component ranking procedure cannot directly provide the extent of the reduction, and thus the number of components to be removed in a batch. For these reasons, the reduction procedure with a skeletal reduction technique should proceed iteratively by progressively removing components and evaluating the induced error in the reduced chemistry by such deletion at each iteration, until a user-defined condition on such error is met.

Among the skeletal reduction techniques, the DRGEP was chosen as the skeletal method of use for non-equilibrium plasma chemistry, as it can be aimed at the removal of both species and reactions. An overview of the reduction algorithm characteristics is provided in the next sections.

5.4.1 DRGEP species-oriented

The purpose of a species-oriented skeletal reduction technique is to simplify an input chemistry set by iteratively removing the less relevant species in the desired (under examination) subgroup of phenomena. Moreover, the key point of the whole algorithm is how the species ranking is performed.

The DRGEP species-oriented algorithm adopts a strategy based on the chemistry set representation through a directed graph. In the graph, the species are represented by the graph nodes, and the directed edges represent the influence of the tail species in the production (or consumption) of the head species; the longer the edge, the less relevant the tail species is for the head species.

5.4.1.1 Directed graph construction algorithm

The first step to build the chemistry set directed graph representation is to include the species as graph nodes. The nodes will be characterized by: a name (the species name), an initial random position (which is not fixed and will be modified afterwards) in the graph system of coordinates, and a list of directed edges connected to it (empty at this stage). Once all the species have been included, the edges can be initiated. A directed edge is defined through: a tail node (the node from which the edge departs), a head node (the node to which the edge is directed), and a length. To initialize the edges, the DRGEP algorithm involves assigning the length of an edge by means of the Direct Interaction Coefficient (DIC). For the species-oriented algorithm, the DIC definition is obtained as follows:

$$r_{AB}(\mathrm{t}) = \frac{\left|\sum_{j=1,R} \nu_{A,j}^{n} \dot{\omega}_j(t) \delta_B^j\right|}{\max\left(P_A(t), C_A(t)\right)} \tag{5.1}$$

where A is the head species, B is the tail species, j is the reaction index (thus, the sum extends to all the R reactions in the chemistry set), $\nu_{A,j}^{n}$ is the net stoichiometric coefficient of species A in the reaction j, $\dot{\omega}_j$ is the reaction rate $\left(\frac{kmol}{m^3\ s}\right)$, P_A is the species A rate of production $\left(\frac{kmol}{m^3\ s}\right)$, C_A is the species A rate of consumption $\left(\frac{kmol}{m^3\ s}\right)$ and δ_B^j is a function to check if the species B is involved in the reaction j, defined as follows:

$$\delta_B^j = \begin{cases} 1, & if\ B \in \mathrm{Reac}(j) \vee B \in \mathrm{Prod}(j) \\ 0, & else \end{cases}$$

with $\mathrm{Reac}(j)$ and $\mathrm{Prod}(j)$ representing respectively the list of reactants and the list of products of the reaction j.

It is worth noting that r_{AB}(t) does not represent the DIC coefficient yet, as it is a function of time (*i.e.,* computing the $B \rightarrow A$ edge's length by means of this coefficient would imply building a directed graph for each time instant). Moreover, the notation should be extended to include multiple cases of interest (multiple simulations), thus using $r_{AB}^{(\kappa)}(t)$ to represent the κ-th simulation case. The case and time-independent DIC coefficients are then obtained by taking:

$$r_{AB} = \max_{t,\kappa} r_{AB}^{(\kappa)}(t) \tag{5.2}$$

The $B \rightarrow A$ edge's length can be obtained from r_{AB} by taking its inverse:

$$\lambda_{B \rightarrow A} = \frac{1}{r_{AB}} \tag{5.3}$$

Supposing that a group of simulations of the complete (initial) chemistry set for the case studies of interest has already been performed, the procedure can use the simulations' results ($\dot{\omega}_J$, P_A and C_A) in the time domain (t) for each case (κ).

The last point that needs to be addressed is the position of the nodes in the graph. This aspect is rather secondary for the reduction, as the ranking and reduction steps only rely on the $\lambda_{B \rightarrow A}$ length. Nonetheless, to allow the graph representation, it is worth mentioning that the position of the nodes can be unambiguously identified only if, starting from a random reference node, all the inter-node distances are satisfied. This criterion is observed by allowing the graph edges to be curves rather than only straight lines. In this sense, the shortest edges' lengths uniquely determine the relative positions of the nodes.

An idealized representation of a possible graph produced by this approach is shown in Figure 5.4.1.

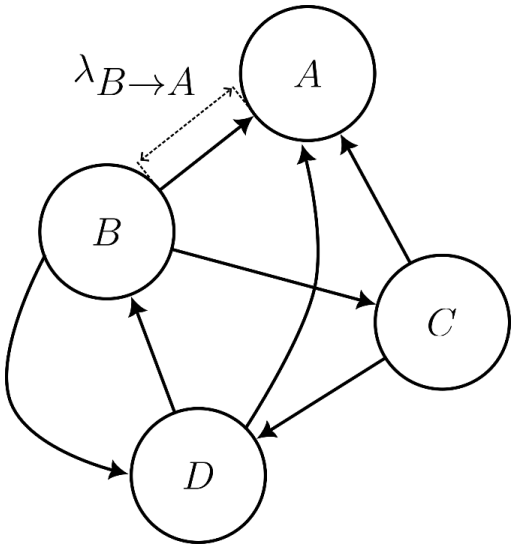

Figure 5.4.1 Idealized representation of a directed graph representing a chemistry set

5.4.1.2 Species ranking

It has to be noted that until now, the procedure has been independent of the chemistry set optimization to accurately account for only the subset of phenomena of interest. Thus, in principle, it can be used to rank the species for any phenomena captured by the original chemistry set.

In order to simplify the reaction set, it is first necessary to identify which species (hereafter referred to as target species) are the most relevant for the phenomena of interest. These chemical compounds (which have to be defined by the user and obtained by previous analysis of the simulations' results) will be the ones that will stir the reduction procedures and whose concentrations' results will be the most consistent throughout the whole chemistry set ensemble.

In this context, the chemistry set species ranking will be obtained by means of the graph's edges length pointing from each species to any of the target species nodes.

The most simplistic approach to compute the species importance ranking in the chemistry set would be to consider the length of all the edges having any of the target species as head nodes. Subsequently, the overall importance of a given species is obtained by the shortest of the edges departing from its representative node towards the complete list of target species. In other words, the species' importance is determined by:

$$\Upsilon_q = \min \lambda_{q\to T_i}, \qquad \forall T_i \in \vec{T} \tag{5.4}$$

where T_i represents the i-th target species, $\vec{T}$ represents the ensemble of target species and Υ_q represents the importance score of the q-th non-target species. By

considering the scores in descending order, the species ranking is obtained. The last species in the ranking is then removed from the chemistry set.

Nonetheless, this first approach neglects the effect of indirect interactions between species. For example, when considering an idealized case with four species (three non-target species - S_1, S_2 and S_3 - and a target species - T) as represented in Figure 5.4.2.

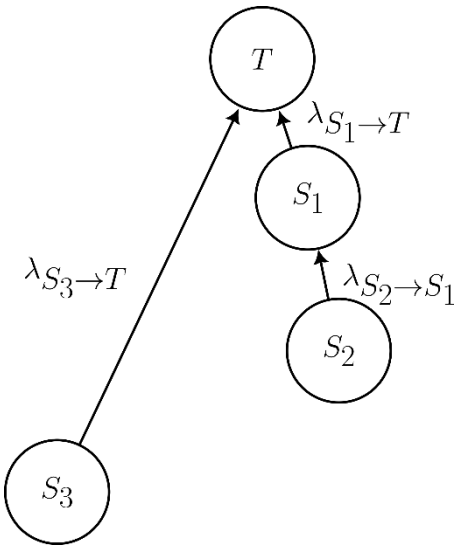

Figure 5.4.2 Example case: three chemical species connected to a target one. Discussion on how the edge's length ranking is limiting.

According to equation (5.4), $\Upsilon_{S_2} \to \infty$ which implies that S_2 registers the lowest position in the species ranking and should be removed from the set. Nonetheless, by removing S_2 a large error in the S_1 concentration would be induced, which then would reflect on the T concentration as S_1 is the most impactful species on T. This simplistic example highlights the shortcomings of the previously described approach. Constraining the importance score evaluation based only on the direct connections between nodes is often too approximate.

For these reasons, a better approach would be to reformulate equation 5.4 to adopt as the $\lambda_{q \to T_i}$ distance the shortest possible path connecting the q-th species to the i-th target ($\psi_{q \to T_i}$), even if it includes additional nodes. The importance score definition then becomes:

$$\Upsilon_q = \min \psi_{q \to T_i}, \qquad \forall T_i \in \vec{T} \tag{5.5}$$

It has to be mentioned that this approach increases the computational cost of the reduction algorithm as it requires the adoption (and execution) of an additional shortest path finding algorithm coupled with the species-oriented DRGEP. In the

ARC module implementation in SPPARK, Dijkstra's algorithm [12] was adopted to identify the shortest path, here diverging from the approach suggested in ARCANE [11].

5.4.1.3 Induced error evaluation

The reduced chemistry set can be crafted once the species ranking has been obtained. The last species in the ranking is removed from the reaction set. As it no longer exists in the set, the species deletion implies that also all the reactions involving the removed species have to be erased. The obtained reduced chemistry set can now be used to perform all the case study simulations of interest. As the reduced reaction set accuracy is shifted towards the computation of the target species concentrations, the error induced by the reduction should be evaluated only on these species.

The target species discrepancy can be computed as follows:

$$\xi_{T_i} = \max_{t,\kappa} \left| \frac{n_{T_i}^{(\kappa)}(t) - n_{0,T_i}^{(\kappa)}(t)}{n_{0,T_i}^{(\kappa)}(t)} \right| \tag{5.6}$$

where $n_{T_i}^{(\kappa)}(t)$ represents the concentration of species T_i at time t for case κ calculated using the reduced chemistry set and $n_{0,T_i}^{(\kappa)}(t)$ represents the concentration of species T_i at time t for case κ calculated using the original (complete) one.

Finally, the overall discrepancy between the reduced and complete set can be defined as:

$$\Xi = \max_{T_i} \xi_{T_i} \tag{5.7}$$

5.4.1.4 Algorithm convergence

The reduction algorithm, as described in the previous paragraphs, refers to a single reduction step. As mentioned in Section 5.4, the procedure needs to be iterative as the exact effect of the chemistry set modification cannot be easily predicted. In the iterative approach, if the user-imposed tolerance isn't satisfied by equation 5.7 at the first iteration, the graph and species ranking (equations 5.1 to 5.4) need to be re-evaluated based on the results of the reduced chemistry set obtained at the previous iteration. To further clarify this aspect, the equation 5.1 is here reported for a generic τ reduction step (*i.e.,* algorithm iteration).

$$\left[r_{AB}^{(\kappa)}(t)\right]^{\tau} = \frac{\left|\sum_{j=1,[R]^{\tau-1}} \nu_{A,j}^{n}\left[\dot{\omega}_j^{(\kappa)}\right]^{\tau-1}\delta_B^j\right|}{\max\left(\left[P_A^{(\kappa)}\right]^{\tau-1},\left[C_A^{(\kappa)}\right]^{\tau-1}\right)}, \qquad \forall\tau = 1,2,\ldots \tag{5.1a}$$

where $[R]^{\tau-1}$ represents the number of reactions included in the chemistry set obtained at the previous iteration, and $\left[\dot{\omega}_j^{(\kappa)}\right]^{\tau-1}$, $\left[P_A^{(\kappa)}\right]^{\tau-1}$ and $\left[C_A^{(\kappa)}\right]^{\tau-1}$ are obtained through the simulation of the previous iteration reaction set. Once the graph is obtained, the algorithm can continue with the same steps of the first iteration.

By iteratively reducing the chemistry set complexity, the error Ξ (always computed by referring to the original reaction set results) progressively increases until the user-imposed convergence criterion is met.

Defining the τ^* iteration such that $\Xi^{\tau^*} \geq$ Tol, the final reduced chemistry set will be characterized by a number of species $S^{\tau^*} = S^0 - \tau^*$ and a number of reactions R^{τ^*}.

5.4.1.5 Algorithm control

Some remarks about the DRGEP species-oriented method control can finally be stated.

A first observation can be made about the meaning of the error induced in the target species. As mentioned above, the target species are chosen by the user as identifiers of a peculiar phenomenon of interest. Building a chemistry set that induces an error in these species computation could seem detrimental, but it only reflects the effect of the removal of minor phenomena on the targets. In other words, inducing an error in the target species computations forces the algorithm to remove the less relevant phenomena from the chemistry set, thus, the extent of the reduction and tailoring of the reaction set to the desired subset of mechanisms can be controlled by the magnitude of the convergence parameter specified by the user.

A second consideration concerns the extent of the reduction based on the number of test cases (κ) included in the DIC computation. In this context, considering a larger number of test cases widens the validity domain of the chemistry set. Taking into account only one test case (*i.e.,* a specific initial thermodynamic state and power signal) will make the chemistry set formally valid only for the examined conditions as it won't consider the nuances of the phenomena in the DIC computation, thus reducing the probability for an edge to be sufficiently short as suggested by equation 5.2. For these reasons, the chemistry set obtained by considering only the necessary test cases will be the most reduced as possible.

Furthermore, a third remark on the amount of target species (*i.e.,* multitude of phenomena of interest). Similarly to the previous point, as expressed in equation 5.5, a large amount of target species affects negatively the reduction because it becomes increasingly probable that a non-target species will have some interesting effect on at least one of the targets. Furthermore, from equations 5.6 and 5.7, it becomes likelier that at least one of the errors induced in the target species' computations will excide the user-imposed convergence error threshold. Summarizing, the larger the number of interesting phenomena for the chemistry set usage is, the larger S^{τ^*} can be.

Lastly, a consideration on the effect of the considered time domain. From the reduction algorithm perspective, it is not necessary to share the same time domain in both the simulations and the DIC evaluation in equation 5.2. In fact, once the simulation results have been obtained in the complete time domain, a subdomain of arbitrary time samples can be used to affect the reduction outcomes. For example, if the phenomena of interest mostly occur in the early stages of the simulation, the reduction algorithm can be forced to consider only the first few time samples (with an arbitrary time-step). Doing so, the chemistry set produced by the algorithm can be adjusted to account mostly for the shorter phenomena.

5.4.1.6 Pseudocode algorithm summary

The following pseudocode is provided to summarize the algorithm structure.

A. Directed graph construction

Inputs: Chemistry set, previous simulations' results and reduction times samples (t)

Algorithm:

a. *Create an empty directed graph object*

b. *Add a node in the directed graph for each species in the chemistry set*

c. *For each node in the directed graph (becomes the tail node - B), pick a second node (the head node - A)*

   i. *Compute* $r_{AB}^{(\kappa)}(t)$ *the AB couple for each case and each instant in time (considering all the reactions) from the previous simulations' results*

   ii. *Compute* $r_{AB} = \max_{t,\kappa} r_{AB}^{(\kappa)}(t)$

   iii. *Get* $\lambda_{B\to A} = \frac{1}{r_{AB}}$

   iv. *Add the node* $B \to A$ *to the directed graph*

Outputs: Directed graph representative of the chemistry set

B. Species ranking

Inputs: Directed graph representative of the chemistry set & a list of target species

Algorithm:

a. *For each species* (T_i) *in the target group and for each species* (q) *not in the target group compute the* $\psi_{q\to T_i}$ *path length through the Dijkstra's algorithm*

b. *Compute* $Y_q = min\,\psi_{q\to T_i}$, $\forall T_i \in \vec{T}$

c. *Remove the* q^* *species characterized by* $Y_{q^*} = \max_q Y_q$ *and all the reactions involving the* q^* *species*

Outputs: Reduced chemistry set

C. Induced error evaluation & convergence

Inputs: Reduced chemistry set, list of simulations, list of target species & convergence criteria (Tol)

Algorithm:

a. For each case (κ) *in the list of simulations, simulate the reduced chemistry set.*

b. Evaluate $\xi_{T_i} = \max_{t,\kappa} \left| \frac{n_{T_i}^{(\kappa)}(t) - n_{0,T_i}^{(\kappa)}(t)}{n_{0,T_i}^{(\kappa)}(t)} \right|$ *for each target species* (T_i)

c. Evaluate $\Xi = \max_{T_i} \xi_{T_i}$

d. Evaluate if $\Xi \geq Tol$

Case: True

Stop the loop

Case: False

Reduced chemistry set is new input of the Directed graph construction

Outputs: Reduced chemistry set

5.4.2 DRGEP reaction-oriented

In a reaction-oriented skeletal reduction technique, chemical reactions are the chemistry set's components to be ranked and removed.

The DRGEP reaction-oriented algorithm is structured similarly to the species-oriented one as it shares the strategy of the chemistry set representation through a directed graph, but with some constitutive differences. In fact, in this case, not only the species are represented as graph nodes, but also the reactions. The first will act only as head nodes whilst the latter as tail nodes. In contrast with the species-oriented case, the edges of such graph will represent the influence of the single reaction node on the production (or consumption) of the species node. As in the previous case, the longer the edge, the less relevant the tail reaction is for the head species. Once the reactions have been classified based on their weight in the chemistry set, the lowest scoring one can be removed and its effect evaluated on the simulation cases.

5.4.2.1 Directed graph construction algorithm

Similarly to the species-oriented algorithm, the first step of the method is to build the directed graph. As mentioned before, in this case both the species and reactions are represented by means of the graph nodes. As in the species-oriented algorithm, each node will be characterized by a name, and a list of edges that connect to it. To complete the graph, the edges need to be included by means of a tail node, a head node, and a length. Also in this case, the edges length is defined thorough the DIC of the tail reaction and the head species.

$$r_{Aj}(t) = \frac{\left|\nu_{A,j}^{n}\dot{\omega}_j(t)\right|}{\max\left(P_A(t), C_A(t)\right)} \tag{5.8}$$

where r_{Aj} represents the influence of the j-th reaction on the species A, $\nu_{A,j}^{n}$ represents the net stoichiometric coefficient of the species A in the j-th reaction, $\dot{\omega}_j$ is the reaction rate $\left(\frac{kmol}{m^3\ s}\right)$, P_A is the A species rate of production $\left(\frac{kmol}{m^3\ s}\right)$, and C_A is the A species rate of consumption $\left(\frac{kmol}{m^3\ s}\right)$.

Extending the notation to multiple simulation cases, it is possible to compute the time and case independent DIC as:

$$r_{Aj} = \max_{t,\kappa} r_{Aj}^{(\kappa)}(t) \tag{5.9}$$

where r_{Aj} represents the DIC value and κ is the simulation case's index.

The $j \rightarrow A$ edges length can be obtained, as in the species-oriented method, by the inverse of the DIC value:

$$\lambda_{j\rightarrow A} = \frac{1}{r_{Aj}} \tag{5.10}$$

Also in this case, an illustrative representation of the directed graph is provided in Figure 5.4.3.

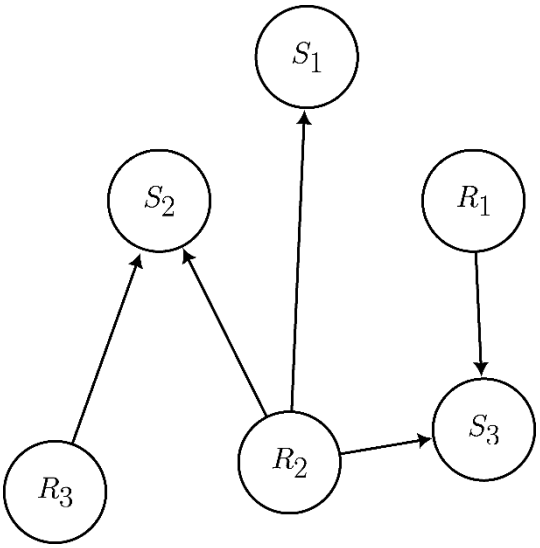

Figure 5.4.3 DRGEP reactions-oriented directed graph example. In the example three species (S_1, S_2 and S_3) and three reactions (R_1, R_2 and R_3) are included in the graph.

5.4.2.2 Reactions ranking

The fundamental difference between the species and reactions-oriented algorithms arises in the reactions ranking step for two major reasons. The first one concerns the structure of the directed graph. In fact, this is characterized by the impossibility of accounting for non-direct interactions between nodes (*i.e.,* no reaction node can be a head node for an edge). This aspect affects the reactions ranking as it implies that the importance score of the reactions must be computed using the edges length directly as a more complex path is non-existent. The second basis of difference with respect to the species-oriented mechanism comes from the nature of the reduction target of the algorithm. In fact, in this case, the method focuses on removing single reactions form the chemistry set. Ranking the reactions by considering only their importance with respect to the target species would result in an equivalent score for all the reactions that are not affecting mole balance of such species (*i.e.,* reactions characterized by a stoichiometric balancing of production and consumption of target species moles and reactions not involving the target species at all). This aspect would destabilize the method effectiveness in controlling the error induced by the reduction, which is only granted by the presence of a sorted ranking of components that are safe to remove. To avoid this issue, the reactions ranking must be weighted on all the species present in the chemistry set.

In light of these considerations, the reactions' importance score is defined as follows:

$$\Upsilon_j = \min_{A \in S} \lambda_{j \to A}\,, \tag{5.11}$$

where the minimum evaluation has been extended to all the species (S) in the chemistry set.

This reaction ranking procedure implies that the reactions will be removed from the reaction set based on their global relevance in the multitude of phenomena involved in the graph construction. Thus, the chemistry set targeting towards the representation of just the desired subset of phenomena is not granted by default by the algorithm but can only be controlled by the iterative procedure of the induced error in the target species computation estimation. Furthermore, as the simplification is non-specific, the same phenomena accurately represented by the initial chemistry set will be approximately considered just as effectively in the reduced set, making the use of a pre-targeted reaction set as input to the algorithm interesting.

5.4.2.3 Induced error evaluation and algorithm convergence

The error evaluation of the reaction-oriented algorithm closely follows the same principles expressed in Section 5.4.1.3. In fact, also in this case the error induced by the reactions' removal on the target species computations and the overall discrepancy between the reduced and complete set can be defined computed by equations 5.6 and 5.7 respectively.

Analogously, the algorithm iteration procedure is largely shared with the species-oriented algorithm (Section 5.4.1.4). In this case it is also possible to use the simulations results obtained from previous iterations' reactions sets to calculate the time and case dependent DIC coefficients:

$$\left[r_{Aj}^{(\kappa)}(t)\right]^{\tau} = \frac{\left|\nu_{A,j}^{n}\left[\dot{\omega}_{j}^{(\kappa)}\right]^{\tau-1}\right|}{\max\left(\left[P_{A}^{(\kappa)}\right]^{\tau-1},\left[C_{A}^{(\kappa)}\right]^{\tau-1}\right)}, \qquad \forall\tau = 1,2,\ldots \tag{5.8a}$$

with τ being the iteration index.

Also in this case, the τ^* iteration will be defined such that $\Xi^{\tau^*} \geq \mathrm{Tol}$ (with Tol representing the user-defined tolerance). At the end of the algorithm, the final reduced chemistry set will be characterized by a number of reactions $R^{\tau^*} = R^0 - \tau^*$ and a number of species S^{τ^*}. For completeness, it's worth mentioning that, in contrast with the species-oriented algorithm, in this case the number of species S^{τ^*} will most likely remain unchanged during the algorithm execution as a species should be removed only in the occurrence of it not being involved in any reaction.

5.4.2.4 Pseudocode algorithm summary

The following pseudocode is provided to summarize the algorithm structure.

A. Directed graph construction

Inputs: Chemistry set, previous simulations' results and reduction times samples (t)

Algorithm:

a. *Create an empty directed graph object*

b. *Add a node in the directed graph for each reaction and for each species in the chemistry set*

c. *For each reaction node in the directed graph (becomes the tail node - j), pick a species node (the head node - A)*

i. *Compute* $r_{Aj}^{(\kappa)}(t)$ *for the Aj couple for each case and each instant in time from the previous simulations' results*

ii. *Compute* $r_{Aj} = \max_{t,\kappa} r_{Aj}^{(\kappa)}(t)$

iii. *Get* $\lambda_{j\to A} = \frac{1}{r_{Aj}}$

iv. *Add the node* $B \to A$ *to the directed graph*

Outputs: Directed graph representative of the chemistry set

B. Species ranking

Inputs: Directed graph representative of the chemistry set

Algorithm:

a. *For each reaction* (j) *in the chemistry set compute* $Y_j = \min_{A\in S} \lambda_{j\to A}$

b. *Remove the* j^* *reaction characterized by* $Y_{j^*} = \max_j Y_j$ *and all the species not involved in any reaction*

Outputs: Reduced chemistry set

C. Induced error evaluation & convergence

Inputs: Reduced chemistry set, list of simulations, list of target species & convergence criteria (Tol)

Algorithm:

a. *For each case* (κ) *in the list of simulations, simulate the reduced chemistry set.*

b. *Evaluate* $\xi_{T_i} = \max_{t,\kappa} \left| \frac{n_{T_i}^{(\kappa)}(t) - n_{0,T_i}^{(\kappa)}(t)}{n_{0,T_i}^{(\kappa)}(t)} \right|$ *for each target species* (T_i)

c. *Evaluate* $\Xi = \max_{T_i} \xi_{T_i}$

d. *Evaluate if* $\Xi \geq Tol$

Case: True

Stop the loop

Case: False

Reduced chemistry set is new input of the Directed graph construction

Outputs: Reduced chemistry set

5.5 Chemistry Lumping

The family of chemistry lumping techniques entails simplifying an initial chemistry set through a structural reformulation of the set to an approximately equivalent one. Specifically, the objective of the techniques is to reduce the number of species and reactions necessary to represent the phenomena involved in the initial chemistry set, but with an approach intrinsically different from the one adopted by the skeletal reductions. In greater detail, these techniques rely on grouping similar species and reactions under surrogate representatives that inherit the thermodynamic and kinetic properties of their constituents. Through this approach, it is possible to obtain reaction sets globally behaving similarly to their predecessors (*i.e.,* all the phenomena considered in the original chemistry set will approximately be accounted for also in the reduced one) with a much less intricate and dense scheme.

The chemistry lumping techniques have been mostly developed for pure thermochemical (*i.e.,* combustion) models where isomer species can be grouped together in the reaction set, as their common composition won't affect the mole balance of the reactions. For this reason, especially in state-to-state reaction sets, the reduction supported by a lumping technique could be extremely beneficial for non-equilibrium plasma chemistry as, in addition to isomers, also the excited states of chemical species could potentially be grouped together under a single representative.

In this section, a novel lumping technique for non-equilibrium plasma chemistry developed during this PhD will be presented.

5.5.1 A novel lumping technique for plasma chemistry

5.5.1.1 Lumping technique overview

As mentioned above, the scope of a lumping technique is to simplify an initial chemistry set by replacing groups of its components with fictious representatives. The lumping technique here discussed will focus on species lumping through the introduction of a lump representative species (L_γ) that will need to be defined both thermodynamically and kinetically (*i.e.,* a reaction subset involving the representatives requires the definition of new reactions). The number of lump representative species depends on the number of identified groupings of species. In fact, not only multiple isomers and state manifolds could be present in a chemistry set, but the selection of species to be grouped together can also be refined from the simple composition sharing criteria considering further similarities between the species. For example, in ARCANE [11] the authors describe a rationale, designed for thermochemical reaction sets, to identify different

subgroups in isomeric species based on their thermodynamic properties. Similarly for non-equilibrium plasma chemistry, multiple criteria could be used, grouping species based on their composition and subsequently by thermodynamic similarity, excitation type, and further restrictive conditions.

Once the lumping groups have been identified, the lump representative species can be defined. To ensure that the reaction set obtained from the lumping procedure will be equally valid with respect to the original chemistry set, the novel species characteristic (*i.e.,* thermodynamic properties and reaction kinetics role) should be inherited from the single component of the lump. Furthermore, as the relevance of species in a chemistry set is not uniform, each characteristic of the original species should be considered with different weights for the definition of the lumped representative. For these reasons, it is useful to introduce the species-to-lump fraction parameter:

$$D_{i,L_\gamma} = \frac{n_i}{\sum_{q \in \hat{L}_\gamma} n_q} \tag{5.12}$$

where n_i represents the i-th species concentration, $\hat{L}_\gamma$ the γ-th lumping group, L_γ the γ-th lump representative species, and D_{i,L_γ} the species-to-lump fraction of the i-th species with respect to the γ-th lump. In this expression, is worth noting that the $\sum_{q \in \hat{L}_\gamma} n_q(t)$ summation term represents the overall lump concentration (*i.e.,* the γ-th lump representative species concentration).

Starting from the thermodynamic properties' definition of the lumped species, the generic y_{L_γ} attribute of the γ-th lump representative species (*i.e.,* molar heat at constant pressure - $\hat{c}_p$, molar enthalpy of formation - $\hat{h}$ or molar entropy of formation - $\hat{s}$) can be defined as:

$$y_{L_\gamma}(T_g) = \sum_{q \in \hat{L}_\gamma} D_{q,L_\gamma} \cdot y_q(T_g) \tag{5.13}$$

where y_q refers to the q-th species belonging to the $\hat{L}_\gamma$ lumping group and T_g represents the gas temperature.

On the other hand, the lumped species contribution to reactions' kinetics can be expressed through the definition of new lumped reactions rate constants such that the mole balance of the lumped representative species is consistent with the mole balances of each lump constituent. This implies that:

$$\frac{dn_{L_\gamma}}{dt} = \sum_{q \in \hat{L}_\gamma} \frac{dn_q}{dt} \tag{5.14a}$$

Expanding equation 5.14a the following expression can be obtained:

$$\frac{dn_{L_\gamma}}{dt} = \sum_{q \in \hat{L}_\gamma} \sum_{j=1}^{R} \nu_{q,j}^{n} \left(k_j^f \prod_{z=1}^{S} n_z^{\nu_{z,j}^f} - k_j^r \prod_{z=1}^{S} n_z^{\nu_{z,j}^r} \right) \tag{5.14b}$$

where $\nu_{q,j}^n$, $\nu_{q,j}^f$ and $\nu_{q,j}^r$ represent the q-th species net, forward and reverse stoichiometric coefficient in the j-th reaction $\left(\nu_{q,j}^n = \nu_{q,j}^r - \nu_{q,j}^f\right)$, k_j^f and k_j^r the j-th reaction forward and reverse rate coefficients, R is the initial chemistry set number of reactions, and S is the initial chemistry set number of species.

Introducing the D_{i,L_γ} coefficients in equation 5.14b the definition of the lumped reactions (*i.e.,* reactions where the L_γ lump representative species is involved) coefficients can be obtained (see Section 5.9.1):

$$\begin{cases} \tilde{k}_j^f = \sum_{\eta \in R: \eta \sim j} \left(k_\eta^f \prod_{\hat{L}_\gamma \in \Lambda} \prod_{q \in \hat{L}_\gamma} D_{q,L_\gamma}^{\nu_{q,\eta}^f} \right) \\ \tilde{k}_j^r = \sum_{\eta \in R: \eta \sim j} \left(k_\eta^r \prod_{\hat{L}_\gamma \in \Lambda} \prod_{q \in \hat{L}_\gamma} D_{q,L_\gamma}^{\nu_{q,\eta}^r} \right) \end{cases} \tag{5.15}$$

where the expressions have been extended to multiple lumping groups (Λ) and the notation of reaction similarity ($\eta \sim j$) has been introduced. The condition for two reactions to be similar is that, once the all the lumps' representative species have been substituted, different reactions' equations become overlapping. In other words, if two reactions' equations involve species belonging to the same lump with the same stoichiometric coefficients, the two reactions can be considered as similar (thus their respective effects can be summed in the lumped chemistry set). Following this definition, it is worth noting that the stoichiometric coefficients $\nu_{q,\eta}$ are invariant for all the q species in the $\hat{L}_\gamma$ lump and all the reactions η similar to j, which implies that they could be substituted in the expression with a common stoichiometric coefficient $\nu_{L_\gamma,j}$.

In summary, the lumping technique consists in identifying Λ groups of species based on a shared chemical composition and, secondarily, on their thermodynamic similarity and excitation type. These species are then removed from the chemistry

set and replaced by a representative species whose thermodynamic properties are weighted according to the relevance of each individual species within the lump expressed through the D_{i,L_γ} ratio (equation 5.13). Furthermore, the lump representative must replace the original species in all reactions, with similar reactions being merged, and new reaction rate constants must be defined based on the original ones (also weighted by the D_{i,L_γ} ratios), as expressed by equation 5.15.

5.5.1.2 Species-to-lump ratios computations

Equations 5.13 and 5.15 explicit the dependence of the thermodynamic and kinetic aspects of the lumped chemistry set on the species-to-lump ratios $\left(D_{i,L_\gamma}\right)$. For this reason, it becomes evident that the accuracy of the reduction procedure relies on their expressions' determination.

In general, D_{i,L_γ} ratios will be functions of the state vector based on the initial chemistry set $\overrightarrow{\Gamma^0} = \left\{T_g, p, V, \vec{n}_q, \vec{n}_u, t, T_e, \frac{E}{N}, \dots\right\}$ (with $\vec{n}_u$ being the concentrations of the subgroup of species that are not interested by the lumping procedure) as the species in the lumping group only exist in such space. On the contrary, during their usage in equations 5.13 and 5.15, such ratios determination must rely on the lumped chemistry set state vector $\left(\overrightarrow{\Gamma^L} = \left\{T_g, p, V, \vec{n}_{L_\gamma}, \vec{n}_u, t, T_e, \frac{E}{N}, \dots\right\}\right)$ only.

For example, the rate constants defined in equation 5.15 must be quantifiable based just on the plasma state to be used in a simulation. Such plasma state can only extend to the variables known at the time of the simulation. This implies that the D_{i,L_γ} ratios must be dependent on the state vector based on the lumped reaction set.

The D_{i,L_γ} requirement of bridging the initial and lumped chemistry sets domains leads to the conclusion that only the common terms of both state vectors can ever determine the values of the ratios $\left(\overrightarrow{\Gamma^0} \cap \overrightarrow{\Gamma^L} = \left\{T_g, p, V, \vec{n}_u, t, T_e, \frac{E}{N}, \dots\right\}\right)$. Furthermore, for the rate constants introduced in equation 5.15 to be properly defined, the D_{i,L_γ} functions should be independent also of time and of the common species densities, allowing only for the gas and electrons kinetic parameters to be used as arguments. On the other hand, equation 5.13 would need the species-to-lump ratios to be dependent on the gas temperature only, but this aspect will prove to be too limiting, thus requiring the expression in 5.13 to be revised.

Using equation 5.12, the D_{i,L_γ} ratios can be used to express the mole balance of a generic species i in the $\hat{L}_\gamma$ lumping group in terms of the total lump representative species mole balance:

$$\frac{dn_i}{dt} = D_{i,L_\gamma} \frac{dn_{L_\gamma}}{dt}$$

which, from equation 5.14*b* can lead to a definition of the species-to-lump ratio in terms of the system's chemical kinetics:

$$D_{i,L_\gamma} = \frac{\sum_{j=1}^{R} \nu_{i,j}^{n} \left(k_j^f \prod_z n_z^{\nu_{z,j}^f} - k_j^r \prod_z n_z^{\nu_{z,j}^r} \right)}{\sum_{q \in \hat{L}_\gamma} \sum_{j=1}^{R} \nu_{q,j}^{n} \left(k_j^f \prod_z n_z^{\nu_{z,j}^f} - k_j^r \prod_z n_z^{\nu_{z,j}^r} \right)} \tag{5.16}$$

The expression in equation 5.16 is formally dependent on the whole $\overrightarrow{\Gamma^0}$ state vector. To formulate an approach to determine the D_{i,L_γ} dependencies on the plasma kinetic parameters only, a more detailed investigation of the single terms' dependencies must be performed. Starting with the n_z species concentrations, these are direct variables of the $\overrightarrow{\Gamma^0}$ state vector whose dependency should be removed in the D_{i,L_γ} expression. For what concern the k_j^f and k_j^r rate constants, these are functions of the gas thermodynamic state, which can be expressed in terms of the gas temperature (T_g) (with the addition of the gas pressure p in case falloff-reactions are considered in the chemistry set), and of the electrons kinetics. In general, the latter can be uniquely determined from the electronic excitation, expressed in terms of the reduced electric field $\left(\frac{E}{N}\right)$, and from the electron collision cross sections, weighted by the molar composition of the heavy particles. Thus, summarizing, the D_{i,L_γ} expression in equation 5.16 can be interpreted as a function of the gas temperature (T_g), the gas pressure (p), the reduced electric field $\left(\frac{E}{N}\right)$, the electron collision cross sections (σ_j), and of the species concentrations (n_z).

As mentioned earlier, the dependence on species concentrations is undesirable in the species-to-lump ratios, as it would render the definition of the reaction rate constants in equation 5.15 improper. For this reason, an approximation is introduced in the D_{i,L_γ} computations to remove the n_z dependency. Focusing on the explicit dependence on species concentrations, this can be removed by performing a random sampling of the system molar composition according to an arbitrary distribution and by averaging the effects of multiple samples on the D_{i,L_γ} ratio. For simplicity, assuming that no species is more relevant than the others (*i.e.,* considering a uniform distribution) and sampling over a sufficiently large number of cases, the concentrations of the individual species become:

$$n_z = \frac{1}{S} \frac{p}{RT_g}$$

where S is the total number of species and R is the ideal gas constant.

A different assumption is instead used for the implicit dependence on the species concentrations involved in the electron collision cross sections weighting. In this case, the molar composition is assumed to be equal to the most probable gas composition to be found in the simulations (*i.e.,* an average composition weighted on the complete chemistry set simulations).

Under these approximations, one can define a parameter space spanned by the gas temperature, gas pressure and the reduced electric field (Ω_{T_g}, Ω_p and $\Omega_{\frac{E}{N}}$ respectively), and compute the D_{i,L_γ} value at each point within this space.

5.5.1.3 A directed graph approach for the ratios' computations

Some additional considerations on the determination of the D_{i,L_γ} ratios deserve to be addressed. The main aspect not yet clarified concerns which reactions should be considered when evaluating these functions, thereby enabling their explicit and operational definition. For this purpose, it is useful to refer to equation 5.15. By defining the forward and backward rate constants separately (for example, through the principle of detailed balancing), in a generic $\widetilde{k_j}$ the influence of the D_{i,L_γ} ratios will be exerted only on those reactions (rendered irreversible in this case) in which the species belonging to the lumped group appear as reactants. In this sense, it is convenient to represent the lumping process using directed graphs (figures 3.4 and 3.5). In these graphs, the nodes represent chemical species, and the edges represent the overlap of reactions that consume the tail species to produce the head species (note: unlike the directed graphs used in the DRGEP strategies discussed in earlier sections, in this case the edge lengths are arbitrary). In figure 3.4, nodes with solid outlines represent species not belonging to any lumping group, while nodes with dashed circles and a central cross denote species included in the lumping group (a single group in this example). As for the edges, the interface mechanisms between the lumping group and the remaining species are highlighted. Dashed edges represent mechanisms in which lumped species act as reactants, whereas dash–dot edges indicate mechanisms leading to the production of these species.

The lumping procedure will produce a similar directed graphs where all the species in the lumping group are replaced by a single representative under the constrain of establishing new connections (*i.e.,* the lumped reactions) having the same type (production or consumption type) of the ones existing in the original chemistry set with the species outside of the lumping manifold (figure 3.5). Moreover, these new connections have to ensure that the moles produced or consumed by their constitutive reactions are matching between the two sets.

In this regard, the condition on the production of the lumped representative species (*i.e.,* the sum of all species within the lumped group) is independent of the accuracy in evaluating the D_{i,L_γ}. Conversely, only the consumption of this species is dependent and affects the assessment of the species-to-lump ratios. Indeed, the D_{i,L_γ} represents the fraction of the total molar consumption of all species in the lumped group (which, to satisfy equation. 5.14a, remains invariant during the lumping process) that is attributable to the i-th species.

For these reasons, the calculation of the D_{i,L_γ} can be carried out at each point of the domain $\Omega_{T_g} \cup \Omega_p \cup \Omega_{\frac{E}{N}}$ based on the graph introduced here, as follows:

$$D_{i,L_\gamma} = \frac{\sum_{j=1}^{R_c} \nu_{q,j}^n k_j^f \prod_z \left(\frac{1}{S}\frac{p}{RT_g}\right)^{\nu_{z,j}^f}}{\sum_{q\in\hat{L}_\gamma}\sum_{j=1}^{R_c} \nu_{q,j}^n k_j^f \prod_z \left(\frac{1}{S}\frac{p}{RT_g}\right)^{\nu_{z,j}^f}} \tag{5.17}$$

where R_c has been introduced to refer to the reaction' subset involving the consumption mechanisms of the $\hat{L}_\gamma$ lumping group.

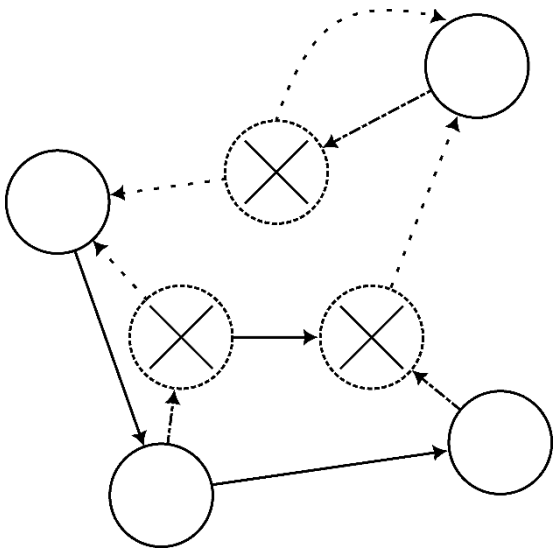

Figure 5.5.1 Directed relation graph representative of the reaction set before the lumping procedure.

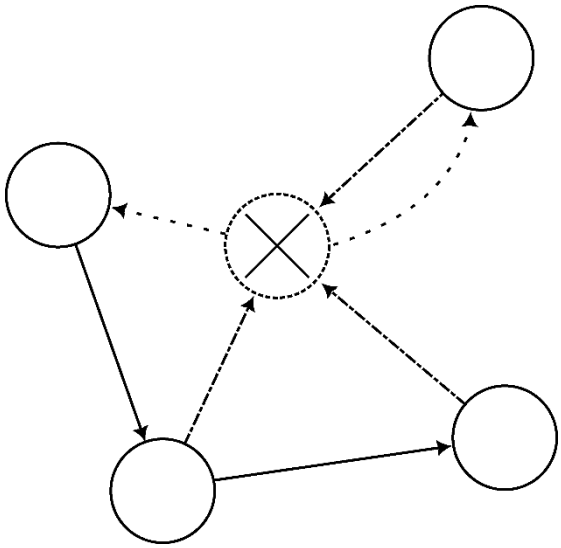

Figure 5.5.2 Directed relation graph representative of the reaction set after the lumping procedure.

5.5.1.4 Lumped thermodynamic properties and cross-sections

As mentioned in Section 5.5.1.2, equation 5.13 presents some critical issues when the definition of the D_{i,L_γ} ratio in equation 5.17 is employed. Specifically, thermodynamic properties must be defined as functions uniquely determined by the gas temperature (T_g). For this reason, equation 5.13 is revised to account for the dimensional discrepancy between the domains of the two functions as follows:

$$y_{L_\gamma}(T_g) = \sum_{q \in \hat{L}_\gamma} \frac{1}{\Delta_{\frac{E}{N}} \Delta_p} \int_{\Omega_p} \left[\int_{\Omega_{\frac{E}{N}}} D_{q,L_\gamma}\left(T_g, p, \frac{E}{N}\right) \cdot y_q(T_g) d\frac{E}{N} \right] dp \qquad (5.18)$$

where $\Delta_{\frac{E}{N}}$ and Δ_p are respectively the $\Omega_{\frac{E}{N}}$ and Ω_p extensions. In summary, given the domain of the D_{i,L_γ} functions - linked to the variables involved in determining the reaction rate constants - the calculation of thermodynamic properties requires averaging the effects of the D_{i,L_γ} ratio over the reduced electric field and pressure domains.

A second aspect worth emphasizing, which is particularly relevant to plasma chemistry, concerns the determination of cross sections for electron–collision processes. From equation 5.15, the reaction rate constants of these processes can be obtained; however, in order to keep the chemical kinetics consistently coupled with the electrons Boltzmann equation (EBE), it is necessary to derive electron cross sections to be used as input for the Boltzmann solver.

From the equation 5.15, when considering a rate constant deriving from an electron collision cross section, it is possible to derive the following expressions (see Section 5.9.2):

$$\widetilde{k_j} = \sqrt{\frac{2e}{m_e}} \int \varepsilon F_0 \left[\sum_{\eta \in R:\eta \sim j} \sigma_\eta(\varepsilon) \prod_{\hat{L}_\gamma \in \Lambda} \prod_{q \in \hat{L}_\gamma} D_{q,L_\gamma}^{\nu_{q,\eta}^f} \right] d\varepsilon \tag{5.19}$$

where e is the elementary charge, m_e is the electron mass, ε is the colliding electron kinetic energy, F_0 is the electron energy distribution function (EEDF), and $\sigma_\eta(\varepsilon)$ is the η-th process cross section. In equation 5.19 is implicitly provided also the lumped cross section $\left(\widetilde{\sigma_j}'\right)$ definition as:

$$\widetilde{\sigma_j}'\left(\varepsilon, \frac{E}{N}, T_g, p\right) = \sum_{\eta \in R:\eta \sim j} \sigma_\eta(\varepsilon) \prod_{\hat{L}_\gamma \in \Lambda} \prod_{q \in \hat{L}_\gamma} D_{q,L_\gamma}^{\nu_{q,\eta}^f}$$

This definition shares the same issues as the definition of lumped thermodynamic properties in equation 5.13. Indeed, in this case as well, it is necessary to average the effects provided by the D_{i,L_γ} ratio on the lumped cross section to obtain the following expression:

$$\widetilde{\sigma_j}(\varepsilon) = \frac{1}{\Delta_{\frac{E}{N}} \Delta_p \Delta_{T_g}} \int_{\Omega_{T_g}} \int_{\Omega_p} \int_{\Omega_{\frac{E}{N}}} \widetilde{\sigma_j}'\left(\varepsilon, \frac{E}{N}, T_g, p\right) d\frac{E}{N}\, dp\, dT_g \tag{5.20}$$

where Δ_{T_g} is the Ω_{T_g} space extension.

5.5.1.5 Induced error evaluation

Similarly to the techniques described previously, given the assumptions and approximations introduced so far, it is reasonable to expect that lumping induces errors in the simulations of the cases of interest (which are here implicitly contained within the extensions $\Delta_{\frac{E}{N}}$, Δ_p, and Δ_{T_g}). It is therefore important to keep track of the error introduced in the calculation of chemical species due to the reduction. This can be done as follows:

$$\xi_i = \max_{t,\kappa} \left| \frac{n_i^{(\kappa)}(t) - n_{0,i}^{(\kappa)}(t)}{n_{0,i}^{(\kappa)}(t)} \right| \tag{5.21}$$

where $n_i^{(\kappa)}(t)$ represents the concentration of the i-th species at time t for case κ calculated using the lumped chemistry set and $n_{0,i}^{(\kappa)}(t)$ represents the concentration

of the i-th species at time t for case κ calculated using the original (non-lumped) one.

Finally, the overall discrepancy between the reduced and complete set can be defined as:

$$\Xi = \max_{i} \xi_i \tag{5.22}$$

5.5.1.6 Pseudocode algorithm summary

The following pseudocode is provided to summarize the algorithm structure.

A. Species-to-lump ratios identification

Inputs: Chemistry set

Algorithm:

a. *Identify the lumping groups based on some similarity condition between species*

b. *Build the directed graph for the species-to-lump ratios computation*

c. *For each lumping group, compute the species-to-lump ratio for each species (i) in the lumping group for each point in the* $T_g, p, \frac{E}{N}$ *domain:*

$$D_{i,L_\gamma} = \frac{\sum_{j=1}^{R_c} \nu_{q,j}^{n} k_j^f \prod_z \left(\frac{1}{S}\frac{p}{RT_g}\right)^{\nu_{z,j}^f}}{\sum_{q\in\hat{L}_\gamma}\sum_{j=1}^{R_c} \nu_{q,j}^{n} k_j^f \prod_z \left(\frac{1}{S}\frac{p}{RT_g}\right)^{\nu_{z,j}^f}}$$

Outputs: Species-to-lump ratios functions

B. Lump representatives' characterization

Inputs: Species to lump ratios, Original chemistry set

Algorithm:

a. For each lumping group, create a lump representative species

i. Compute the lumped thermodynamic properties and cross sections

ii. Compute the lumped reactions cross sections

iii. Substitute the lump representatives in the chemistry set

Outputs: Reduced chemistry set

C. Induced error evaluation & convergence

Inputs: Reduced chemistry set, list of simulations, list of target species

Algorithm:

a. For each case (κ) in the list of simulations, simulate the reduced chemistry set.

b. Evaluate $\xi_{T_i} = \max_{t,\kappa} \left| \frac{n_{T_i}^{(\kappa)}(t) - n_{0,T_i}^{(\kappa)}(t)}{n_{0,T_i}^{(\kappa)}(t)} \right|$ *for each target species (T_i)*

c. Evaluate $\Xi = \max_{T_i} \xi_{T_i}$

Outputs: Reduced chemistry set

5.6 SPPARK's ARC Module

In this thesis work, the techniques described so far have been coupled with SPPARK through a module dedicated to ARC. Within this module, the reduction techniques are not only available individually but also combined into a more complex algorithm that orchestrates their interfacing, similarly to what has been presented in ARCANE [11]. This section describes the reduction algorithm implemented in SPPARK, focusing on the user-defined inputs and on the logic governing the coupling among the individual ARC techniques.

The algorithm is composed of three major subroutines. Firstly, a chemistry set is provided as the original chemistry set to be reduced together with a list of cases of interest (hereafter referred to as canonical cases). In this phase, the complete chemistry set is simulated on all the canonical cases identified by the user. Secondly, a skeletal reduction step takes place by combining in a loop both the species and reactions-oriented DRGEP algorithms. Thirdly, the chemistry lumping technique takes place. Optionally a second step of the DRGEP skeletal reduction loop can be applied if the chemistry lumping was successfully executed and the reaction set needs (and accepts) further reductions.

5.6.1 Canonical cases simulation

As mentioned earlier, the first step in the ARC algorithm consists in simulating the original chemistry set over the entire set of canonical cases. The procedure has been parallelized across multiple processors to optimize the computational time. In this context, the user provides the full chemistry set along with the set of conditions (both initial and forcing) required to define the problem. Since these conditions remain invariant with respect to the reduction, the same methodology is applied to the simulation of the reduced reaction sets and to the assessment of the error induced by each reduction step.

5.6.2 DRGEP Loop

The first actual reduction step couples the skeletal reduction loops through a species- and reaction-oriented DRGEP (hereinafter referred to as the DRGEP loop). As discussed earlier, the species-oriented technique allows more precise control over the focus of the reaction scheme on the phenomena of interest compared to the reaction-oriented algorithm, which, on the other hand, benefits from operating on a chemistry set that has been previously specialized. For these reasons, the first reduction step in the DRGEP loop employs the species-oriented technique (which carries out the bulk of the reduction work on secondary phenomena) and then further reduces the chemistry set using the reaction-

oriented technique (which, in this sense, performs a fine-tuning operation acting on the set's stiffness).

In addition to the internal loops within each technique, an external loop between the two techniques is also introduced. In this case, the exit conditions do not directly concern the error induced by the reduction, but rather the possibility of further reducing the reaction set. Accordingly, after the species-oriented DRGEP, a check is performed on the number of reactions in the sets before and after the reduction step. Conversely, following the reaction-oriented DRGEP, the check is performed on the number of species before and after the reduction step. In other words, it is assumed that each algorithm has fully addressed its respective target component, and it is checked whether running the complementary algorithm is required. This coupling rationale has been graphically summarized in Figure 5.6.1.

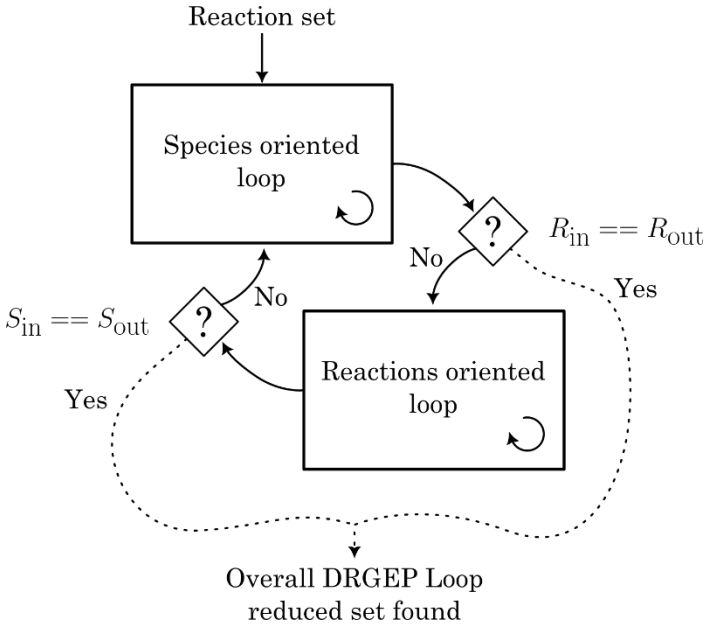

Figure 5.6.1 Graphical representation of the DRGEP loop.

Given the application of both species- and reaction-oriented algorithms within the DRGEP loop, some additional considerations on the convergence of the individual algorithms are required. The issue arises from the consecutive application of two algorithms with the same tolerance to the error induced by the reduction. Indeed, if the convergence condition were already satisfied after the first step, the second one could not take place. To address this, a two-threshold strategy (Tol_{min} and Tol_{max}) is adopted. The higher threshold, Tol_{max}, represents the tolerance actually desired by the user as the result of the DRGEP loop, while the lower one, Tol_{min} , acts as a barrier. Once Tol_{min} is exceeded, at each iteration the corresponding chemistry set is stored, so that, upon reaching Tol_{max}, a ranking of the candidate sets can be established based on the reduction-induced error, and the reaction set

with the smallest error can be selected as the final output (Figure 5.6.2). This final chemistry set can be provided to the following skeletal reduction step.

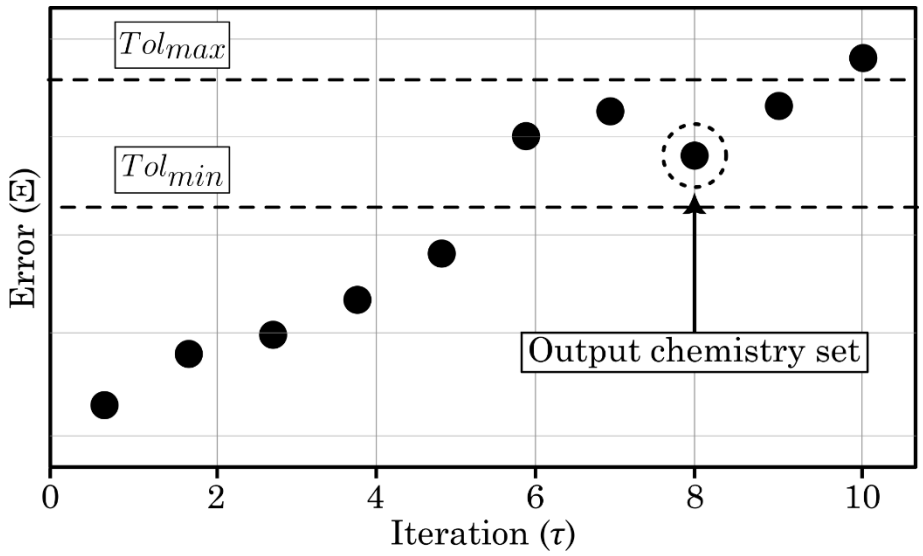

Figure 5.6.2 Single DRGEP technique convergence rationale in the DRGEP loop

5.6.3 Lumping step

The reduced chemistry set obtained from the DRGEP loop is then provided as input to the chemistry lumping step. In this context, lumping is carried out according to four possible grouping strategies:

1. Grouping all species that share the same chemical composition.

2. Grouping species that share both the same composition and the same type of excitation (electronic, vibrational, or rotational).

3. Grouping species that share the same composition and excitation type, and additionally exhibit similar excitation levels or modes (e.g., principal quantum numbers or vibrational modes; these sub-classifications must be user-defined).

4. Pairing species with the same composition based on their thermodynamic proximity.

Moreover, as in this algorithm the lumping technique acts on a skeletally reduced chemistry set, which is formally valid on the target species computations only, the lumping induced error evaluation is performed based on the same target species used in the DRGEP loop.

5.6.4 Algorithm's summary

In order to summarize the structure and functioning of the algorithm, this final section is included, with a particular focus on the required input quantities and the stages in which they are employed.

For the proper functioning of the algorithm, the following list of inputs must be defined:

1. Initial chemistry set ($R.S.^0$). This must include a sufficiently detailed description of thermodynamic properties and excitation characteristics for the species, as well as a complete specification of the reactions in terms of reaction equations and rate constants. Its primary use lies in the simulation of the canonical cases and in the very first iteration of the species-oriented DRGEP.

2. Set of canonical cases ($\overrightarrow{C.C.}$). A collection of simulation configurations defined in terms of initial conditions, forcing terms, and time domain of interest. These are employed throughout the entire process, both in the initial canonical simulations and in the evaluation of the errors induced by each reduction technique.

3. List of target species ($\vec{T}_i$). This set includes the species representative of the phenomena toward which the reduced reaction network is to be directed. They are used in the ranking process of the species-oriented DRGEP as well as in every stage of error evaluation.

4. List of immune species ($\vec{S}_i$). Not introduced until now, these are species that must be retained in the reaction scheme regardless of the reduction (e.g., reactants or selected excited states that should remain distinct from their lumped counterparts). They are enforced at all stages of reduction to ensure their inclusion in the reaction set.

5. Set of evaluation time instants ($\vec{t}$). Specific time points at which the error induced by the reduction is assessed. They are employed in every error evaluation step and during the directed graphs building steps for the skeletal techniques.

6. Minimum and maximum tolerance (Tol_{min} and Tol_{max}). Threshold values: once the minimum tolerance is reached, the skeletal chemistry sets produced are saved; once the maximum tolerance is reached, the skeletal reduction process is terminated.

7. Domains of E/N, pressure, and gas temperature ($\Delta_{\frac{E}{N}}$, Δ_p, and Δ_{T_g}). These are required for the construction of the lumped chemistry set.

To complete the summary of the algorithm, a graphical representation of its workflow and its coupling with the required inputs is provided in the Figure 5.6.3.

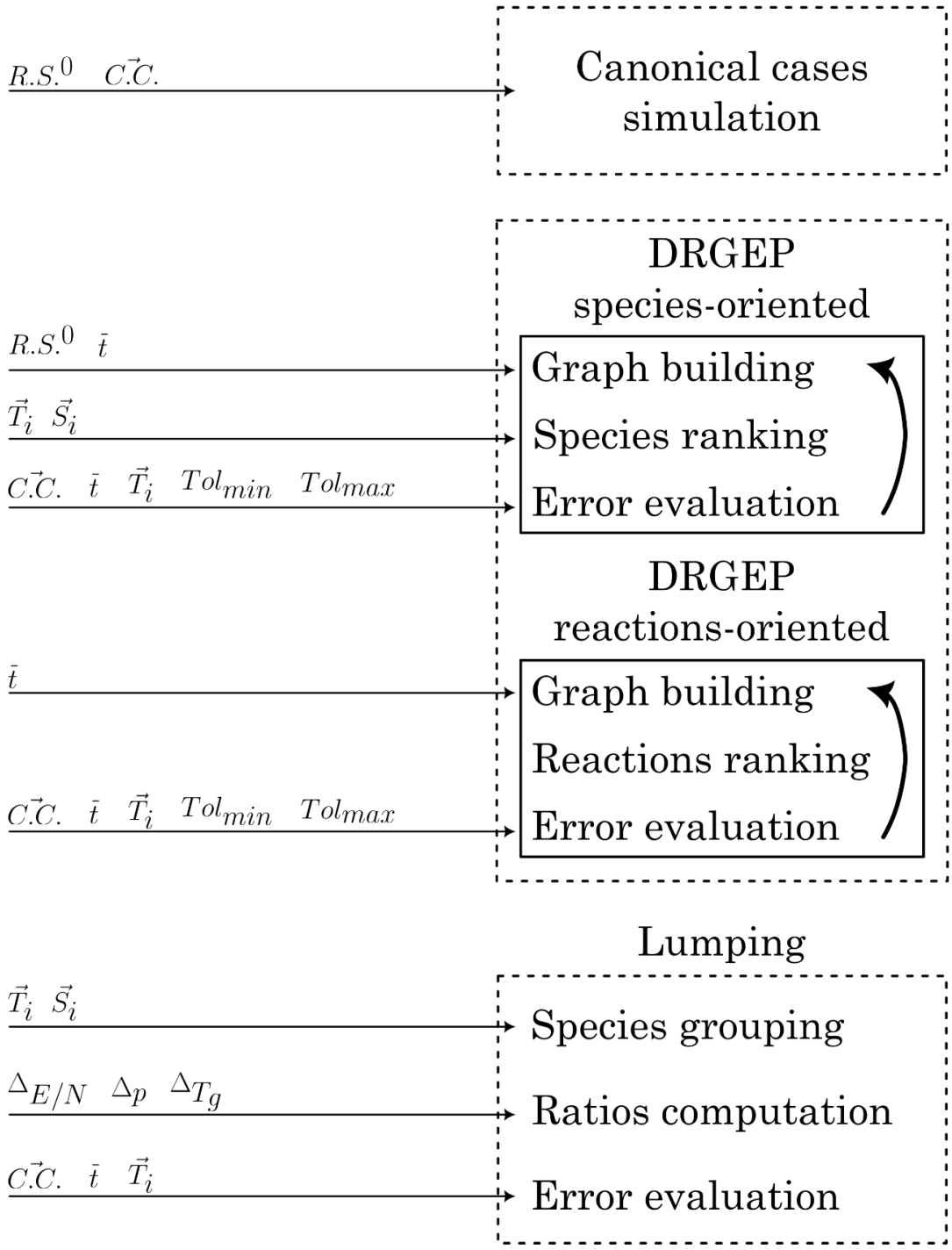

Figure 5.6.3 Reduction algorithm input scheme.

5.7 Applications

The technique described in Section 5.6 has been applied to two different chemistry sets; one referring to a humid air chemistry and the second referring to an Ar chemistry. In this section, the reduction results on such test cases will be shown and the reduction performance evaluated.

5.7.1 Humid air

The humid air case is based on the chemistry set published by Sakiyama *et al.* [13]. This reaction set is composed of 54 species, classifiable as shown in Table 5.7.1, and 623 reactions. The purpose of the reduction is to derive, from the full chemistry set, a reduced reaction scheme that accurately represents ozone production in an atmospheric-pressure plasma in humid air. Given the limited number of excited states (Table 5.7.1), the lumping step would provide negligible benefits; therefore, the algorithm is terminated at the DRGEP loop.

Type	**Species**
Ground	H, N, O, O_3, NO, N_2O, NO_2, NO_3, N_2O_3, N_2O_4, N_2O_5, H_2, OH, H_2O, H_2O_2, HNO, HNO_2, HNO_3, N_2, O_2, HO_2
Positively charged	N^+, N_2^+, N_3^+, N_4^+, O^+, O_2^+, O_4^+, NO^+, N_2O^+, NO_2^+, H^+, H_2^+, H_3^+, OH^+, H_2O^+, H_3O^+
Negatively charged	e, O^-, O_2^-, O_3^-, O_4^-, NO_2^-, N_2O^-, NO^-, NO_3^-, OH^-, H_2O^-,
Excited states	$N(\,^2D)$, $N_2(A^3\Sigma)$, $N_2(B^3\Pi)$, $O(\,^1D)$, $O_2(a^1\Delta)$

Table 5.7.1 Chemical species included in the Sakiyama *et. al.* [13] model.

5.7.1.1 Canonical case simulation

In this context, a single canonical case was studied having the conditions displayed in Table 5.7.2.

Condition	**Value**	**Condition**	**Value**
Gas temperature (T_g)	300 K (fixed)	Pressure (p)	1 atm
Power density $(\tilde{P})$	200 $\frac{W}{cm^3}$ (constant)	Plasma to total ratio (φ)	1
Relative humidity	60 %	Simulation time	2 ms

Table 5.7.2 Conditions defining the canonical case

In the canonical case simulation step, the full chemistry set is applied to a global model simulation of the canonical case. The estimated ozone concentration obtained through this simulation are shown in Figure 5.7.1.

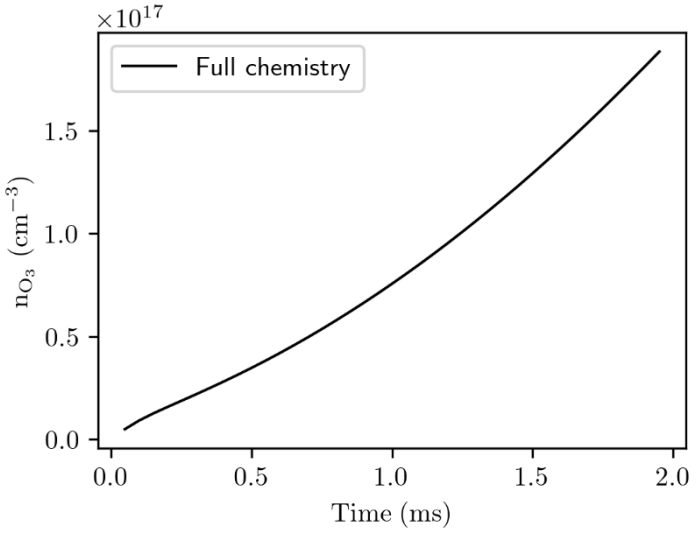

Figure 5.7.1 Full chemistry set ozone concentration estimation on the canonical case conditions.

5.7.1.2 DRGEP loop

The results produced by the full chemistry set simulation are then used in the DRGEP loop reduction step. In addition to the complete chemistry set and the

canonical case, this step requires a list of target and immune to the reduction species, a list of time samples and two tolerances to control the species- and reactions-oriented algorithms. These group of additional inputs are listed, for reference, in Table 5.7.3.

Parameter	**Value**	**Parameter**	**Value**
$\vec{T}_i$	O_3	$\vec{S}_i$	E, O_2, N_2 and H_2O
Tol_{min}	5%	Tol_{max}	10%
$\vec{t}$	15 equally spaced points		

Table 5.7.3 Additional inputs for the DRGEP loop.

Under these conditions, the DRGEP loop is executed registering a single global iteration. The species-oriented step performs 8 iterations, obtaining a reduced chemistry set characterized by 46 species and 527 reactions. After this step, three additional iterations of the reactions-oriented algorithm are executed leading to a reaction scheme including 46 species and 424 reactions. To illustrate the reduction quality, the canonical case simulations of the two (species-oriented and reactions-oriented) reactions sets compared against the original chemistry set results are shown in Figure 5.7.2.

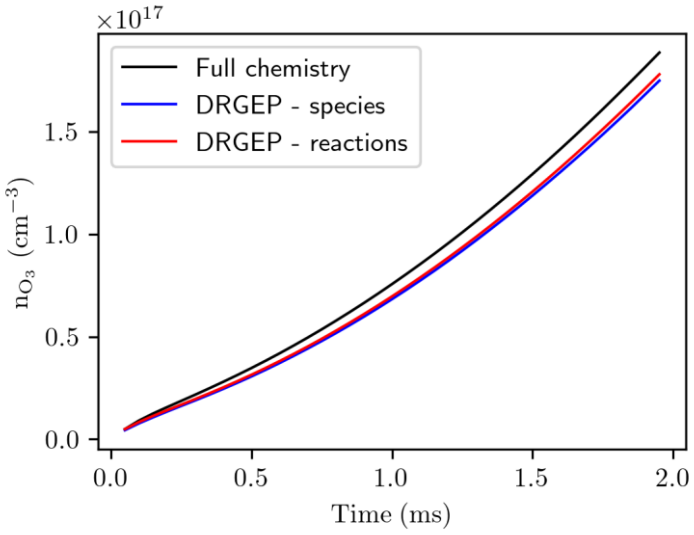

Figure 5.7.2 Reduced chemistry sets comparison against the original one on the canonical case conditions.

In addition to the temporal evolution of ozone concentration in the reaction volume, the bar plot in Figure 5.7.3 summarizes the reduction achieved through the application of the species- and reactions-oriented DRGEP techniques. As shown, the species-oriented DRGEP reduction step induces an error of $\Xi \approx 7.254\%$ whilst the error decreases at the subsequent application of the reactions-oriented DRGEP with a value of $\Xi \approx 5.629\%$, in all probability due to error cancellation effects.

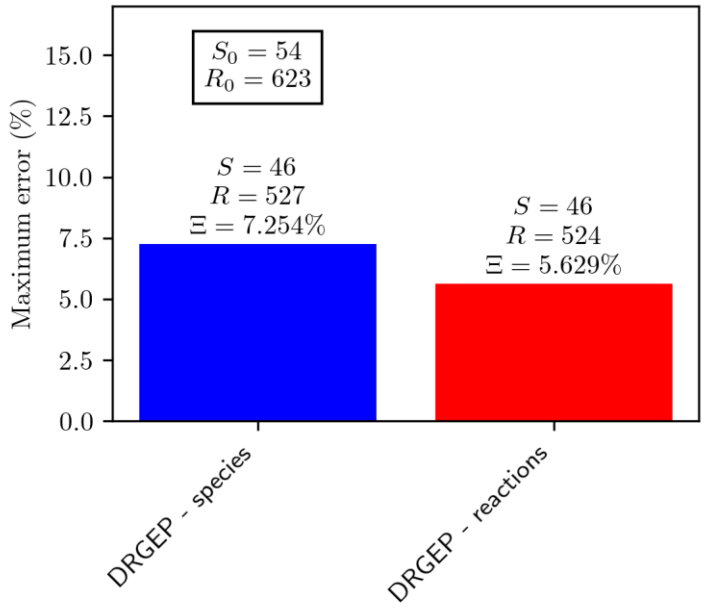

Figure 5.7.3 Summary of the DRGEP techniques' performances with respect to the original chemistry set

In conclusion, after the overall reduction step, the computational cost associated with the number of continuity equations in the model (*i.e.,* the number of species) decreases of 14.81% with respect to the original chemistry set.

5.7.2 Ar chemistry

The Ar chemistry case is built on an extended version of the chemistry set published by Stankov *et al.* [14]. In fact, the original 23 species have been extended to 39 by explicitly accounting for the excited levels higher than the 2p levels that in the Stankov chemistry set were compressed in the $Ar^*(hl)$ species as shown in Table 5.7.4. In the extended chemistry set, the 39 species interact with each other through 919 reactions (498 electron collisions, 64 non-equilibrium, 354 thermochemical and 5 surface reactions). In this case, due to the large number of excited states, the chemical lumping is likewise carried out after the DRGEP loop, with the objective of obtaining a reduced set capable of representing the ionization process in a low-pressure Ar plasma.

Type	**Species**
Ground	$Ar(\,^1p_0)$
Positively charged	Ar^+, Ar_2^+
Negatively charged	e
Excited states	$Ar(\,^1s_5)$, $Ar(\,^1s_4)$, $Ar(\,^1s_3)$, $Ar(\,^1s_2)$, $Ar(\,^2p_1)$, $Ar(\,^2p_2)$, $Ar(\,^2p_3)$, $Ar(\,^2p_4)$, $Ar(\,^2p_5)$, $Ar(\,^2p_6)$, $Ar(\,^2p_7)$, $Ar(\,^2p_8)$, $Ar(\,^2p_9)$, $Ar(\,^2p_{10})$, $Ar(\,^2s_2)$, $Ar(\,^2s_3)$, $Ar(\,^2s_4)$, $Ar(\,^2s_5)$, $Ar(\,^3d_1')$, $Ar(\,^3d_1'')$, $Ar(\,^3d_2)$, $Ar(\,^3d_3)$, $Ar(\,^3d_4)$, $Ar(\,^3d_4')$, $Ar(\,^3d_5)$, $Ar(\,^3d_6)$, $Ar(\,^3s_1')$, $Ar(\,^3s_1'')$, $Ar(\,^3s_1''')$, $Ar(\,^3s_1'''')$, $Ar_2^*(\,^3\Sigma_u^+, v=0)$, $Ar_2^*(\,^1\Sigma_u^+, v=0)$, $Ar_2^*(\,^3\Sigma_u^+, v\gg 0)$, $Ar_2^*(\,^1\Sigma_u^+, v\gg 0)$
Photons	$h\nu$

Table 5.7.4 Species included in the extended Stankov *et al.* [14] Ar reaction set.

5.7.2.1 Canonical cases simulation

In this case as well, a single canonical case is employed to investigate the phenomenon of interest. A gas consisting of 100% $Ar(\,^1p_0)$ at a temperature of $273.15\,K$ and a pressure of $1\,Torr$ is confined inside a cylindrical reactor with a radius of $1.5\,cm$ and a length of $1\,cm$. It is assumed that a constant power density of $110\,\frac{W}{m^3}$ is deposited throughout the entire volume, coupling entirely with the plasma phase, which occupies 25% of the reactor. Two circular electrodes are also considered in the simulation, featuring the cathode ions recombinations with or without secondary electrons emissions (with a coefficient of 0.07) and the anode electrons capture. Both rates are identified by means of an ambipolar diffusion rate [15]. The ionization process is simulated for $30\,\mu s$ (sufficient for the ionization to reach its steady state). All the conditions defining the canonical case have been summarized in Table 5.7.5.

Condition	**Value**	**Condition**	**Value**
Gas temperature (T_g)	273.15 K (fixed)	Pressure (p)	1 Torr
$Ar(\ ^1p_0)$ initial molar fraction	1	Reactor's radius	1.5 cm
Reactor's length	1 cm	Power density $(\tilde{P})$	110 $\frac{W}{m^3}$ (constant)
Plasma to total ratio (φ)	0.25	Secondary emission coefficient	0.07
Simulation time	30 μs		

Table 5.7.5 Canonical case's parameters

The complete chemistry set, simulated in a global model under these conditions, produced the following results (Figure 5.7.4) for the Ar^+ concentration in the plasma phase.

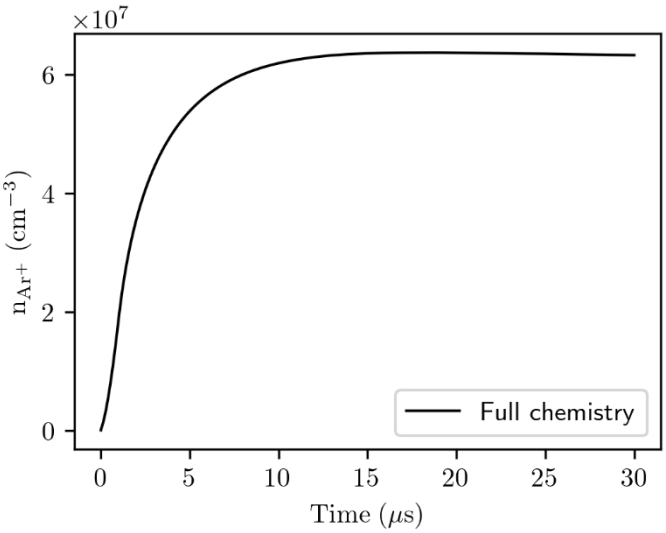

Figure 5.7.4 Full chemistry canonical simulation results for the Ar^+ concentration.

5.7.2.2 DRGEP loop

The DRGEP loop is set in this case with high constraints for the error induced by the skeletal reduction. In fact, a minimum tolerance of 0.1 % and a maximum one of 1 % are adopted. This choice reflects the possibility of application of the lumping technique that loosens the need of a strong skeletal reduction to reduce the overall chemical complexity. For completeness, the detailed DRGEP loop parameters are summarized in Table 5.7.6.

Parameter	**Value**	**Parameter**	**Value**
$\vec{T}_i$	Ar^+	$\vec{S}_i$	e and $Ar(\,^1p_0)$
Tol_{min}	0.1 %	Tol_{max}	1 %
$\vec{t}$	15 equally spaced points		

Table 5.7.6 DRGEP loop input parameters

Under these conditions, in the DRGEP loop both the species- and reactions-oriented algorithms are executed once. The species-oriented technique performs 5 loops, reducing the species from 39 to 34 (the $Ar_2^*(\,^3\Sigma_u^+, v=0)$, $Ar_2^*(\,^1\Sigma_u^+, v=0)$, $Ar_2^*(\,^3\Sigma_u^+, v\gg 0)$, $Ar_2^*(\,^1\Sigma_u^+, v\gg 0)$, and hv species are removed) and the reactions from 919 to 608. The subsequent reactions-oriented step further reduces the reactions to 575 reactions. The two techniques register an induced error Ξ of 0.175 % and 0.146 % respectively. The canonical case's simulation results of the two reduced chemistry sets are shown in Figure 5.7.5. Furthermore, a reduction performance summary is shown in Figure 5.7.6.

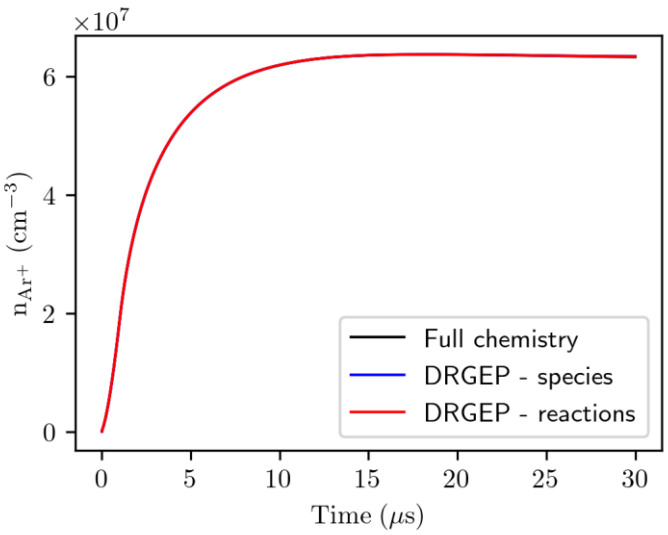

Figure 5.7.5 Reduced chemistry sets to full chemistry comparison on the canonical case. The three lines are overlapping

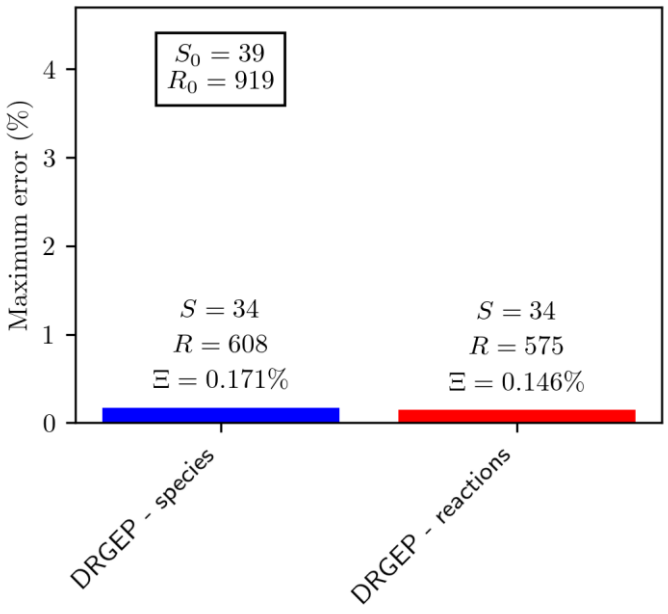

Figure 5.7.6 Summary of the reduction performance.

5.7.2.3 Chemistry lumping

The chemistry set produced by the DRGEP loop is then provided to the lumping technique. As in the reaction set no falloff reactions are included, only two additional parameters have to be supplied. The gas temperature domain is defined by means of a three point linearly spaced one with minimum value of 273.14 K and a maximum value of 273.16 K. Doing so, the lumped chemistry set will be valid in the considered canonical case (constant temperature of 273.15 K). On the other hand, the reduced electric field domain is introduced through an exponentially

spaced domain of 15 points from $0.1\,Td$ to $5000\,Td$. Furthermore, all the excited states present in the chemistry set are grouped together under the same lump representative species.

The lumping step leads to a chemistry set composed of just 5 species and 9 reactions inducing an error with respect to the complete one of 3.266 % in the computation of the target species. The canonical case's simulation results of all reduced chemistry sets are shown in Figure 5.7.7. Furthermore, an overall reduction performance summary is shown in Figure 5.7.8.

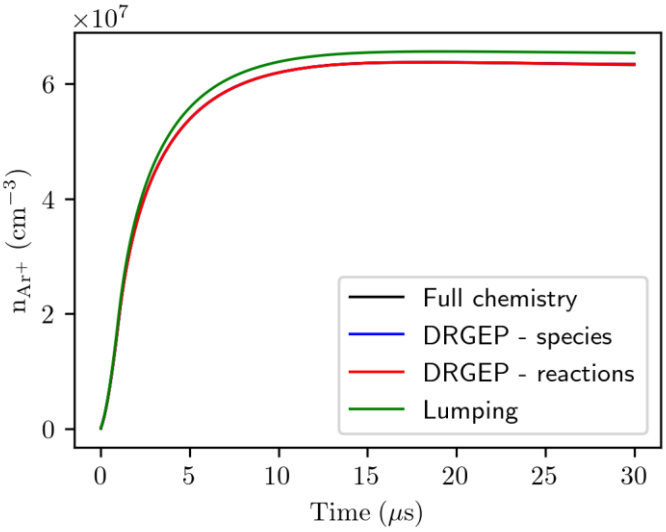

Figure 5.7.7 Reduced sets against full chemistry comparison on the canonical case.

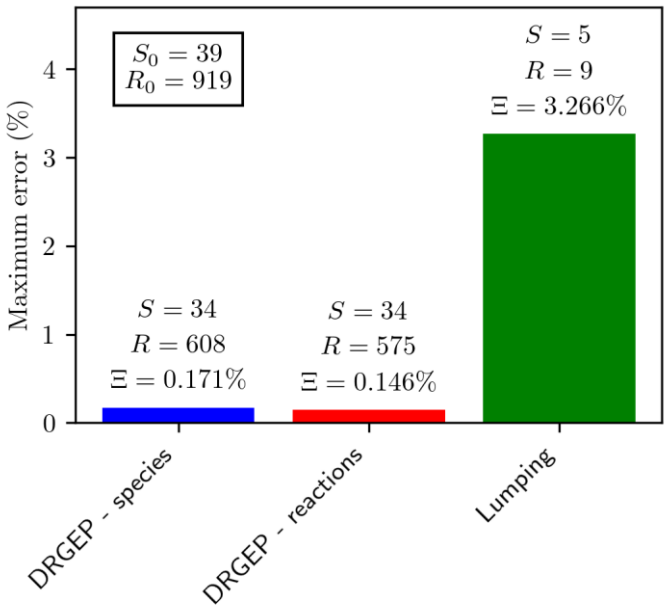

Figure 5.7.8 Reductions' performances summary

In conclusion, after the overall reduction step, the computational cost associated with the number of continuity equations in the model decreases of 87.18% with respect to the complete chemistry set.

5.8 Conclusions

The reduction of the computational cost associated with chemical complexity is a particularly relevant issue in plasma modeling for chemical applications. This becomes even more crucial when the systems under investigation feature geometrical complexities that require the use of spatially resolved models, such as fluid models. In this context, one of the key challenges is the development of automatic and reproducible strategies for chemical mechanism reduction. Such strategies enable the scaling of numerical modeling from simple global models to more complex descriptions without relying on prior theoretical knowledge of the reaction pathways, thereby creating an automated pipeline for the geometric scale-up of plasma simulations.

One possible approach is the application of ARC techniques to plasma chemistry. Since these methods originate from combustion modeling, specific adaptations are often required to make them suitable for plasma applications. In this chapter, the reduction strategy developed during the PhD has been presented. The approach combines skeletal reduction techniques (species- and reactions-oriented DRGEP) with a novel chemical lumping method, in order to automatically reduce a given input mechanism while preserving the ability to represent a selected subset of relevant phenomena.

Two case studies have been introduced. The first chemistry set, describing an atmospheric plasma in humid air, was reduced through skeletal techniques alone to represent ozone production. In this case, the computational cost associated with the number of species was decreased by 14.81%, with an induced error of 5.629% in the predicted ozone concentration. The second chemistry set, representing an Ar plasma at low pressure, was reduced to capture the ionization dynamics of Ar. Here, the use of both skeletal reduction and chemical lumping enabled the construction of a highly compact mechanism, leading to an 87.18% decrease in computational cost while keeping the overall induced error at 3.266%.

Future work should focus on extending the reduction framework by incorporating time-scale analysis techniques, which are expected to further enhance the efficiency of plasma chemistry simulations in multidimensional configurations. For example, partial equilibrium and quasi-steady-state approximations could be

adapted to plasma chemistry applications, allowing reaction subsets stiffness to be reduced.

5.9 Appendix

For completeness and reference purposes, this appendix section provides detailed derivations for the key expressions presented in Chapter 5.

5.9.1 Lumped reactions coefficients derivation

Equation (5.14a) expresses the net production of a lumped representative species (L_γ) as the sum of the net productions of the species in the lumping group $(\hat{L}_\gamma)$:

$$\frac{dn_{L_\gamma}}{dt} = \sum_{q \in \hat{L}_\gamma} \frac{dn_q}{dt} \tag{5.14a}$$

The net production of the q-th species in the lumping group can be expressed in terms of the elementary reactions:

$$\frac{dn_q}{dt} = \sum_{j=1}^{R} \nu_{q,j}^{n} \left(k_j^f \prod_{z=1}^{S} n_z^{\nu_{z,j}^f} - k_j^r \prod_{z=1}^{S} n_z^{\nu_{z,j}^r} \right)$$

which, when substituted in equation (5.14a), yields:

$$\frac{dn_{L_\gamma}}{dt} = \sum_{q \in \hat{L}_\gamma} \sum_{j=1}^{R} \nu_{q,j}^{n} \left(k_j^f \prod_{z=1}^{S} n_z^{\nu_{z,j}^f} - k_j^r \prod_{z=1}^{S} n_z^{\nu_{z,j}^r} \right) \tag{5.14b}$$

Equation (5.14b) is defined in the original chemistry set domain, as it depends on the $\overrightarrow{\Gamma^0}$ state vector (see Section 5.5.1.2). Since the net production rate of lumped species must preserved during the lumping procedure, an equivalent expression for equation (5.14b) to be evaluated using the $\overrightarrow{\Gamma^L}$ state vector (Section 5.5.1.2) must exist:

$$\frac{dn_{L_\gamma}}{dt} = \sum_{j=1}^{R_L} \nu_{L_\gamma,j}^{n} \left(\tilde{k}_j^f \prod_{z=1}^{S_L} n_z^{\nu_{z,j}^f} - \tilde{k}_j^r \prod_{z=1}^{S_L} n_z^{\nu_{z,j}^r} \right)$$

where S_L and R_L denote, respectively, the number of species and reactions in the lumped chemistry set, and $\tilde{k}_j^f$ and $\tilde{k}_j^r$ are the forward and reverse reaction rate constants in the lumped chemistry set.

Equating the net production rates before and after lumping leads to:

$$\sum_{q\in\hat{L}_\gamma}\sum_{j=1}^{R}\nu_{q,j}^{n}\left(k_j^f\prod_{z=1}^{S}n_z^{\nu_{z,j}^f}-k_j^r\prod_{z=1}^{S}n_z^{\nu_{z,j}^r}\right)=\sum_{j=1}^{R_L}\nu_{L_\gamma,j}^{n}\left(\tilde{k}_j^f\prod_{z=1}^{S_L}n_z^{\nu_{z,j}^f}-\tilde{k}_j^r\prod_{z=1}^{S_L}n_z^{\nu_{z,j}^r}\right)(A.5.1)$$

The left-hand-side of the expression can be reformulated as by introducing the species to lump ratios $(D_{h,L})$ for a set of multiple lumping groups (Λ), and defining:

$$\nu_{L_\gamma,j}^{n}=\sum\nolimits_{q\in\hat{L}_\gamma}\nu_{q,j}^{n}$$

The left-hand-side of $(A.5.1)$ can be rewritten as:

$$\sum_{q\in\hat{L}_\gamma}\sum_{j=1}^{R}\nu_{q,j}^{n}\left(k_j^f\prod_{z=1}^{S}n_z^{\nu_{z,j}^f}-k_j^r\prod_{z=1}^{S}n_z^{\nu_{z,j}^r}\right)=$$

$$=\sum_{q\in\hat{L}_\gamma}\sum_{j=1}^{R}\nu_{q,j}^{n}\left(k_j^f\prod_{z\notin\hat{L}\forall\hat{L}\in\Lambda}n_z^{\nu_{z,j}^f}\prod_{\hat{L}\in\Lambda}\prod_{h\in\hat{L}}n_h^{\nu_{h,j}^f}-k_j^r\prod_{z\notin\hat{L}\forall\hat{L}\in\Lambda}n_z^{\nu_{z,j}^r}\prod_{\hat{L}\in\Lambda}\prod_{h\in\hat{L}}n_h^{\nu_{h,j}^r}\right)$$

$$=\sum_{q\in\hat{L}_\gamma}\sum_{j=1}^{R}\nu_{q,j}^{n}\left(k_j^f\prod_{z\notin\hat{L}\forall\hat{L}\in\Lambda}n_z^{\nu_{z,j}^f}\prod_{\hat{L}\in\Lambda}\prod_{h\in\hat{L}}D_{h,L}^{\nu_{h,j}^f}n_L^{\nu_{h,j}^f}-k_j^r\prod_{z\notin\hat{L}\forall\hat{L}\in\Lambda}n_z^{\nu_{z,j}^r}\prod_{\hat{L}\in\Lambda}\prod_{h\in\hat{L}}D_{h,L}^{\nu_{h,j}^f}n_L^{\nu_{h,j}^f}\right)$$

$$=\sum_{j=1}^{R}\nu_{L_\gamma,j}^{n}\left(k_j^f\prod_{z\notin\hat{L}\forall\hat{L}\in\Lambda}n_z^{\nu_{z,j}^f}\prod_{\hat{L}\in\Lambda}\prod_{h\in\hat{L}}D_{h,L}^{\nu_{h,j}^f}n_L^{\nu_{h,j}^f}-k_j^r\prod_{z\notin\hat{L}\forall\hat{L}\in\Lambda}n_z^{\nu_{z,j}^r}\prod_{\hat{L}\in\Lambda}\prod_{h\in\hat{L}}D_{h,L}^{\nu_{h,j}^f}n_L^{\nu_{h,j}^f}\right)(A.5.2)$$

Here, $D_{h,L}$ denotes the species to lump ratio of the species h to its lumping group representative L, and Λ is the set of all lumping groups.

The number of reactions before and after lumping, R and R_L, generally differ. The original R reactions can be grouped in three different classes:

i. Reactions insensible to the lumping, which are not featuring any of the species in any of the lumping groups.

ii. Reactions to be lumped, consisting of "similar" reactions (Section 5.5.1.1) that can be grouped together under a single representative reaction.

iii. Reactions internal to a single lumping group, which are featuring only species belonging to the same lamping group.

In the lumping procedure, only the first two reactions classes are included in the R_L after-lumping reactions as the third one does not influence the overall lumped

representative net rate of production (*i.e.*, their net effect is zero). Moreover, the number of reactions of the second class is strongly reduced by the effect of the similar reactions grouping.

Accordingly with the classification, the right-hand-side of equation ($A.5.1$) and equation ($A.5.2$) can be decomposed as:

$$\sum_{j=1}^{R_L} \nu_{L_\gamma,j}^n \tilde{\omega}_j^n = \sum_{j\in NL} \nu_{L_\gamma,j}^n \omega_j^n + \sum_{j\in L'} \nu_{L_\gamma,j}^n \tilde{\omega}_j^n \qquad (A.5.1a)$$

$$\begin{aligned}\sum_{j=1}^{R} \nu_{L_\gamma,j}^n \omega_j^n &= \sum_{j\in NL} \nu_{L_\gamma,j}^n \omega_j^n + \sum_{j\in L} \nu_{L_\gamma,j}^n \omega_j^n + \sum_{j\in I} \nu_{L_\gamma,j}^n \omega_j^n \\ &= \sum_{j\in NL} \nu_{L_\gamma,j}^n \omega_j^n + \sum_{j\in L} \nu_{L_\gamma,j}^n \omega_j^n \qquad (A.5.2a)\end{aligned}$$

where ω_j^n denotes the net rate of the j-th reaction, and NL, I, L, and L' are, respectively, the reactions' classes of insensible to the lumping, internal to a single lumping group, to be lumped belonging to R and to be lumped belonging to R_L. From a comparison of equations ($A.5.1a$) and ($A.5.2a$) it can be remarked that the net rate of the j-th reaction remains unchanged during the lumping procedure for reactions in the NL group, whilst the L' group reactions are characterized by a lumped net rate $\tilde{\omega}_j^n$.

For this reason, the lumped rate constants can be obtained by the equality:

$$\sum_{j\in L'} \nu_{L_\gamma,j}^n \tilde{\omega}_j^n = \sum_{j\in L} \nu_{L_\gamma,j}^n \omega_j^n$$

Introducing now the concept of similar reactions (denoted by the ~ operator - Section 5.5.1.1), it is possible to group together similar reactions in L. By definition, similar reactions are characterized by the same net stoichiometric coefficient for every lumped representative.

$$\sum_{j\in L} \nu_{L_\gamma,j}^n \omega_j^n = \sum_{j\in L'} \nu_{L_\gamma,j}^n \left(\sum_{\eta\in L:\eta\sim j} \omega_\eta^n \right)$$

This last result leads to the equality:

$$\tilde{\omega}_j^n = \sum_{\eta\in L:\eta\sim j} \omega_\eta^n$$

which can be expressed in terms of the lumped reaction rate constants:

$$\tilde{k}_j^f \prod_{z=1}^{S_L} n_z^{\nu_{z,j}^f} - \tilde{k}_j^r \prod_{z=1}^{S_L} n_z^{\nu_{z,j}^r} = \sum_{\eta \in L:\eta \sim j} \omega_\eta^f - \sum_{\eta \in L:\eta \sim j} \omega_\eta^r$$

Separating the forward and reverse effects and rearranging terms, yields the expressions of forward and revers rate constants reported in equation (5.15):

$$\begin{aligned}
\tilde{k}_j^f \prod_{z=1}^{S_L} n_z^{\nu_{z,j}^f} &= \sum_{\eta \in L:\eta \sim j} k_j^f \prod_{z \notin \hat{L} \forall \hat{L} \in \Lambda} n_z^{\nu_{z,j}^f} \prod_{\hat{L} \in \Lambda} \prod_{h \in \hat{L}} D_{h,L}^{\nu_{h,j}^f} n_L^{\nu_{h,j}^f} \\
&= \sum_{\eta \in L:\eta \sim j} k_j^f \prod_{z \notin \hat{L} \forall \hat{L} \in \Lambda} n_z^{\nu_{z,j}^f} \prod_{\hat{L} \in \Lambda} n_L^{\sum_{h \in \hat{L}} \nu_{h,j}^f} \prod_{\hat{L} \in \Lambda} \prod_{h \in \hat{L}} D_{h,L}^{\nu_{h,j}^f} \\
&= \sum_{\eta \in L:\eta \sim j} k_j^f \prod_{z=1}^{S_L} n_z^{\nu_{z,j}^f} \prod_{\hat{L} \in \Lambda} \prod_{h \in \hat{L}} D_{h,L}^{\nu_{h,j}^f}
\end{aligned}$$

$$\begin{aligned}
\tilde{k}_j^r \prod_{z=1}^{S_L} n_z^{\nu_{z,j}^r} &= \sum_{\eta \in L:\eta \sim j} k_j^r \prod_{z \notin \hat{L} \forall \hat{L} \in \Lambda} n_z^{\nu_{z,j}^r} \prod_{\hat{L} \in \Lambda} \prod_{h \in \hat{L}} D_{h,L}^{\nu_{h,j}^r} n_L^{\nu_{h,j}^r} \\
&= \sum_{\eta \in L:\eta \sim j} k_j^r \prod_{z \notin \hat{L} \forall \hat{L} \in \Lambda} n_z^{\nu_{z,j}^r} \prod_{\hat{L} \in \Lambda} n_L^{\sum_{h \in \hat{L}} \nu_{h,j}^r} \prod_{\hat{L} \in \Lambda} \prod_{h \in \hat{L}} D_{h,L}^{\nu_{h,j}^r} \\
&= \sum_{\eta \in L:\eta \sim j} k_j^r \prod_{z=1}^{S_L} n_z^{\nu_{z,j}^r} \prod_{\hat{L} \in \Lambda} \prod_{h \in \hat{L}} D_{h,L}^{\nu_{h,j}^r}
\end{aligned}$$

$$\begin{cases}
\tilde{k}_j^f = \sum_{\eta \in L:\eta \sim j} \left(k_\eta^f \prod_{\hat{L} \in \Lambda} \prod_{h \in \hat{L}} D_{h,L}^{\nu_{h,j}^f} \right) \\
\tilde{k}_j^r = \sum_{\eta \in L:\eta \sim j} \left(k_\eta^r \prod_{\hat{L} \in \Lambda} \prod_{h \in \hat{L}} D_{h,L}^{\nu_{h,j}^r} \right)
\end{cases} \tag{5.15}$$

5.9.2 Lumped electron collision cross-sections derivation

Equation (5.15) provides the forward and reverse rate constants of the j-th lumped reaction in terms of the rate constants of reactions defined in the original chemistry set:

$$\begin{cases} \tilde{k}_j^f = \sum_{\eta \in R:\eta \sim j} \left(k_\eta^f \prod_{\hat{L}_\gamma \in \Lambda} \prod_{q \in \hat{L}_\gamma} D_{q,L_\gamma}^{\nu_{q,\eta}^f} \right) \\ \tilde{k}_j^r = \sum_{\eta \in R:\eta \sim j} \left(k_\eta^r \prod_{\hat{L}_\gamma \in \Lambda} \prod_{q \in \hat{L}_\gamma} D_{q,L_\gamma}^{\nu_{q,\eta}^r} \right) \end{cases} \tag{5.15}$$

Considering the j-th reaction rate constant in the lumped chemistry set, this is obtained by summing all the rate constants of the original chemistry set reactions similar to the j-th reaction, weighted by means of the species to lump ratios $\left(D_{q,L_\gamma}\right)$.

Since equation (5.15) was derived (Section 5.9.1) for an arbitrary reaction, it can be applied also to reaction rate constants deriving from electron collision cross sections. The rate constant for an electron collision can be expressed in terms of its cross section as follows:

$$k_\eta^f = \sqrt{\frac{2e}{m_e}} \int \varepsilon F_0 \sigma_\eta(\varepsilon) d\varepsilon \tag{$A.5.3$}$$

where e is the electron (elementary) charge, m_e is the electron mass, ε is the colliding electron energy, F_0 is the Electron Energy Distribution Function (EEDF) and $\sigma_\eta(\varepsilon)$ is the η-th collisional process cross section.

Introducing the collision cross sections in the forward rate constant expression in equation (5.15) yields:

$$\tilde{k}_j^f = \sum_{\eta \in R:\eta \sim j} \left(\sqrt{\frac{2e}{m_e}} \int \varepsilon F_0 \sigma_\eta(\varepsilon) d\varepsilon \prod_{\hat{L}_\gamma \in \Lambda} \prod_{q \in \hat{L}_\gamma} D_{q,L_\gamma}^{\nu_{q,\eta}^f} \right) \tag{$A.5.4$}$$

Rearranging terms in equation ($A.5.4$) provides equation (5.19):

$$\tilde{k}_j^f = \sqrt{\frac{2e}{m_e}} \int \varepsilon F_0 \left[\sum_{\eta \in R:\eta \sim j} \sigma_\eta(\varepsilon) \prod_{\hat{L}_\gamma \in \Lambda} \prod_{q \in \hat{L}_\gamma} D_{q,L_\gamma}^{\nu_{q,\eta}^f} \right] d\varepsilon \tag{5.19}$$

From equation (5.19), it is possible to define a lumped collision cross section $(\widetilde{\sigma_j}')$ for the j-th reaction in the lumped chemistry set. In fact, to share the same formulation as in equation $(A.5.3)$, it can be rewritten as:

$$\tilde{k}_j^f = \sqrt{\frac{2e}{m_e}} \int \varepsilon F_0 \widetilde{\sigma_j}' d\varepsilon \qquad (A.5.5)$$

Comparing equations (5.19) and $(A.5.5)$ the expression for $\widetilde{\sigma_j}'$ is obtained:

$$\widetilde{\sigma_j}'\left(\varepsilon, \frac{E}{N}, T_g, p\right) = \sum_{\eta \in R:\eta \sim j} \sigma_\eta(\varepsilon) \prod_{\hat{L}_\gamma \in \Lambda} \prod_{q \in \hat{L}_\gamma} D_{q,L_\gamma}^{\nu_{q,\eta}^f}$$

where $\frac{E}{N}$, T_g, and p are, respectively, the reduced electric field, the gas temperature, and the gas pressure. The dependency of $\widetilde{\sigma_j}'$ on these three variables derives from D_{q,L_γ} (see Section 5.5.1.2). This aspect is undesirable for a proper cross section definition, and it can be removed by averaging $\widetilde{\sigma_j}'$ in the reduced electric field, gas temperature and pressure domains ($\Omega_{\frac{E}{N}}$, Ω_{T_g}, and Ω_p), yielding equation (5.20):

$$\widetilde{\sigma_j}(\varepsilon) = \frac{1}{\Delta_{\frac{E}{N}} \Delta_p \Delta_{T_g}} \int_{\Omega_{T_g}} \int_{\Omega_p} \int_{\Omega_{\frac{E}{N}}} \widetilde{\sigma_j}'\left(\varepsilon, \frac{E}{N}, T_g, p\right) d\frac{E}{N}\, dp\, dT_g \qquad (5.20)$$

where $\Delta_{\frac{E}{N}}$, Δ_{T_g}, and Δ_p are the reduced electric field, the gas temperature and gas pressure domains extensions.

5.10 References

[1] Sakai O, Nobuto K, Miyagi S and Tachibana K 2015 Analysis of weblike network structures of directed graphs for chemical reactions in methane plasmas *AIP Advances* **5** 107140

[2] Sun S R, Wang H X and Bogaerts A 2020 Chemistry reduction of complex CO_2 chemical kinetics: application to a gliding arc plasma *Plasma Sources Sci. Technol.* **29** 025012

[3] Lu T and Law C K 2005 A directed relation graph method for mechanism reduction *Proceedings of the Combustion Institute* **30** 1333–41

[4] Obrusník A, Bílek P, Hoder T, Šimek M and Bonaventura Z 2018 Electric field determination in air plasmas from intensity ratio of nitrogen spectral bands: I. Sensitivity analysis and uncertainty quantification of dominant processes *Plasma Sources Sci. Technol.* **27** 085013

[5] Hanicinec M, Mohr S and Tennyson J 2020 Fast species ranking for iterative species-oriented skeletal reduction of chemistry sets *Plasma Sources Sci. Technol.* **29** 125024

[6] Pepiot-Desjardins P and Pitsch H 2008 An efficient error-propagation-based reduction method for large chemical kinetic mechanisms *Combustion and Flame* **154** 67–81

[7] Berthelot A and Bogaerts A 2016 Modeling of plasma-based CO_2 conversion: lumping of the vibrational levels *Plasma Sources Sci. Technol.* **25** 045022

[8] Pepiot-Desjardins P and Pitsch H 2008 An automatic chemical lumping method for the reduction of large chemical kinetic mechanisms *Combustion Theory and Modelling* **12** 1089–108

[9] Rehman T, Kemaneci E, Graef W and Van Dijk J 2016 Simplifying plasma chemistry via ILDM *J. Phys.: Conf. Ser.* **682** 012035

[10] Lu and Law C K 2006 Systematic Approach To Obtain Analytic Solutions of Quasi Steady State Species in Reduced Mechanisms *J. Phys. Chem. A* **110** 13202–8

[11] Cazères Q, Pepiot P, Riber E and Cuenot B 2021 A fully automatic procedure for the analytical reduction of chemical kinetics mechanisms for Computational Fluid Dynamics applications *Fuel* **303** 121247

[12] Dijkstra E W 1959 A note on two problems in connexion with graphs *Numer. Math.* **1** 269–71

[13] Sakiyama Y, Graves D B, Chang H-W, Shimizu T and Morfill G E 2012 Plasma chemistry model of surface microdischarge in humid air and dynamics of reactive neutral species *J. Phys. D: Appl. Phys.* **45** 425201

[14] Stankov M, Becker M M, Hoder T and Loffhagen D 2022 Extended reaction kinetics model for non-thermal argon plasmas and its test against experimental data *Plasma Sources Sci. Technol.* **31** 125002

[15] Alves L L and Tejero-del-Caz A 2023 Charged-particle transport models for global models Plasma Sources Science and Technology **32** 054003

Chapter 6

Conclusions

This thesis aimed to contribute to the current possibilities of numerical modeling of non-equilibrium plasma chemistry through the introduction and presentation of a new generalized simulation software for plasma chemistry. In particular, the SPPARK global model solver was described. Being built on a coupling of Bolsig+ and Cantera, SPPARK is capable of accurately representing both electron kinetics and reaction thermodynamics. The solver's modeling capabilities have been highlighted also in the context of non-strictly homogeneous systems through the adoption of a multi-zone modeling approach. Finally, an algorithm for chemical complexity reduction was developed, based on Analytically Reduced Chemistry techniques, enabling the simplification of detailed global-model reaction schemes into forms that can be adopted within spatially resolved models at a sustainable computational cost, while controlling the error introduced by the reduction in the quantities of interest.

It is believed that the methodological contribution introduced in this thesis provides a novel pathway towards more accurate and flexible models, which may assist in the understanding and optimization of plasma-chemical phenomena across a variety of applications, particularly for novel or poorly characterized chemistries.

The work presented here does not claim to be definitive, and several limitations remain. Regarding SPPARK as a base solver, it still lacks a proper treatment of the thermodynamics of excited species (and their associated temperatures), radiative transitions, and the coupling with electrical circuit models of complex sources, which are essential to accurately represent energy partitioning and power balances in many plasma devices. The application of SPPARK to multi-zone modeling is fundamentally limited by the need to approximate transport rates, starting from thermodynamic and kinetic parameters of the different regions, with explicit expressions. Finally, the reduction algorithm requires the inclusion of additional techniques to separate the different timescales in the system, such as partial equilibrium and quasi-steady-state approximations, and therefore the adaptation of existing methods in a more general and automated framework.

For these reasons, future work should focus on addressing these limitations, making the framework more robust and accurate, and on extending its modeling capabilities through direct coupling with multidimensional solvers.

Overall, the results of this thesis contribute to broaden the use of plasma-chemistry modeling tools and to facilitate the application of more predictive and versatile tools in both scientific and engineering contexts.

Acknowledgments

The PhD scholarships of the author Marchetti, A. was funded by Nuovo Pignone Tecnologie Srl. and by the European Union - NextGenerationEU through the Italian Ministry of University and Research under PNRR – Mission 4 Component 2, Investment 3.3 “Partnerships extended to universities, research centres, companies and funding of basic research projects” D.M. 352/2021 – CUP J33C22001480009.

This chapter of my life is also coming to an end. Personally, I think it’s important, in moments like this, to pause for a second and bring to mind all the good we’ve received while writing a new chapter in the book of our existence.

I now turn to you, the people mentioned in these last few lines. These words are mine. My thoughts, dedicated to you. To you as people, mentors, and loved ones.

I’d like to start by thanking Matteo. You always trusted me, gave me the space to express myself, tried to understand me, and guided and taught me a lot. We had the chance to get to know each other, to exchange ideas, and to discuss topics even beyond work. For all this, I am honestly and deeply grateful to you.

Romolo. We’ve often disagreed. You know I sometimes lack self-control. Yet despite everything, we’ve always understood each other. You’ve been a friend. You already know you helped me through difficult moments. Thank you.

Now to the guys from the lab. They often say that a journey is something personal. But experience teaches us that, as we walk our path, putting one foot in front of the other, we meet others who walk it with us. In those cases, singing while struggling eases the fatigue. Thank you for being there.

Michi. You’re a precious friend. You’ve been close to me, listened to me, and let me return the favour so many times I’ve lost count. You have only one flaw: you no longer drink the Pastis beers the way you used to. Still, I have an evil plan to get you back in shape. I wish you all the best, always.

Pasquale. I don’t need to tell you anything. Yet we’ve become close lately. Let’s keep pitying each other, because you know — “megghjiu criscia purci”...

Kosta. As I write these words of thanks to you, I suddenly get hungry and feel like going to the gas station. I thank you truly, from my heart. You've been like a brother to me. Your hospitality has always deeply moved me. I hope to hug you again soon.

Ginuzzo. Thank you for your eyes. I don't know what I've done to deserve your affection. I think all I can do is enjoy it. I'm still thinking about getting you some climbing shoes — though I'm not sure Anna would approve…

Vittoria and Saverio. You've treated me like a son. I'll always try to be worthy of it.

Zia Ponch. Every time I see you, you remind me to enjoy life. You're a force of nature. Thinking of you always sets me back on the right path, even when things are tough.

Cipo, Mamma, and Babbo. You are my family. Much of who I am, I owe to you. We laugh, we get angry, and we suffer together. I love you.

Chiara. Thank you for being you.